STUDYING THE ELECTRON POPULATION EFFECTS ON MAGNETRON OSCILLATION VIA PARTICLE-IN-CELL SIMULATION

by

Andong Yue

A dissertation
submitted in partial fulfillment
of the requirements for the degree of
Doctor of Philosophy in Electrical & Computer Engineering
Boise State University

May 2021

BOISE STATE UNIVERSITY GRADUATE COLLEGE

DEFENSE COMMITTEE AND FINAL READING APPROVALS

of the dissertation submitted by

Andong Yue

Dissertation Title:	Studying the Electron Population Effects on Magnetron Oscillation Via Particle-In-Cell Simulation
Date of Final Oral Examination:	10 March 2021

The following individuals read and discussed the dissertation submitted by student Andong Yue, and they evaluated the student's presentation and response to questions during the final oral examination. They found that the student passed the final oral examination.

Jim Browning, Ph.D.	Chair, Supervisory Committee
Kris Campbell, Ph.D.	Member, Supervisory Committee
Hani Mehrpouyan, Ph.D.	Member, Supervisory Committee
Harish Subbaraman, Ph.D.	Member, Supervisory Committee
Peng Zhang, Ph.D.	External Examiner

The final reading approval of the dissertation was granted by Jim Browning, Ph.D., Chair of the Supervisory Committee. The dissertation was approved by the Graduate College.

DEDICATION

I dedicate this dissertation to my parents, Yunqing Yue and Lingyun Zheng, for their relentless support for my education. They also guided me in making many correct decisions at many critical junctions of my life. My accomplishments today would not have been possible without their support.

ACKNOWLEDGMENTS

I would like to thank Dr. Browning for giving me the opportunity to work on this research and for his precise and consistent support throughout my career as a Ph.D. student. I would like to also thank Dr. Kris Campbell, Dr. Hani Mehrpouyan, Dr. Harish Subbaraman for serving on my dissertation committee, and Dr. Peng Zhang for serving as the external examiner.

I would like to acknowledge Dr. Marcus Pearlman and Dr. Sulmer A. Fernandez-Gutierrez, who worked on this project before me and laid many of the important ground works for this research.

Material support for this work is provided by the Air Force Office of Scientific Research under award # FA9550-19-1-0101. Geometry drawings and the magnetron hardware were generously provided by L3Harris Technologies. Technical support of the VSim code was provided by Tech-X Corporation.

ABSTRACT

This research examines magnetron physics via the Particle-In-Cell simulations of two magnetron models, the 2D Rising Sun magnetron model and the 3D L3Harris CWM-75kW magnetron model, by using new data analytic schemes. Two data analytic schemes are presented, the electron population analysis and the breadth ratio analysis; these schemes reveal insights into the magnetron physics that are not readily accessible otherwise. Both magnetron models were simulated a) without priming, b) with RF priming, and c) with modulated electron injection. The research found that the 2D Rising Sun magnetron model is sensitive to RF priming; a 50 ns RF priming at less than 1% of the magnetron operating power resulted in a dramatically faster oscillation startup (100 ns with RF priming vs. 350 ns. without). Modulated electron injection led to a fast oscillation startup (80 ns); however, analyses show the oscillation frequency was not stable with the current simulation setup. At the current stage, the model for the L3Harris CWM-75kW does not start oscillation without priming. Oscillations were reached with both RF priming and modulated electron injection in about 160 ns. Analyses based on the results from both simulation models suggest that the electron population became more cycloidal leading to oscillation startup. Although this increased cycloidal motion of the electron population before oscillation did not directly lead to net motion of the electron population toward the anode, a clear correlation was found between the increased electron cycloidal motion and expansion of the electron hub towards the anode. Net electron motion towards the anode does not occur until the electron hub reaches the anode and the device begins to oscillate. A strong correlation was also found between the stability of the oscillation and stability of the net electron motion in the radial direction.

TABLE OF CONTENTS

LIST OF TABLES

LIST OF FIGURES

LIST OF ABBREVIATIONS

RF	Radio Frequency
MVED	Microwave Vacuum Electron Device
CW	Continuous Wave
DC	Direct Current
GFEAs	Gated Field Emission Arrays
PIC	Particle-In-Cell
2D	Two-Dimensional
3D	Three-Dimensional
MFRPM	Multifrequency Recirculating Planar Magnetron
SWSs	Slow-Wave Structures
LBO	L-Band Oscillator
SBO	S-Band Oscillator
MDO	Magnetron with Diffraction Output
MIT	Massachusetts Institute of Technology
LTCC	Low Temperature Co-Fired Ceramic
FDTD	Finite Difference Time Domain
PDEs	Partial Differential Equations
CFL	Courant-Freidrichs-Lewy
PEC	Perfect Electric Conductor
MAL	Matched Absorbing Layer

RAM	Random Access Memory
HDF5	Hierarchical Data Format 5
FFTs	Fast Fourier Transforms
CAD	Computer Aided Design

CHAPTER ONE: INTRODUCTION

1.1 Radio Frequency (RF) and Microwave Vacuum Electron Devices (MVEDs)

Radio frequency (RF) technologies have become the backbone of many aspects of modern society due to RF radiation's unique capability of transmitting without a medium, while carrying a vast amount of information. RF technologies are used in nearly all wireless communication applications ranging from cell phones to satellite communication. Aside from its prominent use in communication, RF technologies are used for object detection (radar) and heating (microwave ovens) [1].

The development of every RF application necessarily encounters the two most fundamental properties of RF radiation: frequency and power. In a sense, the countless RF applications that are foundational to modern society are merely different combinations of frequency and power. In simple terms, a higher frequency enables the RF radiation to carry more information, while a higher power enables the radiation to propagate farther through media. With the ever-expanding need for more information and faster data transfer, communication engineers must use higher frequencies. However, the design of higher frequency systems comes with many significant challenges.

High frequency signals are difficult to generate efficiently since RF generation, on the most fundamental level, requires conversions of the kinetic energy of an electron stream to coherent electromagnetic radiations [2]. In general, RF radiation can be generated by using solid-state devices or microwave vacuum electron devices (MVEDs). In solid-state devices, electrons collide with the material lattice, resulting in the electron kinetic energy being converted to wasted heat. When the frequency is low, such collision is usually limited; however, at higher frequencies, such collisions often lead to massive efficiency loss or to the complete breakdown of the device. This collision issue also significantly limits the power capability of solid-state devices for RF generation at higher frequencies.

On the other hand, in MVEDs, an electron stream flows through a vacuum collisionlessly, which bypasses the material limitations on the path of the electron steam. In general, vacuum electron devices can generate powerful RF radiation at high frequencies at levels beyond the capability of solid-state devices [3]. Figure 0-1 shows the power versus frequency performance of various MVEDs compared to the solid-state

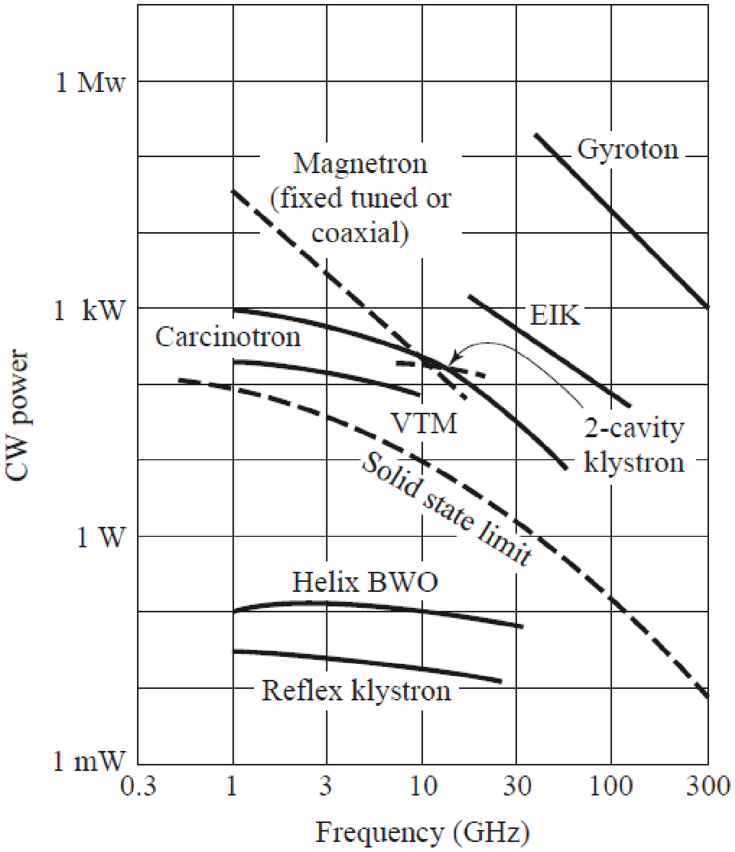

Figure I-1 Continuous wave (CW) power v. frequency performance of various MVEDs compared to the solid-state limit [3]

limit. As the frequency increases, the continuous wave (CW) power that can be efficiently generated by solid state devices exponentially decays. Solid state devices are difficult to use for applications that require CW power generation beyond the kilowatt threshold unless combined together.

1.2 The Magnetron

This dissertation is concerned with one type of MVED, known as the magnetron. A MVED is a broad category that includes families of oscillators and amplifiers, some of which are cross-field devices [4]. In a cross-field device, the DC electric field is perpendicular to the static magnetic field. A cross-field causes electrons to have cycloidal motions and, thus, permits electrons to interact with an RF field [5]. The magnetron is such a cross-field device. The magnetron is an efficient oscillator capable of high-frequency, high-power RF generation. Magnetrons can operate pulsed or continuous wave. At the current stage, pulsed magnetrons are widely used for radar applications, while continuous wave magnetrons are used for heating and material processing [2], [6].

The magnetron geometry can have a linear format or a cylindrical format. There are minor differences between the two forms, but the overall operating principles of the device are the same across both forms. Typically, when operating a magnetron, the anode is at ground potential, and the cathode is at some negative potential, resulting in a DC electric field between the anode and the cathode. The vacuum space between the cathode and the anode is typically referred to as the interaction space (a.k.a. the A-K gap). At the same time, a magnetic field is applied perpendicular to the DC electric field via a permanent magnet or an electromagnet. Typically, the magnetron cathode is a thermionic cathode that is capable of injecting electrons into the interaction space via thermionic emission [7]. However, some high-power magnetrons use field emission cathodes. Once electrons are in the interaction space, they interact with the resonant circuit (anode) and begin bunching, which results in oscillation and, ultimately, high-power, high-frequency RF generation. Chapter Two contains a detailed discussion of the underlying physics behind magnetron operation.

1.3 A Brief History of Magnetron Research

The magnetron was first invented by H. Gerdien in 1910 [8] and was radically improved by John Randall and Harry Boot at the University of Birmingham during the second World War [9]. The magnetron served an important role in the war for its ability to vastly improve radar performance both in terms of power and efficiency. The magnetron was first used in cooking when Raytheon engineer Percy Lebaron Spencer found a piece of chocolate melting in his pocket when he was experimenting with a piece of magnetron-driven radar equipment [10]. Spencer patented the microwave oven on October 8th of 1945, and the first commercially available microwave oven, which was 6 ft. tall, weighed 750 lb. and cost more than 2,000 USD, hit the market in 1947 [11]. Decades later, with the advent of silicon semiconductor devices for RF signal generation, the magnetron, along with many other similar vacuum electron devices, faded out of mainstream attention. Throughout the latter half of the 20th century, magnetron research and development continued for use in various kinds of radar, electronic warfare, and industrial heating systems. Theoretical understanding and simulation of magnetrons has continued to evolve and to elucidate the intricate physical principles behind its operation, something that is still not sufficiently understood. With the increasing power demand of various contemporary RF applications, semiconductor devices are still not adequate for some applications that require high power and high frequency. Magnetrons been developed in various industries, and the magnetron receives attention for its exceptional efficiency (up to 90%) and high power density (up to the order of $kW*cm^{-2}$ when pulsed). However, magnetrons are free running oscillators, which are difficult to phase lock, thus limiting their applications. Chapter Three provides a survey of recent cutting-edge magnetron research.

1.4 Background for the Current Research

Traditionally, magnetrons use thermionic cathodes, which emit electrons by heating a wire or a conductor surface to a temperature that allows the electrons to be “boiled off.” Other magnetrons use field emission cathodes. In either case, electron emission and the oscillation process are random, and phase control is not possible without external components. The phase of the output RF signal drifts over time during oscillation [12]. This variation in the phase of the output RF signal significantly limits the magnetron’s potential for many applications, namely the applications that utilize phase modulation. This phase variation also prohibits the use of the magnetron in array arrangements since signal coherency cannot be ensured. Hence, research that explores methods to phase control the magnetron is of great value, especially considering that the magnetron is among the most efficient high power RF sources, and this phase randomness issue is the key roadblock keeping the magnetron from being used for many important applications.

One potential solution to the phase variation issue is to develop and use a different cathode that is capable of controlled electron emission. If the electron injection process can be controlled spatially and temporally, then the magnetron oscillation might be phase controlled. Gated field emission arrays (GFEAs) are ideal for such a cathode as they are two-terminal devices, which have emission that can be controlled by modulating the voltages applied to the gates [13]. Chapter Four will provide a summary of the experimental plan to use a GFEA-based cathode in the magnetron. Though the physical experiment is not the focus of this dissertation, a summary of it provides the necessary background information.

1.5 The Current Research

The primary focus of the current research is to study the magnetron via particle-in-cell (PIC) simulations [14]. The goal is to study various fundamental physical principles associated with the magnetron's startup process that are not sufficiently understood.

The research presented in this dissertation focuses on two specific magnetron designs: The Rising Sun magnetron and the L3Harris CWM-75 kW industrial magnetron. The development of the 3D CWM-75kW magnetron model is one of the major efforts of the current research. New methods for analyzing the electron population over time were developed for this research and are significant parts of this research effort. These analysis methods were applied to both the 2D Rising Sun model and the 3D CWM-75kW model to extract useful insights into the fundamental physics behind magnetron oscillation.

1.5.1 Rising Sun Magnetron

The 2D Rising Sun magnetron model was studied extensively at Boise State [15-17], and previous research focused on the implementation of the PIC simulation model and the study of phase control by modulated electron injection. The details of the previous work can be found in section 3.3 in this document. The work on the 2D Rising

Sun magnetron model presented in this dissertation builds on those previous efforts, with the functional PIC simulation model built and refined by previous researchers. This new research focuses on leveraging the model to study the particle physics during magnetron start up by applying newly developed analysis techniques. The 2D Rising Sun magnetron simulation model is not based on an actual device. However, the simulated device model oscillates in the π-mode and is a 2D model, so it is ideal for studying magnetron oscillations without the enormous computation overhead of a 3D model.

1.5.2 L3Harris CWM-75kW

The L3Harris CWM-75kW, Figure 0-2, is a CW industrial strapped magnetron capable of 75kW of sustained power output. The typical operating parameters are listed in Table 0-1. Collaborators at L3Harris have experimentally shown that the magnetron is also capable of operating at a set of low-power parameters (also listed in Table 0-1). A

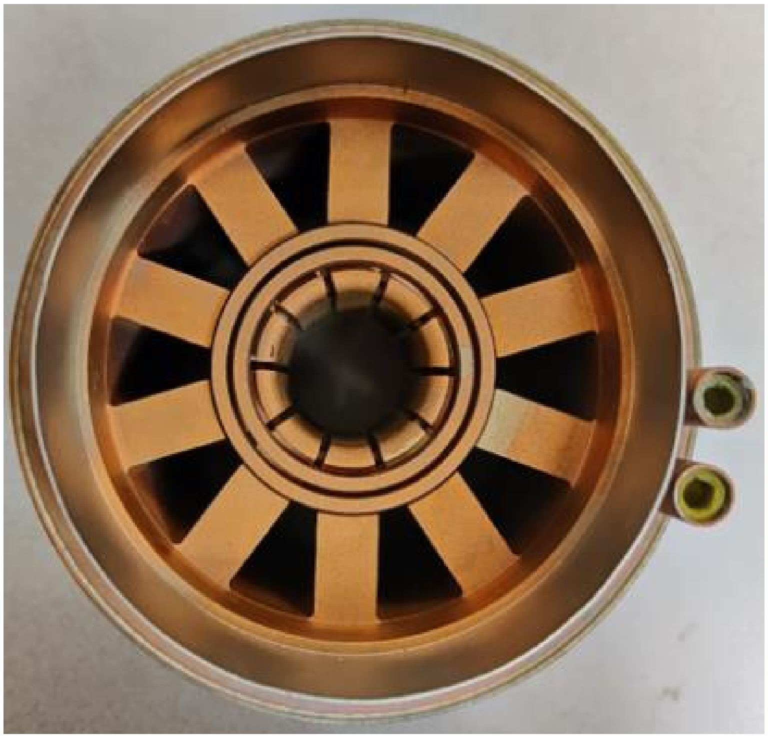

Figure I-2 Top view of the L3Harris CWM-75kW magnetron (cathode not included).

Table I-1 Operating Parameters for the CWM-75kW [16]

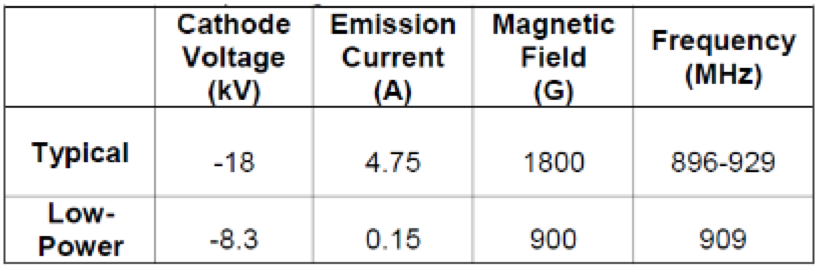

	Cathode Voltage (kV)	Emission Current (A)	Magnetic Field (G)	Frequency (MHz)
Typical	-18	4.75	1800	896-929
Low-Power	-8.3	0.15	900	909

detailed specification sheet of the device can be found in Appendix A [15]. Unlike the 2D Rising Sun magnetron, the CWM-75kW is a commercially available product; the simulation requires a full 3D model in order to properly simulate the strapped-magnetron π-mode. Hence, this model requires significantly more development to make it functional. This model cannot be simulated in 2D due to its inclusion of straps (to be discussed in Chapter Two). Chapter Five will discuss the ways these simulation models are set up, and Chapters Six and Seven will each focus on the simulation results generated by each model.

1.5.3 Electron Population Analysis

Chapter Eight will provide an introduction to the new data analysis techniques, and Chapters Nine and Ten will discuss the findings of the new analysis technique when applied to each model. Finally, a discussion of the fundamental physical implications will be provided.

1.5.4 A Note on the Order of Research

For the sake of clarity for the reader, it is worth noting the order by which the research progressed. The development of the 3D model for the CWM-75kW was completed first. After successful simulation of the device, the electron population analysis was then developed to gain additional insights into the magnetron start up physics. However, the 3D model takes too long to run, with a typical simulation taking up to a week. The amount of data generated by the 3D model (on the order of a terabyte per simulation) also takes a lot of computational time to analyze. For these reasons, the focus of the research was shifted back to the 2D Rising Sun model, as the 2D model is significantly faster to simulate (hours) and to analyze.

1.6 Significance

This research studied magnetron startup physics by simulating two different magnetron models with PIC. The research involves the simulation study of the models' startup behavior using different techniques to start oscillation. For each model, three startup cases were studied: startup with no priming, startup with RF priming, and startup with cathode modulation. The cathode modulation case is intended to study the effects of electron injection on phase control. Several novel analysis techniques were developed to capture the attributes of the electron population, which provides significant insights into the underlying physics. It is believed that these techniques offer new insights into the startup physics and operating conditions of magnetrons and that the techniques could be applied to other device simulations with large particle populations including cross-field amplifiers, klystrons, traveling wave tubes, Hall thrusters, etc.

CHAPTER TWO: THEORETICAL CONSIDERATIONS

2.1 Basic Physics of Magnetron Oscillation

The oscillation of the magnetron, as with oscillations in general, is a dynamic equilibrium and a delicate unification of chaos and order. On the one hand, oscillations require rapid movements of energy in alternating directions; on the other hand, such energy movements must be bounded and periodic for RF to be generated. This process requires energy to be periodically stored and released.

For many applications, oscillation can be achieved by using discrete electrical components such as capacitors and inductors; however, such discrete components become inadequate when high frequency and high power are needed simultaneously, in which case vacuum electron devices are used instead. In the case of the magnetron, the device consists of three major parts: (a) the resonating cavities, which geometrically integrate both inductance and capacitance in a compact circuit, (b) the cathode, which is responsible for injecting electrons into the interaction region, and (c) the interaction region, which is the vacuum space between the anode and the cathode that facilitates particle motions, field dynamics, and the interaction between the two.

2.1.1 Magnetron as a Circuit

A magnetron's resonator cavities can have various shapes, as shown in Figure 0-1, but all these of shapes are composed of two fundamental aspects: a gap, which provides the resonating cavities with capacitance, and a loop, which provides the resonating cavities with inductance. So, a magnetron resonating cavity is, essentially, a capacitor and an inductor in parallel, as shown in Figure 0-2.a [6]. Hence, the magnetron anode can be viewed as a circuit, shown in Figure 0-2.b, and its resonance characteristics are determined by the geometry of the resonating cavities.

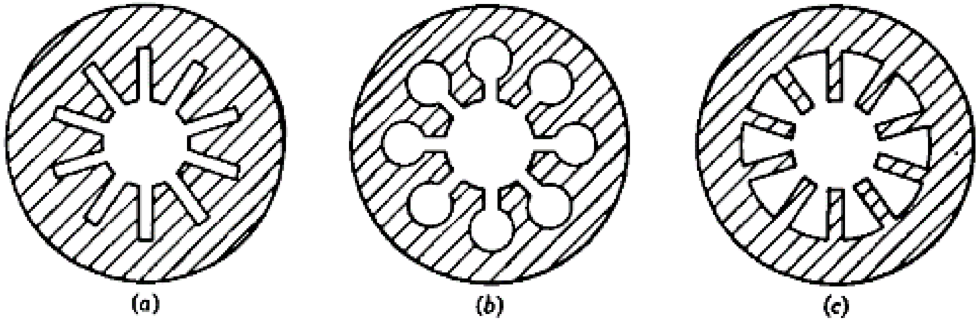

Figure II-1 Various types of magnetron resonator cavities [6]

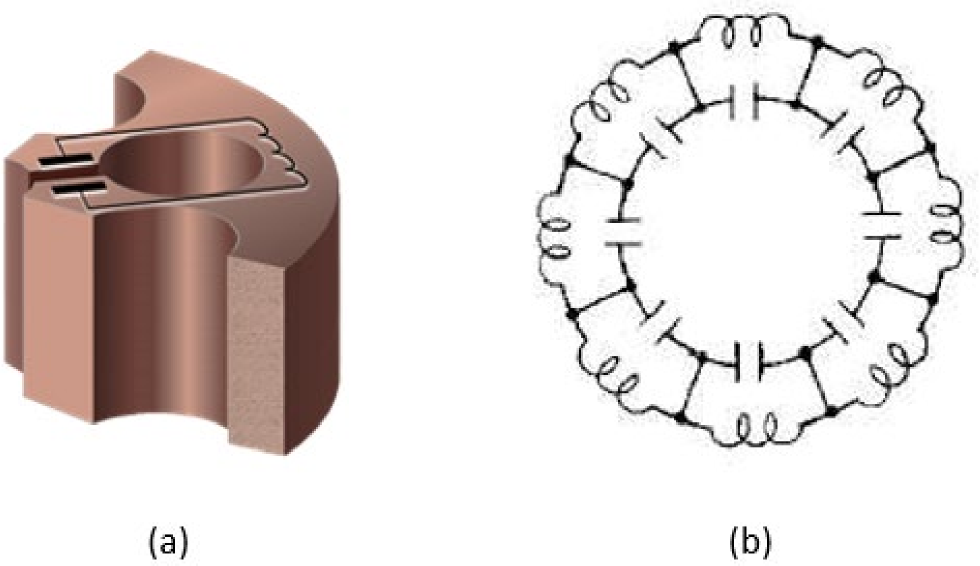

Figure II-2 a) A single magnetron resonator cavity as a circuit [17]; b) The entire magnetron anode as a circuit [18].

To examine the typical response of the magnetron anode circuit, consider the eight-cavity resonating circuit shown in Figure 0-2.b. By applying circuit theory, the resonant frequency of an individual resonator is:

$$\omega_0 = \frac{1}{\sqrt{LC}} \qquad \text{Eq. 0-1}$$

where ω_0 is the resonant frequency, and L, C are the inductance and capacitance of the individual resonator. Because the resonating cavities are evenly spaced, the phase differences φ are the same between adjacent cavities. Then the voltages in the cavities are:

$$V_1 = V_{RF} * \sin(\omega_0 t) \qquad \text{Eq. 0-2}$$

$$V_2 = V_{RF} * \sin(\omega_0 t + \varphi) \qquad \text{Eq. 0-3}$$

$$V_3 = V_{RF} * \sin(\omega_0 t + 2\varphi) \qquad \text{Eq. 0-4}$$

•••

$$V_8 = V_{RF} * \sin(\omega_0 t + 7\varphi) \qquad \text{Eq. 0-5}$$

$$V_9 = V_{RF} * \sin(\omega_0 t + 8\varphi) \qquad \text{Eq. 0-6}$$

where V_{RF} is the amplitude of the RF voltage.

Because the resonant system is circular, V_9 must be equal to V_1 and the total phase shift around the resonator system must be a multiple n of 2π, where n is often referred to as the mode number. In general, n = 1, 2, 3, …, N/2, where N is the total number of resonator cavities. For an eight-cavity magnetron, shown in Figure 0-2.b, the phase differences corresponding to n = 1, 2, 3, 4 are π/4, π/2, 3π/4, and π. The electric field distributions of these modes can be seen in Figure 0-3. In principle, there exists an infinite number of higher modes (n > N/2) in a resonant system; however, these higher modes are widely considered unimportant, since they correspond to the upper harmonics of the resonant system and have very low power capability. Among the fundamental modes (n ≤ N/2), the π mode has the highest power efficiency [6]. In this case, the phase shift between adjacent resonators is 180 degrees. For this reason, in many industrial magnetrons, including the CWM-75kW, there are structures called “straps”, Figure 0-4, that physically connect every other resonator vane to force the magnetron to oscillate in the π mode.

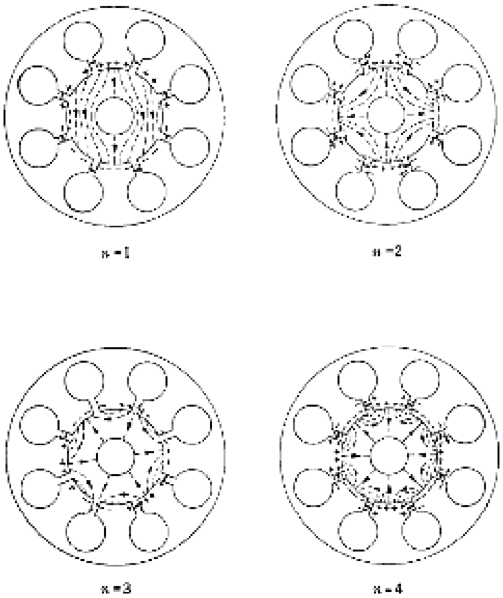

Figure II-3 Electric field distribution for the fundamental modes of an eight-cavity magnetron [6]

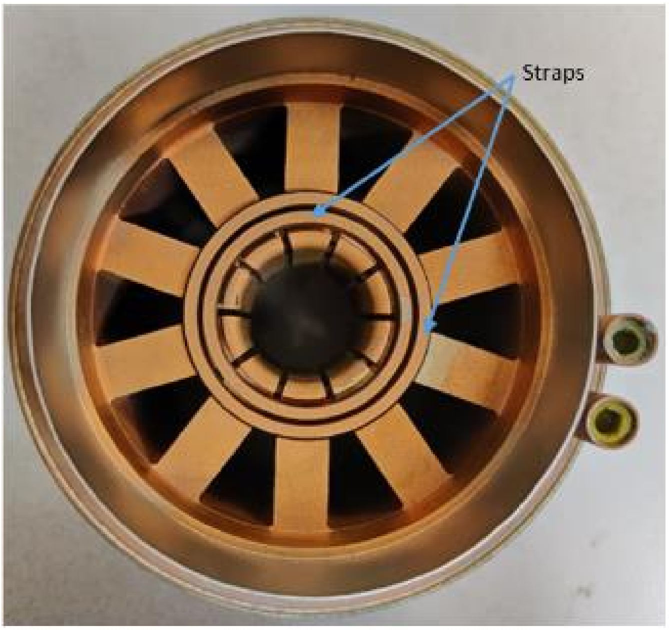

Figure II-4 Photograph of the top-down view of the anode RF circuit in the CWM-75kW. The straps that connect vanes are indicated, and the vanes force π-mode oscillation.

2.1.2 Magnetron Cathode

The cathode is responsible for electron emission; it is an integral component of MVEDs in general and research in this area is prolific [22-23]. In the magnetron, the cathode is usually a thermionic cathode (i.e. a “hot cathode”), but in recent decades, the uses of a field emission cathode (i.e. a “cold cathode”) in the magnetron are also being explored.

A thermionic cathode generates electrons via thermionic emission, a phenomenon first discovered in the late 19th century. Thermionic emission occurs when a metal is heated to high temperature and electrons on the metal surface gain enough energy to “boil off’ the metal surface. The physical theory behind thermionic emission was systematically studied and formalized by O. W. Richardson with his Nobel Prize winning work, now known as “Richardson’s Law” [19]. Richardson’s emission law has the following form:

$$J = A_G T^2 e^{\frac{-W}{kT}}, \qquad \text{Eq. 0-7}$$

where J is the emission current density, T is the temperature of the metal, W is the metal’s work function, k is the Boltzmann constant, and A_G has the form:

$$A_G = A_0 \lambda_R, \qquad \text{Eq. 0-8}$$

where A_0 is a constant given by:

$$A_0 = \frac{4\pi m k^2 q_e}{h^3} \approx 1.2 * 10^6 \; A m^{-2} k^{-2} \qquad \text{Eq. 0-9}$$

and m and q_e are the mass and charge of an electron, respectively. λ_R is a material correction factor that is specific to each piece of material. λ_R can be different between two pieces of material even if they are made of the same metal, and λ_R can change for the same piece of material due to degradation. The CWM-75kW magnetron uses a helical thermionic cathode.

A field emission cathode generates electrons via field emission. Field emission occurs when a conductive material (usually of high geometric aspect ratio) is exposed to an electrostatic field. When the electrostatic field strength exceeds a critical threshold, electrons are “pulled” out of the metal as the result of quantum tunneling. The theory behind field emission was most notably studied by R. Fowler and L. Nordheim [20]. Note that since field emission is controlled by the strength of the electrostatic field, field emitters can have a simple two terminal structure or a three terminal gated structure. Electron emission from gated field emitters can usually be controlled on a finer level by voltage modulation on the gate in comparison to ungated field emitters or thermionic emitters.

2.1.3 General Electron Motions in the Magnetron

Electron motion in the magnetron is a complex subject. In general, a particle with charge q and velocity **v** in electric field **E** and magnetic field **B** is subject to electromagnetic force, described by the Lorentz force law:

$$\boldsymbol{F} = q\boldsymbol{E} + q\boldsymbol{v} \times \boldsymbol{B} \qquad \text{Eq. 0-10}$$

As an electron is emitted by the cathode, it is being pulled towards the anode by the electric field; however, as the electron accelerates towards the direction of the anode, its trajectory is bent by the magnetic field due to the $\boldsymbol{v} \times \boldsymbol{B}$ term. Since the $\boldsymbol{v} \times \boldsymbol{B}$ term involves a cross product, assuming the magnetic field **B** is constant, then the Lorentz force would cause the electron to undergo constant acceleration in a direction that is perpendicular to both the direction of the electron velocity and the direction of the magnetic field. This leads to what is known as electron gyromotion, as illustrated in Figure 0-5 in a linear format.

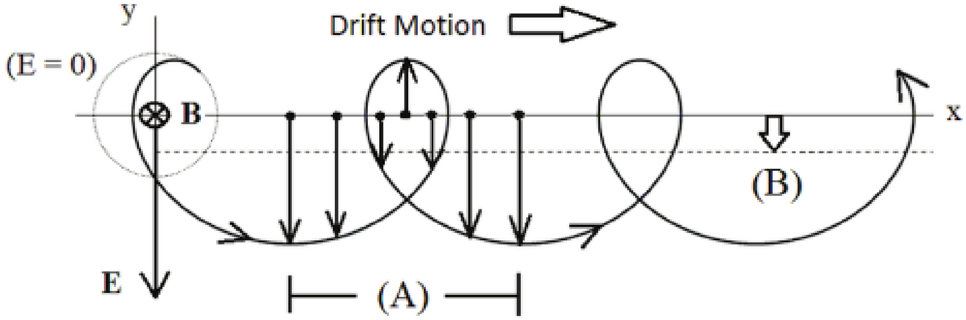

Figure II-5 Electron gyromotion in the presence of a perpendicular electric field and magnetic fields (dark curve). In the absence of an electric field, the electron orbits around the origin (light circle). (A) denotes the length of one cycle; (B) denotes a potential shift in the gyromotion's guiding center [21]

In a cylindrical format, as is the case for the cylindrical magnetron, the electron is also subject to centripetal force, described by the classic formula:

$$F_c = \frac{mv_\perp^2}{r} \qquad \text{Eq. 0-11}$$

where m is the electron mass, $v_\perp$ is the tangential speed, and r is the radius of curvature.

Note that the discussion so far is on a single electron moving in electric and magnetic fields that are both perfectly uniform. In the operation of the magnetron, there are many particles that interact with each other (collisions), and both the electric and magnetic fields are strongly perturbed by the resonant cavities and moving electrons. Overall, there is a large ensemble of various forces (many of which are dependent on one another) acting on the electrons simultaneously; therefore, it is extremely difficult to develop a unified theory that captures all the aspects of electron motions in the magnetron. Hence, complex devices like the magnetron are usually studied with computational simulation tools.

2.1.4 Hull Cutoff and Hartree Condition

Energy is transferred from the electrons to the RF field supported by the resonant circuit in the interaction region. The energy transfer process requires a delicate balance between the DC voltage and the applied magnetic field.

For electron-field interaction to happen, emitted electrons must not directly go to the anode; because the cathode is biased at a negative voltage, a direct conduction path between the anode and the cathode would cause electrons to strike into the anode with high velocity, and all the electron energy would be kinetic. No particle-field interaction would happen, and no RF wave would be generated; this phenomenon is known as magnetron breakdown. Hence, for a given applied magnetic field voltage, the DC electric field perpendicular to the applied magnetic field cannot be too large to allow a direct conduction path to the anode. This condition is known as the Hull cutoff [22].

In a cylindrical format, let r_a and r_c denote anode radius (m) and cathode radius (m) respectively; B_0 denotes the applied magnetic field (G); V_{dc} denotes the applied DC voltage (V); e and m denote the electron charge (C) and the electron mass (kg) respectively. For a given applied magnetic field, the Hull cutoff can be written as:

$$V_{dc,max} = \frac{eB_0^2}{8m}\left(\frac{r_a^2 - r_c^2}{r_a}\right)^2 \qquad \text{Eq. 0-12}$$

which indicates that the amplitude of the applied DC voltage has an upper limit for a given applied magnetic field, such that electrons will not directly strike the anode.

For electron interaction to occur with the RF circuit (anode), the electrons must reach an azimuthal velocity at some point in their cycloidal orbit at least equal to the RF phase velocity of the circuit. If the applied voltage is too low, the electron will never reach the required velocity. The azimuthal velocity is maximum at the top of the cycloidal orbit; hence the condition for interaction at a minimum occurs at this location in the orbit. The cutoff voltage ($V_{hartree}$) of the magnetron in the presence of a rotating perturbation field is called the Hartree condition (also been referred to as the Buneman-Hartree condition or simply the B-H condition) named after British mathematician Douglas Hartree. The mathematical derivation of the Hartree voltage in a cylindrical magnetron involves a long and complex process (derived by Lovelace and Young [23]). It has been shown that, for a cylindrical magnetron, there are two cases:

a) assuming the axisymmetry is spoiled but the z translational symmetry is maintained, then

$$V_{hartree,(a)} = -1 + \left(1 + b_\varphi^2\right)^{\frac{1}{2}}\left(1 - \beta_\varphi^2\right)^{\frac{1}{2}} + \beta_\varphi b_z \qquad \text{Eq. 0-13}$$

b) assuming both the axisymmetry and the z translational symmetry are spoiled, then

$$V_{hartree,(b)} = -1 + \left(1 - b_\varphi^2 - b_z^2\right)^{\frac{1}{2}} + \beta_\varphi b_z + \beta_z b_\varphi \qquad \text{Eq. 0-14}$$

for both cases,

$$\beta_\varphi \equiv \frac{r_a \omega_{rf}}{c} \qquad \text{Eq. 0-15}$$

$$\beta_z \equiv \frac{u_z}{c} \qquad \text{Eq. 0-16}$$

$$b_\varphi \equiv \frac{2eI * \ln\left(\frac{r_a}{r_c}\right)}{mc^3} \qquad \text{Eq. 0-17}$$

$$b_z \equiv \frac{B_0}{B_*} \qquad \text{Eq. 0-18}$$

$$B_* \equiv \left|\frac{2mc^2 r_a}{e\left(r_a^2 - r_c^2\right)}\right| \qquad \text{Eq. 0-19}$$

where ω_{rf} is the RF frequency (rad/s), u_z is the electron velocity (m/s) in z, and I is the emitted current (A).

Overall, for a given applied magnetic field, the allowable DC voltage is bounded above by the Hull cutoff voltage and bounded below by the Hartree voltage. Note that the magnetron will work as long as the ratio between the applied DC voltage and the applied magnetic field is in this bound, but the magnetron has the highest efficiency only when the applied DC voltage is right at the Hartree voltage; this is due to the fact that at the Hartree voltage, the electron velocity at the top of its cycloid just matches the circuit phase velocity. Hence, the electron's overall trajectory is at the highest possible potential energy, i.e. closest to the cathode. This orbit then allows the electron to give up the maximum amount of potential energy to the RF wave. In actual operation, the applied DC voltage is usually slightly above the Hartree voltage to leave some room for potential errors and inaccuracies, since the magnetron would cut off if the applied DC voltage ever dipped below the Hartree voltage. With the equations for the Hull cutoff and the Hartree condition, the values of applied magnetic field and DC voltage can be varied to construct the plot known as the Hartree diagram, which shows the operating region for the magnetron.

2.1.5 Hartree Diagram for the 2D Rising Sun Magnetron

For the 2D rising sun magnetron, use $r_a = 0.0224\,m; r_c = 0.01\,m;\ \omega_{rf} = 2\pi * 960\,MHz$, sweeping the applied magnetic field value from 0 to 1.5 kG, then plotting the Hull cutoff voltage and the two cases of Hartree voltages yields Figure 0-6. Point 1 (0.9 kG, 22.2 kV) is the operating point where previous simulations were run [15-17]; point 2 is the reference operating point for the device. Both operating points sit above and close to the Hartree voltage lines. Interestingly enough, although the magnetron was designed in 2D, the reference operating point sits below the Hartree voltage assuming translational symmetry but sits right above the Hartree voltage without assuming translational symmetry. It seems that the assumption of translational symmetry, or the lack thereof, still has significant impact.

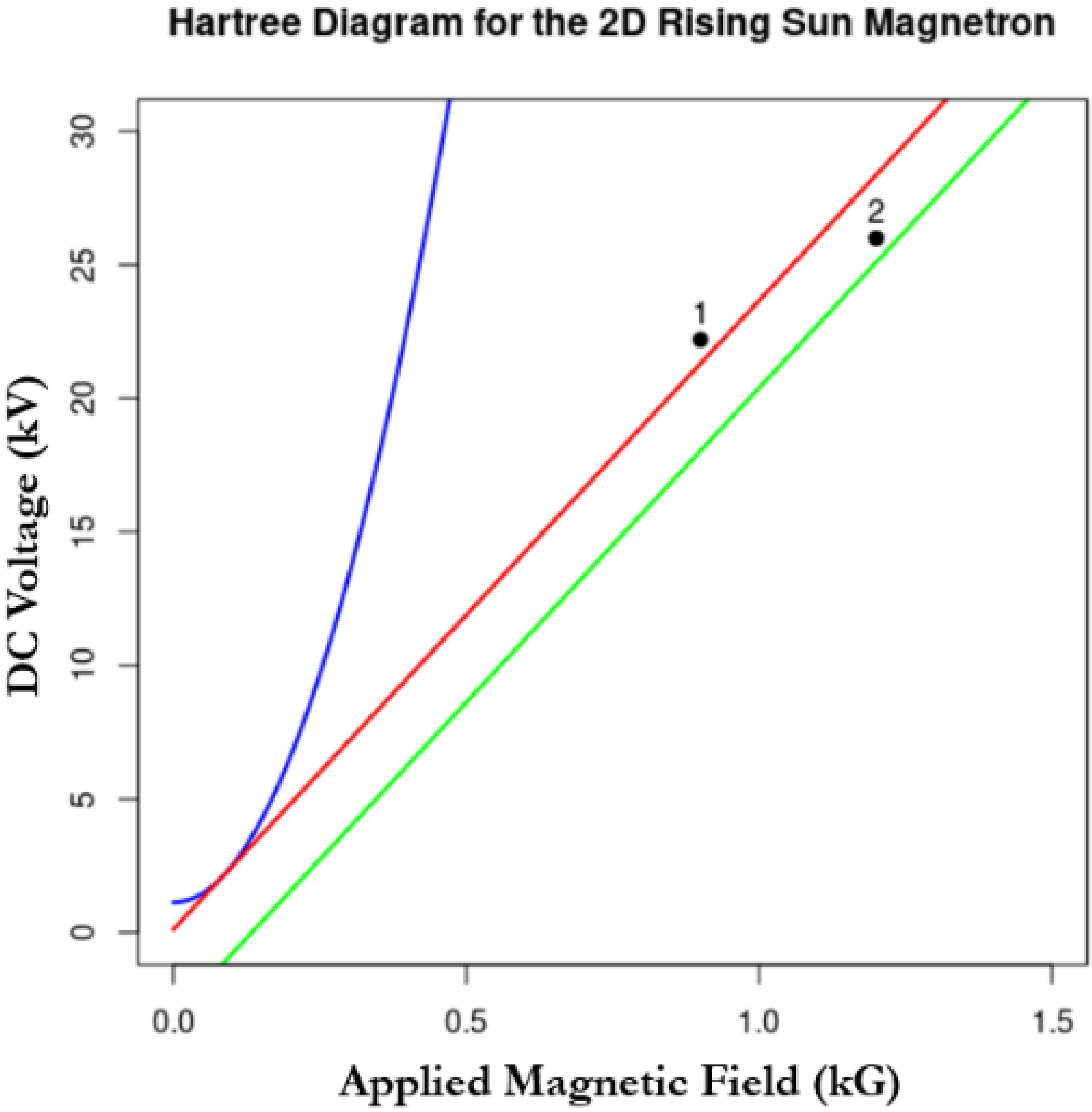

Figure II-6 Hartree diagram for the 2D rising sun magnetron. Blue: Hull cutoff voltage; red: Hartree voltage assuming translational symmetry; green: Hartree voltage without assuming translational symmetry. 1: operating point used in previous simulation (0.9 kG, 22.2 kV); 2: reference operating point (1.2 kG, 26kV).

2.1.6 Hartree Diagram for the CWM-75kW

By using the cathode, anode, and frequency parameters of the CWM-75kW ($r_a = 0.01428\,m; r_c = 0.00638\,m;\ \omega_{rf} = 2\pi * 908\,MHz$) and varying the values of the applied magnetic field from 0 to 2.2 kG, the Hull cutoff and Hartree voltage equations can be plotted as shown in Figure 0-7. The two confirmed operating points are slightly above the Hartree voltage, indicating the device operating points are consistent with maximum energy transfer (high efficiency).

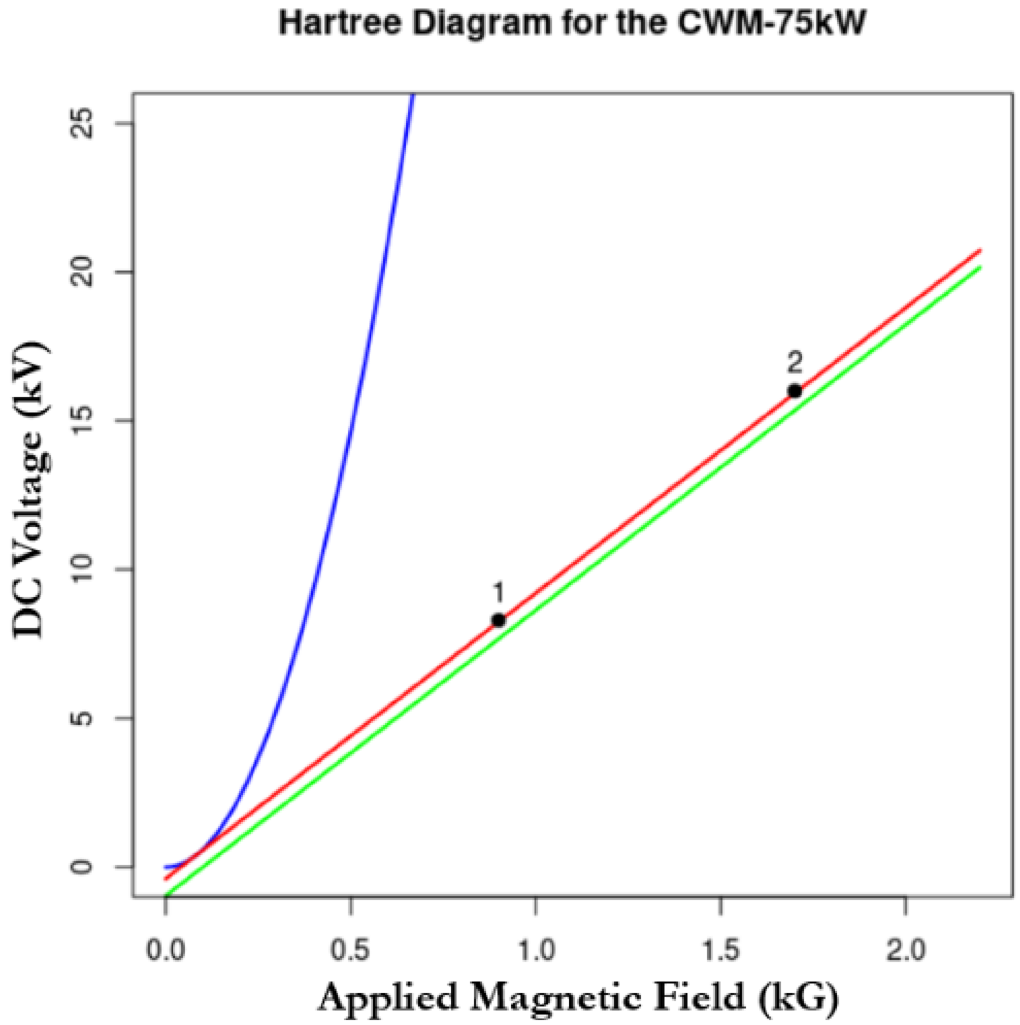

Figure II-7 Hartree diagram for the CWM-75kW. Blue: Hull cutoff voltage; red: Hartree voltage assuming translational symmetry; green: Hartree voltage without assuming translational symmetry. 1: Low-power operating point (0.9 kG, 8.3 kV); 2: Typical operating point (1.7 kG, 18 kV).

2.2 A Gap in the Theory

At this current stage, most theories about the magnetron describe the physics after the magnetron is already oscillating, such as the theories presented in section 2.1.1, or the conditions that are necessary to allow the magnetron to oscillate, such as the theories presented in section 2.1.3. However, the precise physical process from the beginning of start up to oscillation is still under study, and theories about this physics remain incomplete. Understanding the magnetron startup physics leading to oscillation is a major objective of this research. Magnetron physics is often looked at through the lens of plasma science, in which case the magnetron is a plasma device that involves only electrons and vacuum. Following this line of thought, the particle-fluid duality of plasma can be extended to the electron population in a magnetron.

2.2.1 Diocotron Instability

As the magnetron cathode emits electrons, due to the confinement of the magnetic field, an electron hub is formed around the cathode, which can be viewed as a sheet current of a finite width. The “diocotron instability”, sometime referred to as the “slipping stream instability,” is the plasma analog of the Kelvin-Helmholtz instability in general fluid mechanics. The instability is induced when unnaturalized charge sheets interact and generate a shear force at the interface [24]. This instability, along with the resonant nature of the magnetron anode cavities, is what may cause the magnetron to transition to oscillation. However, this hypnosis remains unproven and the critical physical details of such a transition are still unclear. After some early work on the theory in the 1960s [29-30], and some work from the late 1980s to early 1990s [31-32], little research has been pursued on this topic.

2.2.2 Brillouin Flow

The term “Brillouin flow” describes a type of electron flow named after the physicist Leon Brillouin, who first formalized the theory in his 1945 paper titled *A Theorem of Larmor and Its Importance for Electrons in Magnetic Fields* [25]. In the context of a cylindrical magnetron, Brillouin flow refers to a steady electron beam flowing around the cathode with near-constant radius. As discussed in section 2.1.2, after being emitted by the cathode, an electron enters gyromotion; as many electrons exhibit this behavior, they form what has been referred to as the “cycloidal flow” around the cathode. Theoretical research has shown that this cycloidal flow of electrons collapses to Brillouin flow during magnetron startup [34-36]. When the electron flow around the cathode is Brillouin flow, the electron cycloidal motion is minimized, and the electron flow behaves like a sheet current, and thus has very significant velocity shear within the flow, which gives rise to the proposed diocotron instability that potentially leads to magnetron oscillation, as discussed in section 2.2.1.

The challenges of theorizing magnetron startup physics arise from the extreme complexity of the problem and make it difficult to develop a unified analytical theory that is capable of both explaining and predicting magnetron start up physics from the transition of highly cycloidal electrons to Brillouin flow and to the diocotron instability. This issue is further complicated by the continuous introduction of new electrons and loss of older electrons to the system during the startup phase. One approach is to use PIC simulations, which have the appropriate particle physics and can demonstrate magnetron oscillations.

CHAPTER THREE: A SURVEY OF CURRENT STATE-OF-THE-ART IN MAGNETRON RESEARCH

Most current magnetron related research focuses on the design and modification of the magnetron for some specific applications; on the other hand, research that examines the fundamental physical principles behind the magnetron operation remains somewhat limited. Currently, academic fundamental magnetron research in the U.S. is being conducted by the University of Michigan [37-39], University of New Mexico [40-46], Boise State University [15-17], and some others [47-57]. The following sections will survey some of these works.

3.1 University of Michigan Harmonic Frequency Locking Research

The recent University of Michigan magnetron research studies a special type of magnetron named the Multifrequency Recirculating Planar Magnetron (MFRPM), shown in Figure 0-1, [26]. The MFRPM consists of two planar Slow-Wave Structures (SWSs) in a single cavity sharing the same cathode. The anode consists of a 1 GHz, six-cavity SWS (termed the L-Band Oscillator, LBO) and a 2 GHz, eight-cavity SWS (termed the S-Band Oscillator, SBO). Both SWSs have the same anode-cathode gap and were designed to operate in the π-mode (characterized by a 180 degrees phase advance per cavity). The MFRPM is designed to generate two frequencies (1 GHz and 2 GHz) simultaneously. The MFRPM structure is enclosed in a MELBA-C vacuum chamber, shown in Figure 0-2; each SWS has its own output antenna and its own load. The University of Michigan experiment first tested each SWS separately and obtained results shown in Table 0-1 and

Table 0-2. It is worth noting that the π -mode frequencies of the LBO and the SBO are not exactly 1 GHz and 2 GHz, respectively. For harmonic frequency locking to occur, the operating frequency of the SBO needs to be precisely twice the LBO's π -mode frequency, near 1,970MHz. However, this frequency does not match the π -mode frequency of the SBO; instead, it sits between the 6π/8-mode frequency (1.94 GHz) and the 7π/8-mode frequency (2 GHz). Next, the MFRPM was tested with both SWSs being present and the result is shown in Table 0-3.

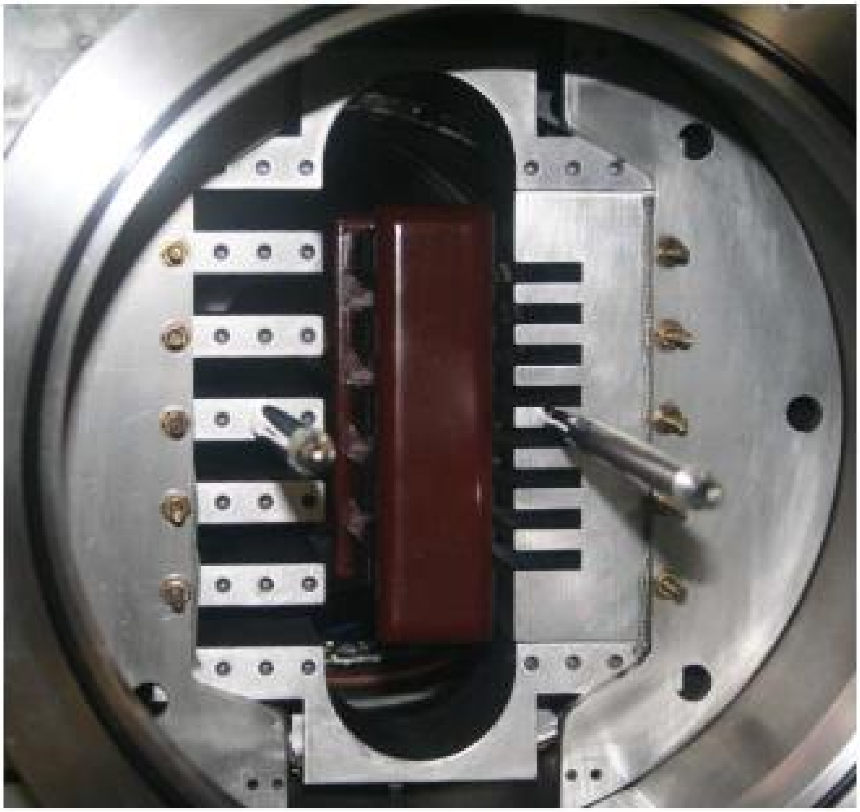

Figure III-1 MFRPM used in the University of Michigan Experiment [26]

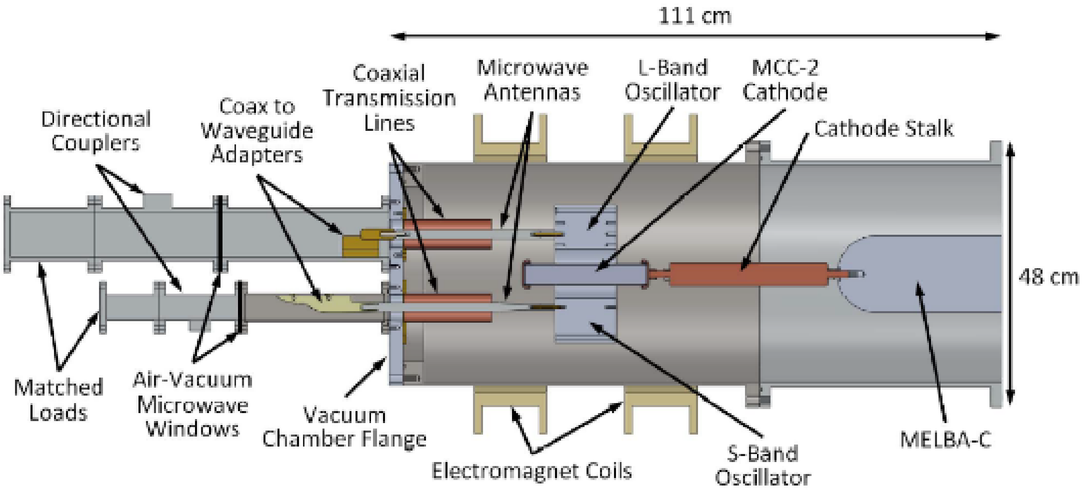

Figure III-2 Top sectional diagram of the MELBA-C vacuum chamber and MFPRM components. The anode support structure is not shown [26]

Table III-1 Summarized performance metrics for the isolated LBO near B = 0.16 T [26]

π-Mode Power [MW]:	25	±	2
π-Mode Frequency [MHz]:	986	±	3
Impedance [Ω]:	124	±	8
Efficiency [%]:	5	±	1

Table III-2 Summarized performance metrics for the isolated SBO near B = 0.16 T [26]

π-Mode Power [MW]:	18	±	2
π-Mode Frequency [MHz]:	2022	±	4
Impedance [Ω]:	236	±	21
Efficiency [%]:	7	±	2

Table III-3 Summarized Performance Metrics for the MFRPM in B = 0.16-0.18 T wherein consistent frequency locking occurred [26]

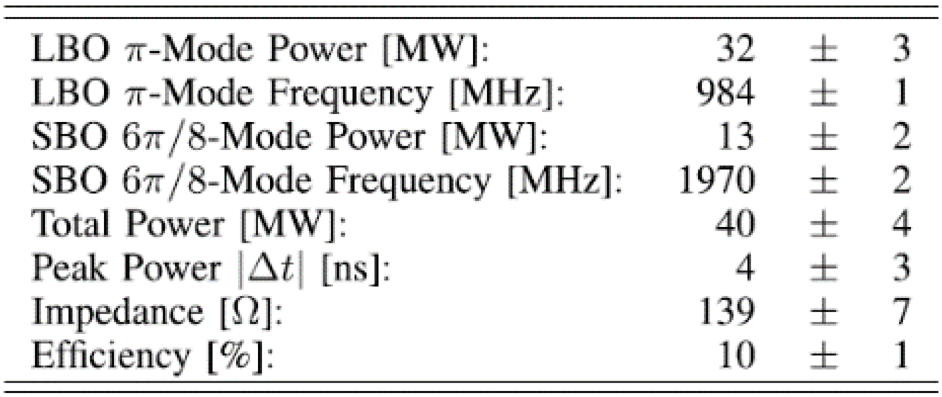

LBO π-Mode Power [MW]:	32	±	3
LBO π-Mode Frequency [MHz]:	984	±	1
SBO $6\pi/8$-Mode Power [MW]:	13	±	2
SBO $6\pi/8$-Mode Frequency [MHz]:	1970	±	2
Total Power [MW]:	40	±	4
Peak Power $\|\Delta t\|$ [ns]:	4	±	3
Impedance [Ω]:	139	±	7
Efficiency [%]:	10	±	1

With both SWSs being present in the MFRPM, there is a notable increase in the LBO's π -mode power compared to the π -mode power of the LBO in isolation, while the LBO's π -mode frequency stayed relatively the same. Hence, the LBO, in this case, maintained π -mode operation and enjoyed a significant boost in output power. On the other hand, the story is quite different when it comes to the SBO. With both SWSs being present in the MFRPM, the 6π/8-mode was excited in the SBO instead of the naturally preferred π -mode. Furthermore, the 6π/8-mode frequency was shifted from 1.94 GHz (in the isolated state) to 1.97 GHz, which precisely matches the second harmonic frequency of the LBO's π -mode. The SBO's 6π/8-mode power is significantly lower compared to its isolated π -mode power. These observed behaviors confirm that harmonic frequency locking has occurred.

3.2 The University of New Mexico "Transparent" Cathode Research

The University of New Mexico "transparent" cathode research considers the effects of using thin electron emission strips instead of a solid circular cathode in the magnetron. The researcher at The University of New Mexico found that "the electronic efficiency, which is the ratio of radiated power P to the power of electrons moving to the anode,

$$\eta_e = \frac{P}{UI_a} \approx 1 - \frac{\Delta}{d} \qquad \text{Eq. 0-1}$$

is determined by the ratio of the electron sheath thickness

$$\Delta = 2\frac{v_e \gamma_e^2}{\omega_{H0}} \qquad \text{Eq. 0-2}$$

to the [anode to cathode] gap. Here I_a is the anode current, $\omega_{H0} = eH_0/mc$ is the nonrelativistic cyclotron frequency, v_e is the average electron velocity along the cathode surface, and γ_e is the relativistic factor for the electron drift [27].” In addition, “$H_0 = \sqrt{H_{0z}^2 + H_{0\theta}^2}$, where H_{0z} is the applied axial magnetic field, $H_{0\theta} = 2I_z/cr$ is the azimuthal magnetic field of an axial current I_z, c is the speed of light, and r is the radius in the gap d between the cathode and the anode [27].”

Based on these equations, the fundamental idea for The University of New Mexico’s “transparent” cathode is to maximize the anode-cathode gap d, so that the electronic efficiency is maximized for any value of Δ. To achieve this goal, the solid cylindrical cathode was replaced with numerous “cathode strips,” as shown in Figure 0-3. The University of New Mexico’s simulations using the PIC code MAGIC have shown the “transparent cathode” leads to a quicker startup.

Recently, researchers at The University of New Mexico have experimentally implemented the “transparent” cathode in their “magnetron with diffraction output (MDO)” experiment [43-44]. While demonstrating the “transparent” cathode as a viable magnetron cathode, the University of New Mexico MDO experiment with “transparent” cathode has only achieved about 40% efficiency at the π-mode of the MDO, which falls short of the 70% efficiency obtained in simulation [43-44].

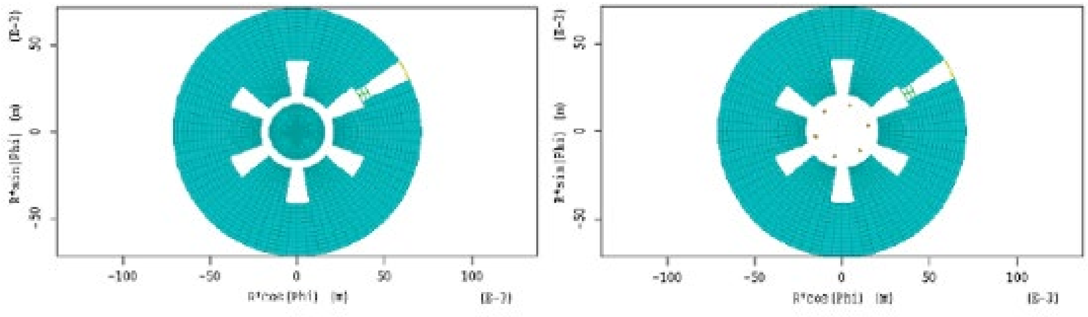

(a)   (b)

Figure III-3 The A6 magnetron with (a) the cylindrical cathode and (b) cathode strips [27]

3.3 Boise State University Rising-Sun Magnetron Simulation

The focus of the Boise State University magnetron simulation effort was to explore the feasibility of using modulated, addressable current sources in the magnetron for rapid startup and phase control [28]. Previous research has simulated such a current source in a 2D Rising Sun magnetron by using the simulation engine VORPAL, which later became VSim. The 2D magnetron simulation used the geometry shown in Figure 0-4. The applied DC voltage was 22.2 kV, the applied magnetic field was 0.09 T, and the emitted current density was 326 A/m. Simulations were performed with three different cathode configurations: cylindrical, five-sided, and ten-sided, shown in Figure 0-4. The research explored the device’s response under continuous, uniform current injection as well as under modulated current injection. For the modulated current injection case, the cathode was set up to emit at five discrete locations that rotate with the RF field at 957 MHz, which was the π mode for this geometrical design. Power output was simulated by defining an absorber in one of the long cavities to couple out the RF power generated by the device. A summary of the most important simulation results is shown in Table 0-4.

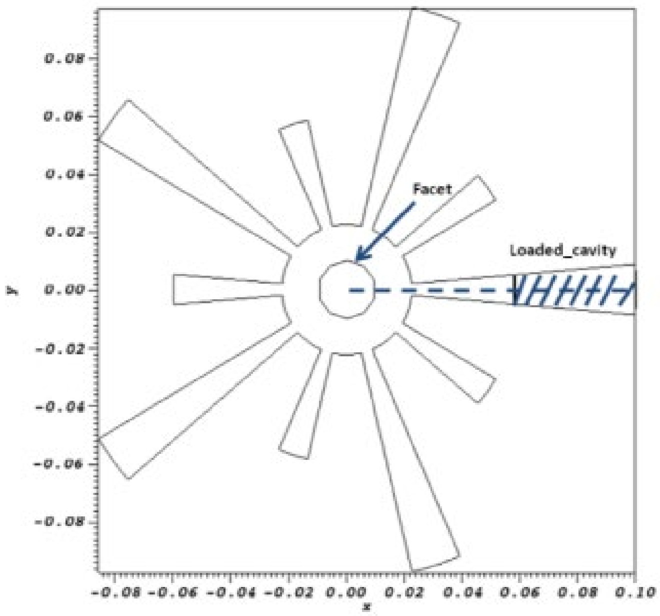

Figure III-4 Geometry model used for the Boise State rising-sun magnetron simulations [28]

Table III-4 Results from the Boise State rising-sun magnetron simulations [28]

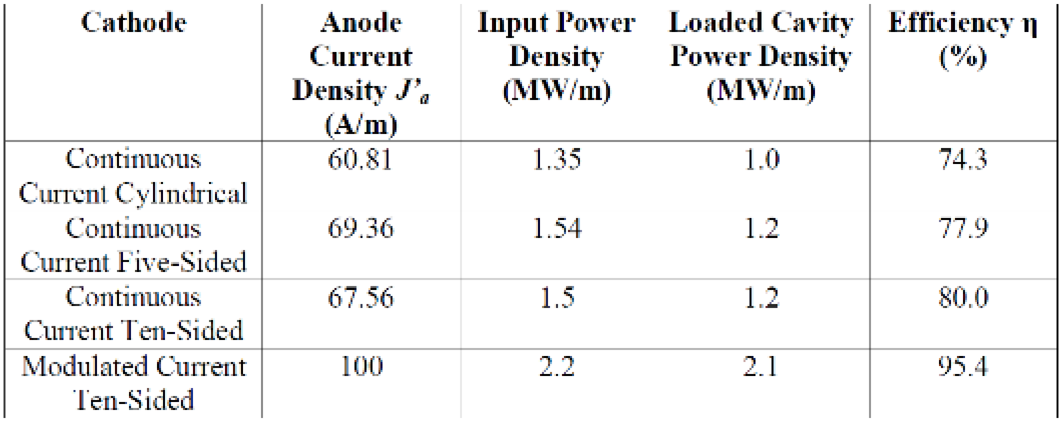

Cathode	Anode Current Density J'_a (A/m)	Input Power Density (MW/m)	Loaded Cavity Power Density (MW/m)	Efficiency η (%)
Continuous Current Cylindrical	60.81	1.35	1.0	74.3
Continuous Current Five-Sided	69.36	1.54	1.2	77.9
Continuous Current Ten-Sided	67.56	1.5	1.2	80.0
Modulated Current Ten-Sided	100	2.2	2.1	95.4

When the ten-sided cathode was used with modulated current injection, the magnetron's startup time was shortened from 110 ns to 50 ns; better power efficiency was also observed. The research also concluded that the modulated, addressable cathode is capable of actively controlling the magnetron startup and RF phase.

Overall, Boise State's 2D rising-sun magnetron simulation supports the feasibility of using a modulated current source in the magnetron for enhanced performance and increased control. The work presented in this document aims to extend the 2D Rising Sun magnetron simulation results into 3D with a commercially available magnetron.

3.4 The University of New Mexico Simulation of the CWM-75/100L

Researchers at The University of New Mexico have simulated the CWM-75/100L magnetron with the 3D PIC code ICEPIC [45-46]. This magnetron is very similar to the L3Harris CWM-75kW simulated as part of this dissertation; the cathode radius and the anode dimensions (anode radius, cavity counts, straps, etc.) are the same. However, the VSim simulation model of the L3Harris CWM-75kW developed as part of this research differs from the ICEPIC simulation model of the CWM-75/100L presented by University of New Mexico in many fundamental ways, which will be discuss in later Chapters. This section focuses on summarizing the simulation setup and results obtained by researchers at The University of New Mexico.

The geometry used in the University of New Mexico simulation is shown in Figure 0-5. The simulated cathode has a cylindrical geometry. The input DC voltage was added into the simulation by an input port at the bottom (lower-z) of the simulation domain, and power extraction was done via the use of three separate output ports at the locations where the three output antenna rods intersect with the top (upper-z) of the simulation domain. An external magnetic field was defined over the entire simulation domain. The researchers at the University of New Mexico did not offer any detailed information regarding the current injection scheme used in the simulation other than the phrase: “space charge limited.” Another important simulation aspect on electron back-bombardment was not clear, which is an important aspect of magnetron physics.

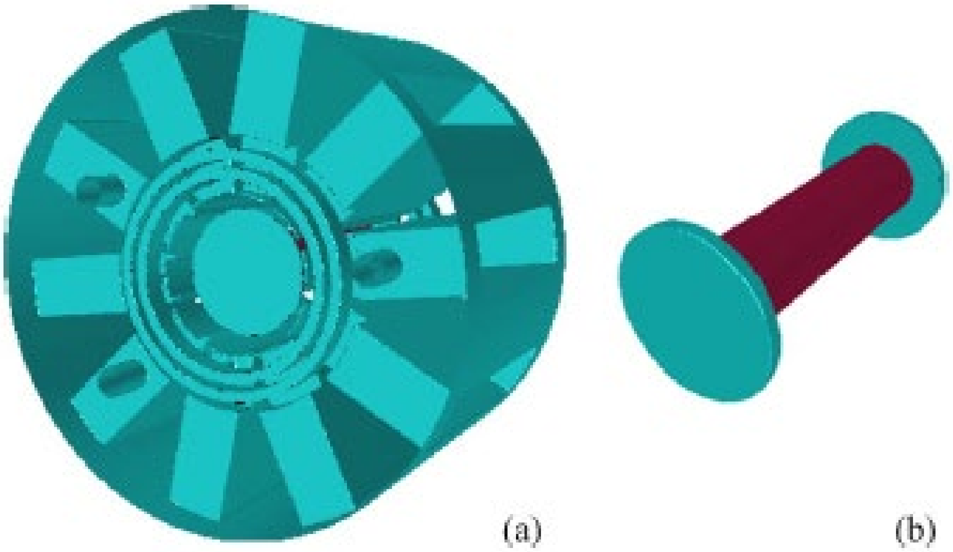

Figure III-5 Geometry used in the University of New Mexico simulation of the CWM-75/100L magnetron. (a) Anode block of the simulation model of the magnetron with solid cathode and three output electrodes, as seen from the output ports. (b) Solid cathode with two end caps. Metallic faces are colored with cyan; electron emitting faces are colored with red [29].

The University of New Mexico simulation produced valuable results with its wide-range parameter sweeps. The researchers were able to study the simulation with many different combinations of the applied DC voltage and the applied magnetic field. The results are summarized in Figure 0-6. With all the operating points plotted in Figure 0-6, the researchers at the University of New Mexico state that the simulated device is capable of reaching oscillation without the aid of any priming techniques.

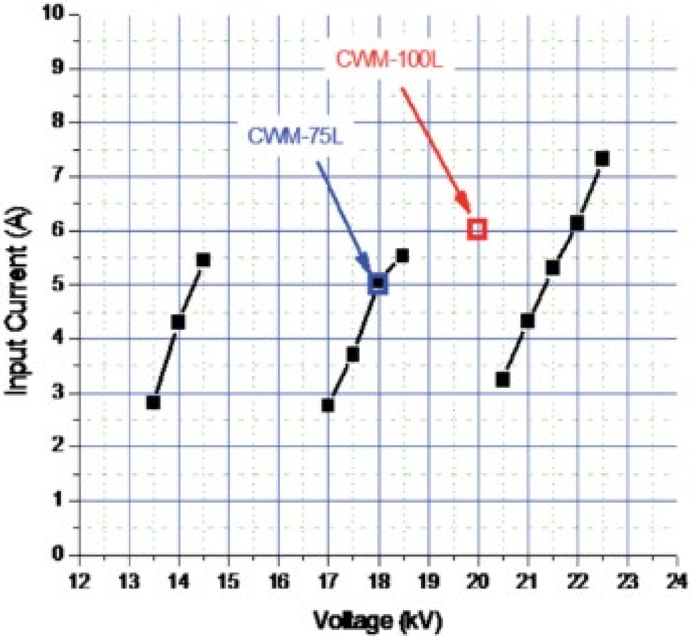

Figure III-6 Summary of the University of New Mexico simulation results. The figure plots input current versus operating voltage at three different magnetic fields: 0.159 Tesla (13.5-14.5 kV), 0.199 Tesla (17.0-18.5 kV), and 0.238 Tesla (20.5-22.5 kV) [47].

CHAPTER FOUR: THE GFEA-BASED CATHODE AND EXPERIMENTAL SETUP

The control of the time and location of electron injection into the interaction region requires the use of an electron source that can be modulated by a control signal. Because of the physical nature of the thermionic cathode, neither the timing nor the location of electron injection can be controlled. Hence, to achieve the goal of controlled electron injection with the high degree of precision required, GFEAs were proposed as the building block of the modulated cathode approach. A field emission cathode, or a "cold cathode," does not always have a gate; however, the inclusion of a gate greatly increases the controllability.

Collaborators at MIT oversee the design and fabrication of the GFEAs that can be integrated into the magnetron cathode. The individual emitters are made of silicon nanowires that are 200 nm in diameter and 10 μm in height, resulting in a high aspect ratio configuration [30]. The emitters have sharp tips that are less than 10 nm in radium for increased field enhancement and the emitter gates are made of polysilicon. These emitters can then be arranged in array formations of various sizes. The structure of the emitter arrays can be seen in Figure 0-1.

The concept of the GFEA-based cathode is shown in Figure 0-2. The image shows a 10-sided cathode in place of the helical cathode thermionic cathode used in the magnetron. The GFEA cathode system used 10 flat plates (facets) to protect the emitters. These plates as well at the rest of the structure shown in Figure 0-2 (a) and (b) are fabricated using a Low Temperature Co-Fired Ceramic (LTCC). The cylindrical cathode

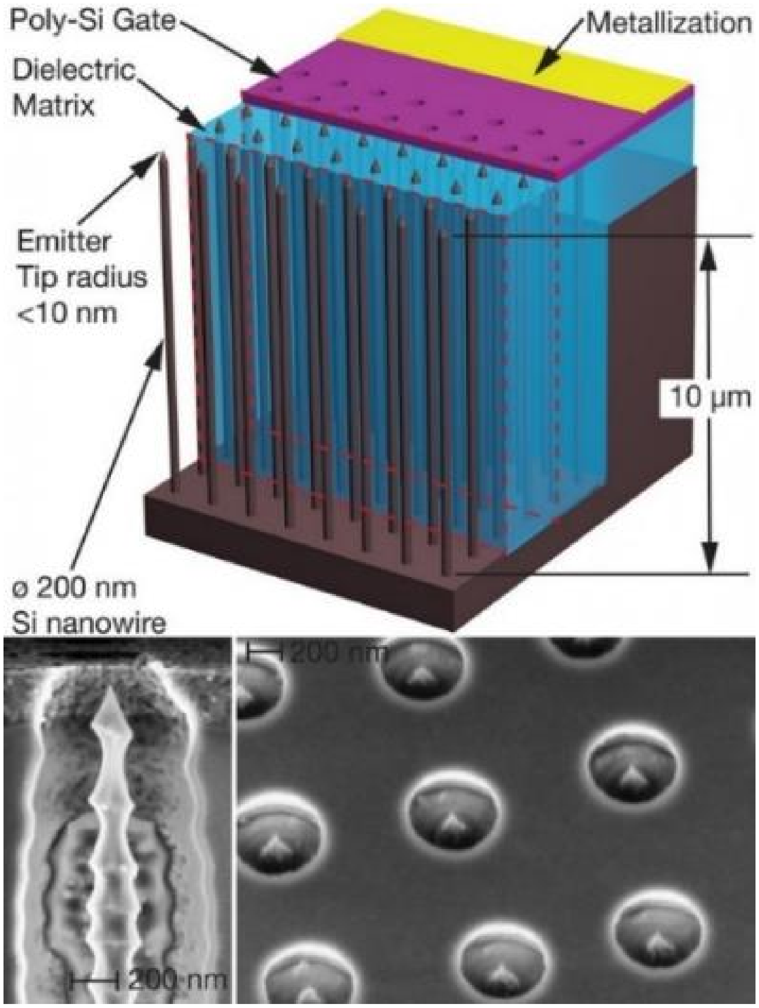

Figure IV-1 Structure schematic (top) and SEM images (bottom) of the MIT GFEAs [30].

structure is separated into 10 facets with GFEA die placed along the structure as shown. Each die, specifically designed and fabricated for this project, is divided into 4 RF phase elements. A fabricated die is shown in Figure 0-2 (d). There are 30 total GFEA die on the cathode structure. The die are placed below the facet plates, which have longitudinal slits. These slits act as electron hop funnels which allow the current to be extracted via secondary electron emission while achieving unity gain. Hence, the GFEAs are protected from the interaction space by the hop funnel structure. L3Harris has shown that the CWM-75kW magnetron can oscillate at only 150 mA, requiring the GFEAs to operate at

~200 mA/cm^2. These GFEAs have been tested but have not yet achieved the uniformity and operating current needed for the magnetron startup.

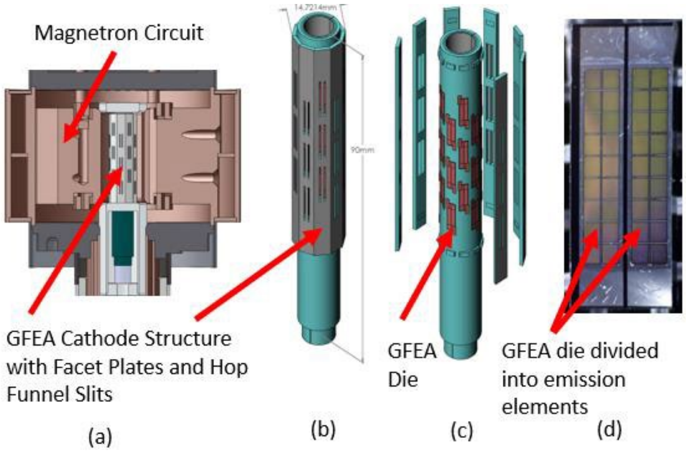

Figure IV-2 (a) Structure design showing cutaway of the magnetron with the GFEA cathode structure located within the circuit, (b) drawing of the cathode structure showing facet plates with hop funnel slits to protect die. There are 10 facet plates, (c) exploded view of cathode structure showing GFEA die placed axially with 30 total die, and (d) photograph of a GFEA die used in the magnetron cathode structure [31].

These die are being redesigned to achieve the required specifications. The entire LTCC cathode test structure has been fabricated and tested including the GFEA die interconnects. However, the phase control is achieved using a helical delay that wraps around the structure with the GFEA die connected through vias. This delay line is still to be designed and modeled. Nevertheless, the use of a 10-sided cathode structure in some of the simulations is predicted on this experimental concept.

CHAPTER FIVE: THE VSIM SIMULATION CODE

5.1 Overview of Magnetron Simulation

In an operating magnetron, there are changing electromagnetic fields, and there are moving electrons. The fields and the electrons are coupled together and exercise simultaneous mutual influence. Electromagnetic fields are governed by Maxwell's equations, and electron motion is determined by the Lorentz equation. Electromagnetic fields change the motions of electrons, and moving electrons induce a current and an electric field which feed back into the electromagnetic fields. In the physical world, this mutual influence between fields and particles occurs instantly; however, in the numerical simulation of this process, calculations of equations must be performed in steps. The major challenge to numerically simulate the magnetron, and MVEDs in general, is that the device requires the simultaneous calculations of both fields and particles within the same system, and these calculations must be self-consistent.

5.2 The Particle-In-Cell Method

The particle-in-cell (PIC) method is a numerical computational method designed to solve particle-field systems such as simulating the magnetron. Although the focus of this document is magnetron simulation, it should be noted here that the PIC method is widely used in simulating many types of MVEDs; it is also used for simulating plasma devices and applications that involve reactions. The use of the PIC method was seen as early as 1955, before the prevalence of computers, in the report titled "A Machine Calculation Method for Hydrodynamic Problems" by Los Alamos scientist F. H. Harlow

[32]. With the PIC method, particle motions are calculated in a Lagrangian frame while fields are calculated on a Eulerian mesh. Or in the words of J. M. Dawson, one of the researchers who laid the foundational work for the PIC method, “the technique follows the motion of a large assembly of charged particles in their self-consistent electric and magnetic fields [computed on a fixed mesh]” [33].

There are a number of PIC codes available today for various applications, among these codes, magnetron studies have been performed with VSim (previously known as VORPAL) [15-17, 47-49], MAGIC [50-54], ICEPIC [55-56], and others [34]. The following discussion of the inner workings of the PIC method will use the VSim code as a reference, but many of these concepts apply to other PIC codes as well.

VSim, as a simulation code, is very different from many well-known simulation software packages. Users of VSim are not bound by any sets of predefined simulation features and options; VSim allows the user access to the most basic level of the simulation and grants advanced users the ability to take complete control over the simulation.

5.3 The VSim Simulation Framework

VSim solves the field-particle system with the particle-in-cell method. The field equations are solved by using the Finite Difference Time Domain (FDTD) method first theorized by the applied mathematician Kane S. Yee [35] with the aid of the Dey-Mittra Algorithm to resolve curved geometries [63-64]. Particle motions are solved by algorithms known as “particle movers.” In VSim, the leapfrog method is used, along with the Boris algorithm for particle push [65-67]. The following sections will discuss these concepts in greater detail.

5.3.1 The Finite-Difference Time-Domain Field Solver

To simulate the electromagnetic fields, the algorithm needs to solve Faraday's equation:

$$\nabla \times \boldsymbol{E} = -\mu_0 \frac{\partial \boldsymbol{H}}{\partial t} \qquad \text{Eq. 0-1}$$

and Ampere's equation:

$$\nabla \times \boldsymbol{H} = \varepsilon_0 \frac{\partial \boldsymbol{E}}{\partial t} + \boldsymbol{J} \qquad \text{Eq. 0-2}$$

where **E** and **H** are the electric and magnetic field vectors, μ_0 and ε_0 are the permeability and permittivity of free space, and **J** is the current density.

The FDTD is one of the methods for solving these equations. The FDTD method breaks the continuous domain down to discrete points (nodes), where fields are computed. The FDTD method can be applied to any coordinate system; however, it is usually applied to the Cartesian coordinate system to avoid complicated distortion factors of the vector field. In three-dimensional Cartesian coordinate system, the curl equations can be expanded to six Partial Differential Equations (PDEs):

$$\frac{\partial H_x}{\partial t} = -\frac{1}{\mu_0}\left(\frac{\partial E_z}{\partial y} - \frac{\partial E_y}{\partial z}\right) \qquad \text{Eq. 0-3}$$

$$\frac{\partial H_y}{\partial t} = -\frac{1}{\mu_0}\left(\frac{\partial E_x}{\partial z} - \frac{\partial E_z}{\partial x}\right) \qquad \text{Eq. 0-4}$$

$$\frac{\partial H_z}{\partial t} = -\frac{1}{\mu_0}\left(\frac{\partial E_y}{\partial x} - \frac{\partial E_x}{\partial y}\right) \qquad \text{Eq. 0-5}$$

$$\frac{\partial E_x}{\partial t} = \frac{1}{\varepsilon_0}\left(\frac{\partial H_z}{\partial y} - \frac{\partial H_y}{\partial z} - \sigma E_x\right) \qquad \text{Eq. 0-6}$$

$$\frac{\partial E_y}{\partial t} = \frac{1}{\varepsilon_0}\left(\frac{\partial H_x}{\partial z} - \frac{\partial H_z}{\partial x} - \sigma E_y\right) \qquad \text{Eq. 0-7}$$

$$\frac{\partial E_z}{\partial t} = \frac{1}{\varepsilon_0}\left(\frac{\partial H_y}{\partial x} - \frac{\partial H_x}{\partial y} - \sigma E_z\right) \qquad \text{Eq. 0-8}$$

where E_x, E_y, E_z, H_x, H_y, H_z are the electric and magnetic field components in Cartesian coordinates, respectively. σ is the conductivity of the medium.

The FDTD method implemented by VSim approximates the derivatives by using the central difference approximation:

$$\delta_h[f](x) = f\left(x + \frac{1}{2}h\right) - f\left(x - \frac{1}{2}h\right) \qquad \text{Eq. 0-9}$$

with h being the spacing between nodes. Note that the value of h can be fixed or variable; usually, a fixed value of h is used for simplicity, but the use of a variable value of h could potentially improve the computational efficiency depending on the geometry used in the simulation model. With the central difference approximation, the PDEs are reduced to algebraic expressions, which can be easily handled by computers.

VSim uses Yee's FDTD method [35]. Within each discretized timestep Δt, for each discretized grid cell (Δx, Δy, Δz), the electric fields are solved at the midpoint of the boundaries of each rectangular cell (referred to as "edgeE" by VSim", while magnetic fields are solved at the center points of the faces of each rectangular cell (referred to as "faceB" by VSim). This arrangement is often referred to as the "Yee cell" or "Yee lattice", as shown in Figure 0-1. In VSim, the solution of Faraday's equation is known as a "Faraday update" and the solution of Ampere's equation is known as an "Ampere update." Note that the Faraday update and Ampere update could be applied more than once within one timestep, when external fields or certain boundary conditions are involved, which will be discussed in later sections.

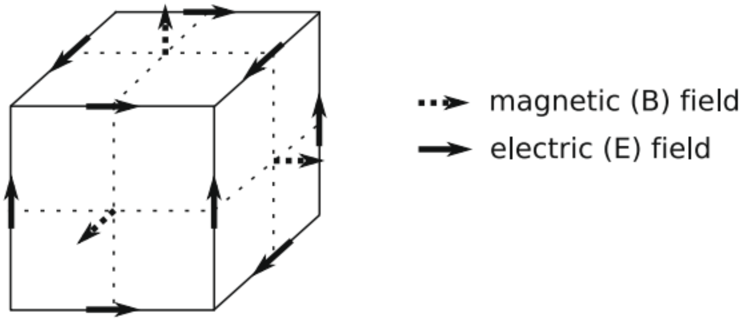

Figure V-1 The Yee cell arrangement showing electric fields being updated on the boundaries of the cell while magnetic fields are being updated at the center point of each face [36].

With spatial discretization, Maxwell's equations can be rewritten as:

$$\frac{d\boldsymbol{b}}{dt} = -\boldsymbol{C} \cdot \boldsymbol{e}, \qquad \text{Eq. 0-10}$$

$$\frac{d\boldsymbol{e}}{dt} = \boldsymbol{C}^{\dagger} \cdot \boldsymbol{b}, \qquad \text{Eq. 0-11}$$

$$\frac{d^2\boldsymbol{b}}{dt^2} = -\boldsymbol{C} \cdot \boldsymbol{C}^{\dagger} \cdot \boldsymbol{b} \equiv -\boldsymbol{D} \cdot \boldsymbol{b}, \qquad \text{Eq. 0-12}$$

where **e** and **b** are column vectors of all electric field components and all magnetic field components at all locations, respectively; $\boldsymbol{C}$ is a forward curl operator and $\boldsymbol{C}^{\dagger}$ is a backward curl operator; the operators $\boldsymbol{C}$ and $\boldsymbol{C}^{\dagger}$ are adjoints of each other, and their dot product $\boldsymbol{D}$ is self-adjoint and positive semi-definite. The matrix $\boldsymbol{D}$ in this context is the finite difference Laplacian operator [36]. These equations are solved by using leapfrog integration to update the fields, with the **E** fields being updated every full time-step, and the **H** fields being updated every half time-step.

5.3.2 Numerical Stability

One simulation constraint that is significant is the speed of light. The computational algorithm will execute regardless of whether the input parameters and the overall setup make sense. In other words, if the simulation were set up, intentionally or unintentionally, to violate the speed of light, the code would do exactly as programmed and return non-physical results. Hence, for the simulation to be stable and its results to be accurate, the timestep size Δt must stay in the bound determined by the size of the spatial discretization Δx, Δy, and Δz. The duration of the timestep must not be longer than the time required for light to cross a cell; this requirement is known as the Courant-Freidrichs-Lewy (CFL) stability criterion [37]:

$$\Delta t < \frac{1}{c\sqrt{\frac{1}{\Delta x^2}+\frac{1}{\Delta y^2}+\frac{1}{\Delta z^2}}} \qquad \text{Eq. 0-13}$$

where c is the speed of light.

5.3.3 The Dey-Mittra Cut-Cell Algorithm

When modeling complex devices involving curved geometries such as the magnetron, it is often unavoidable that the simulation cell grid does not conform to the material boundaries, as shown in Figure 0-2. As a result, it often happens that a material would only partially occupy a cell, making field solving for that cell more complicated. These cells that partially contain a material are known as “cut-cells.”

A common approach to address this cut-cell issue is the staircase approximation, as illustrated in Figure 0-3, which has been shown to be first-order accurate [38]. With this approach, if a material occupies a majority volume of a cell, then the fields for the cell would be calculated as if it is entirely filled with the material, and vice versa. This approach, while simple to implement, can result in large numerical errors when the simulation grid is coarse due to its first-order nature.

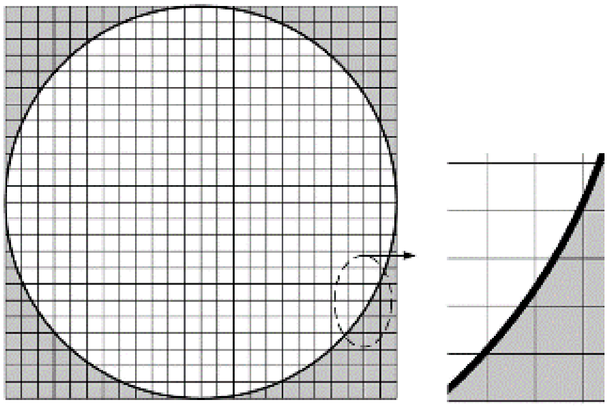

Figure V-2 Example of the case when simulation grid does not conform to the material boundary (bold black line) [39].

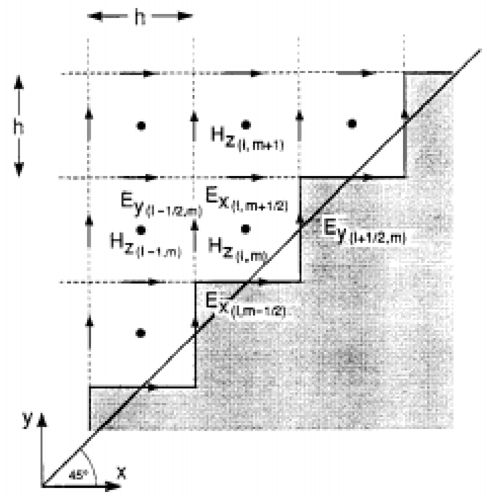

Figure V-3 Illustration of the staircase approximation for material boundaries crossing through FDTD grids [38]. The diagonal line represents a material boundary.

The VSim code addresses the cut-cell issue by adapting an advanced algorithm developed by Dey and Mittra [40], which has been shown to be second order accurate [36]. With the notations used in section 5.3.1, the Dey-Mittra algorithm can be written as:

$$\frac{d^2\boldsymbol{b}}{dt^2} = -\boldsymbol{A}^{-1} \cdot \boldsymbol{C} \cdot \boldsymbol{L} \cdot \boldsymbol{C}^{\dagger} \cdot \boldsymbol{b} \equiv -\boldsymbol{D}' \cdot \boldsymbol{b} \qquad \text{Eq. 0-14}$$

with **A** being a diagonal matrix containing the area fractions of each face outside of the material, and **L** being a diagonal matrix containing the length fractions for each edge corresponds to an element of **e**. With these added terms, the magnetic field update becomes a line integral around the face:

$$\frac{d\Phi_B}{dt} = \frac{A_{xy} dB_z}{dt} = -\oint \boldsymbol{E} \cdot d\boldsymbol{l} \cong -\sum \boldsymbol{E}_i \cdot \boldsymbol{l}_i \, , \qquad \text{Eq. 0-15}$$

where Φ_B is the magnetic flux though the face, A_{xy} is the area of the cut face, and $\boldsymbol{l}_i$ is the length of the cut-cell sides [36].

It is important to note that the area used in the cut-cell updater effectively reduces the area of the cell boundary. This reduced cell boundary still needs to obey the CFL stability criterion, and the maximum allowable timestep size (Δt) is determined by the smallest cell boundary. While VSim implements "area borrowing" schemes such as the Zagorodnov boundary algorithm [41], which "borrows" area from neighboring cells (if the cell is cut by more than a half) to maintain stability when the Dey-Mittra algorithm is used [42], a purely second order cut-cell could still dramatically tighten the CFL bound, which directly translates to longer computation time. For this reason, VSim introduced a parameter known as "dm_frac" (also referred to as "surface mesh tolerance") to allow the user to set the fraction of the second-order approximation used in the simulation.

5.3.4 Macroparticles

In an operating physical magnetron, there can be many trillions of electrons in the interaction space. It is computationally infeasible to track the motion of every physical electron; instead of simulating physical electrons, PIC codes usually simulate "macro-particles" (also known as "super-particles"), which are bunches of physical electrons. For example, for a macro-particle size of 10^5, the PIC code would consider 10^5 physical electrons as one particle that has both the mass and charge of 10^5 electrons. Instead of computing the motion of all 10^5 electrons, the PIC code now only needs to compute the motion of a single entity, which reduces the overall computational burden on particle motions by a factor of 10^5.

This type of particle lumping is feasible because the force acting on a charged particle (recall from section 2.1.2) is governed by the equation:

$$\boldsymbol{F} = q\boldsymbol{E} + q\boldsymbol{v} \times \boldsymbol{B} = q(\boldsymbol{E} + \boldsymbol{v} \times \boldsymbol{B}), \qquad \text{Eq. 0-16}$$

Rearranging by applying Newton's second law of motion yields:

$$\boldsymbol{a} = \frac{q}{m}(\boldsymbol{E} + \boldsymbol{v} \times \boldsymbol{B}), \qquad \text{Eq. 0-17}$$

where m is the particle mass and **a** is the particle acceleration. This equation shows that the acceleration of a charged particle in an electromagnetic field depends only on its charge-to-mass ratio; therefore, a macro-electron will follow the same trajectory as a physical electron would as long as the same charge-to-mass ratio is maintained.

Note that some physics, however little, will still be lost when lumping physical electrons into macro-particles, so a larger macro-particle size can lead to more inaccurate results. It is up to the code user to determine the optimal balance between speed and accuracy.

5.3.5 Nodal Fields

Since electric fields are solved at the mid-points of grid boundaries and magnetic fields are solved on the center-points of grid faces, they cannot be directly used for calculating particle motions because particles within the cell can be at any location. For this reason, particle motions are solved by using nodal fields, which are spatial averages of the fields on the Yee lattice.

5.3.6 The Boris Particle Mover

Analogous to the FDTD field solving scheme, particle motion is also solved by the leapfrog method. This approach means that the particle mover has the same timestep size constraints as the field solver (the CFL stability criterion) [43]. In its generic form, the leapfrog equations for particle motion at the (k+1)th timestep can be written as:

$$\frac{\boldsymbol{x}_{k+1} - \boldsymbol{x}_k}{\Delta t} = \boldsymbol{v}_{k+\frac{1}{2}}, \qquad \text{Eq. 0-18}$$

$$\frac{\boldsymbol{v}_{k+\frac{1}{2}} - \boldsymbol{v}_{k-\frac{1}{2}}}{\Delta t} = \frac{q}{m}\left(\boldsymbol{E}_k + \frac{\boldsymbol{v}_{k+\frac{1}{2}} + \boldsymbol{v}_{k-\frac{1}{2}}}{2} \times \boldsymbol{B}_k\right), \qquad \text{Eq. 0-19}$$

where **x** is the particle position and **v** is the particle velocity. The equations above have the advantage of being very intuitive; however, their structures are not suitable for direct computation due to the intermingled timesteps. The computer-executable algorithm of the leapfrog method is known as the Boris algorithm, named after J. P. Boris, who formalized the algorithm in his 1970 paper [44]. The Boris algorithm takes on the following form:

$$\boldsymbol{x}_{k+1} = \boldsymbol{x}_k + \Delta t \cdot \boldsymbol{v}_{k+\frac{1}{2}}, \qquad \text{Eq. 0-20}$$

$$\boldsymbol{v}_{k+\frac{1}{2}} = \boldsymbol{u}' + q' \cdot \boldsymbol{E}_k, \qquad \text{Eq. 0-21}$$

with

$$\boldsymbol{u}' = \boldsymbol{u} + \big(\boldsymbol{u} + (\boldsymbol{u} \times \boldsymbol{h})\big) \times \boldsymbol{s}, \qquad \text{Eq. 0-22}$$

$$\boldsymbol{u} = \boldsymbol{v}_{k-\frac{1}{2}} + q' \cdot \boldsymbol{E}_k, \qquad \text{Eq. 0-23}$$

$$\boldsymbol{h} = q' \cdot \boldsymbol{B}_k, \qquad \text{Eq. 0-24}$$

$$\boldsymbol{s} = \frac{2\boldsymbol{h}}{1 + h^2}, \qquad \text{Eq. 0-25}$$

$$q' = \Delta t \times \left(\frac{q}{2m}\right). \qquad \text{Eq. 0-26}$$

Note that velocities are calculated at half timesteps, analogous to the **H** field in the field computation scheme.

5.3.7 Section Summary

With all the concepts discussed above, the basic framework of the VSim simulation code can be pieced together. In VSim, the FDTD field updater and the Boris particle mover are both executed within every timestep after initialization until some termination condition is reached. Note that this is the basic framework of VSim, since it is the same for every simulation involving fields and particles (but no reaction), and these algorithms are not intended to be altered by the user.

5.4 User-Setup Elements in VSim

With the basic VSim framework established, it is then up to the user to setup various simulation elements to initialize the simulation and complete the iterative workflow. There are a large number of user-setup simulation elements, but overall, they fall into five general categories: initialization, domain boundary conditions, external fields, particles, and histories.

5.4.1 Initialization

The term "initialization" refers to a sequence of commands that are executed at the beginning of the simulation before the simulation algorithm enters the main loop. The first task of any VSim simulation is the definition of the simulation domain and the subdividing of this domain into grid cells. The dimensions of the simulation domain and the grid cell configurations are determined by the user, but when performing this step, the user must be aware of the impact these dimensions and configurations have on the maximum allowable timestep size due to the CFL constraint.

Once the simulation domain is setup and subdivided, the next step is geometry definition. Geometry definition is, in essence, a boundary condition definition. But unlike the boundary conditions to be discussed in later sections, the geometry boundary is only defined at the beginning of the simulation and does not update with each timestep. VSim allows the user to directly import supported computer-aided-design CAD files, or geometries can be constructed by using functions. After the simulation geometry is defined, VSim then removes cells within its volume that are completely filled with a perfect electric conductor (PEC) from the simulation, so that no calculation is performed within these cells in order to conserve computational resources.

5.4.2 Domain Boundary Conditions

Because the simulation domain is bounded spatially, rules regarding field interaction with the domain boundary must be clearly defined. Many different types of field boundary conditions are offered by VSim [45], and different field boundary conditions are suitable for different setups. For example, if the user intended to simulate infinite vacuum space outside of the simulation domain, then an “open” field boundary is often used; in this case, when field vectors reach the domain boundary, VSim would simply delete these vectors. If the user intended to have the simulation as an enclosed metal box, then a “PEC” field boundary condition can be applied; VSim would remove only the tangential components of the electric field vectors at the boundary, while reflecting the normal components back into the simulation domain with a 180° phase shift. More complex field boundary conditions include the matched absorbing layer (MAL) boundary condition. This boundary condition is used for simulating the field loading effects and requires extensive user setup. The use of the MAL boundary condition will be discussed in greater detail in later chapters as it is an important part of the simulation setup for the CWM-75kW magnetron model.

Domain boundary conditions can not only remove field vectors at the domain boundaries, they can also be used to launch fields into the simulation. User-defined fields, static or time-varying, can be written to the domain boundaries at every timestep, allowing the user to input external signals into the simulated device or to define a constant electric field between two geometry boundaries to establish a DC voltage.

Note that each domain boundary is setup individually, and there can be multiple boundary conditions applied to the same boundary. It is often up to the user to ensure these boundary conditions are mutually compatible. Masking functions can also be used to only apply conditions to specified regions on the domain boundary.

Domain boundary conditions are dynamic in nature so they must be applied within every timestep. The order by which the boundary conditions are applied in the iterative workflow, especially whether they are applied before or after the field updaters and/or particle movers, can be critical to the success of the simulation.

5.4.3 External Fields

External fields are user-defined field vectors, static or time-varying, that are written to specified regions of the simulation domain (can be the entire simulation domain). External fields are used to define applied magnetic fields. They are also used to apply specific types of "priming" to the simulation model. The topic of priming will be discussed later in this chapter.

Similar to domain boundary conditions, external fields are calculated and applied within every timestep. Their placement in the workflow can also have a profound impact on the simulation results.

5.4.4 Particles

The setups of particle sources and sinks are integral parts of VSim simulations, but before setting up sources and sinks, the user must define the "species" of particles to be simulated. In simulation of electron devices like magnetrons, electrons are the only species involved. But it should be noted that VSim supports the simulation of various types of ions and the complex interactions between different species of charged particles.

The definition of electron source requires the user to setup the scheme by which the macroparticle size is calculated; the user also needs to setup the scheme by which electrons are emitted. VSim supports various electron emission models ranging from a simple current density flux to more complex thermionic and field emission models. The details of these models will be discussed on a case-specific basis in later chapters. Lastly, the user needs to inform VSim where and when to emit electrons. Electrons can be emitted from an entire surface throughout the duration of the simulation or emitted only from user-specified regions on a surface during user-specified times. VSim also allows the user to attach unique identifiers known as "particle tags" to every emitted particle, which enables the development of sophisticated diagnostics to study particle trajectories.

Electron sinks are usually defined on metallic (PEC) surfaces; electrons are absorbed and recorded when coming into physical contact with the electron sink and then removed from the simulation. At this current stage, VSim does not incorporate any thermodynamic models and does not account for the heating effect that occurs when kinetic electrons strike a metal surface.

5.4.5 Histories

Histories are user-defined items for VSim to keep track of throughout the simulation. These items include but are not limited to voltages between various coordinates, current emitted and/or absorbed, particle counts, particle energy, and Poynting flux through certain planes, etc. By default, VSim keeps track of datasets containing all the field vectors (**E, H, J**) and particle attributes (**x**, **v**, macroparticle size, tag) within each timestep, since the field solver and particle mover relies on these datasets for calculation; however, because of the extraordinary size of these data sets and the fact that these datasets are updated every timestep, these datasets are only temporally stored in RAM unless the user requests VSim to make permanent copies of them (known as “data dumps”). On the other hand, histories are recorded at the end of every timestep due to their minuscule sizes (usually a single entry per item per timestep).

5.5 Complete VSim Workflow

Now, the complete VSim workflow can be pieced together with some additional nuances, as illustrated in graphical form in Figure 0-4. The FDTD field solver and the Boris particle mover are executed side-by-side with inter-dependencies. Note that although both the Ampere update and the particle velocity update are performed at half timesteps, they are not performed simultaneously. The Ampere update is performed first, then the Faraday updater was applied a second time to line up the timings of the **E** and **H** fields for the computation of the nodal fields, which are used to update the particle velocities.

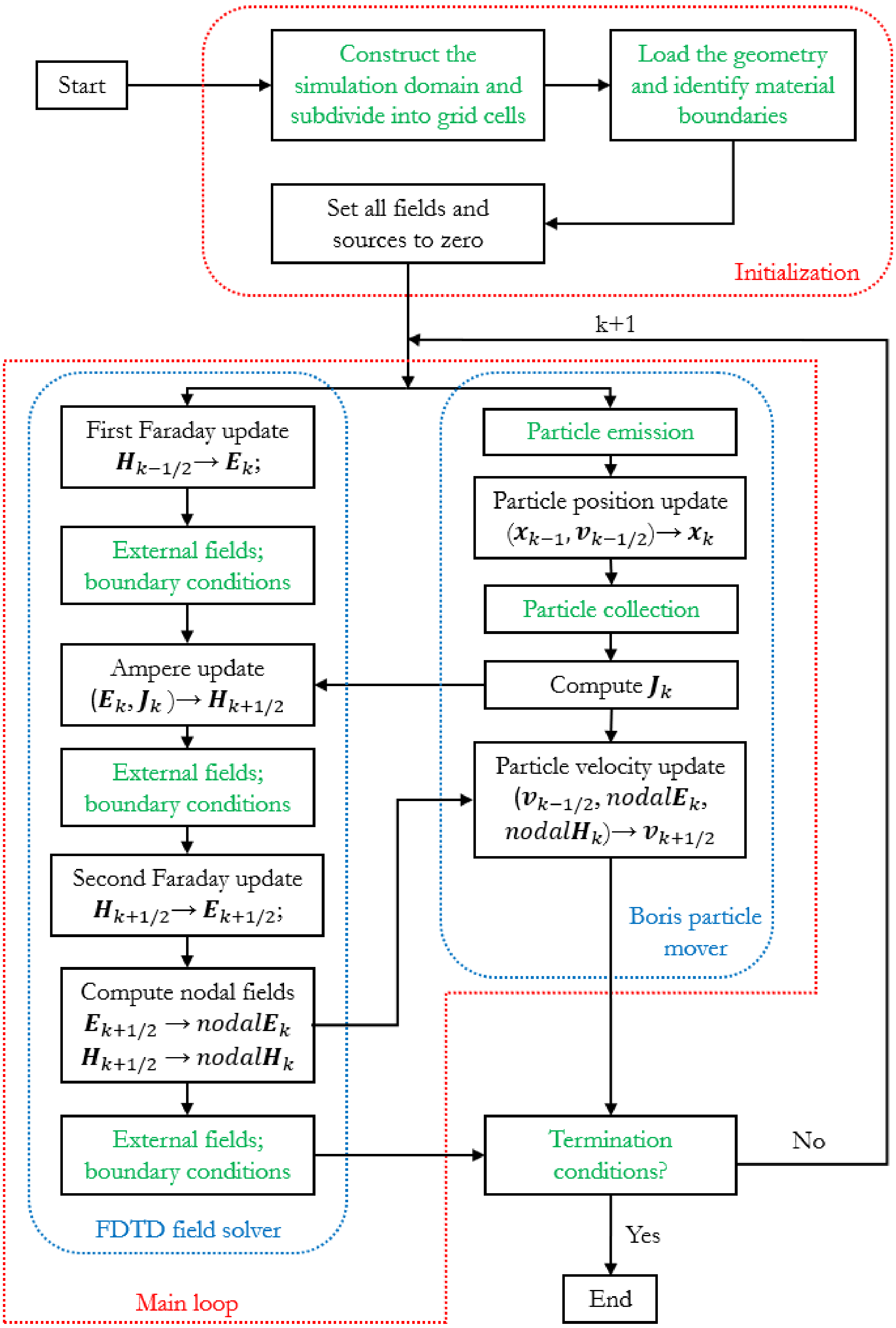

Green: User specified elements

Figure V-4 Complete VSim simulation workflow.

5.6 The Concept of Priming

In the physical operation of magnetrons, startup can take up to milliseconds depending on the type of magnetron. Since the timestep size for this type of simulation is usually a fraction of a picosecond, it is unfeasible to simulate milliseconds. For this reason, researchers may use “priming” techniques to dramatically shorten the simulation startup times. The essence of priming is to use a driving force of some kind to create an environment that the primed device would be operating in when steady state is reached. This driving force is then shut down, either before or after the simulation reaches steady state, and the simulated device is allowed to operate without priming.

For the specific case of the magnetron, priming involves creating an environment that drives the magnetron to quickly start oscillating in the desired mode, usually the π-mode. This is usually performed in one of three different ways:

1. RF priming, by which RF driving currents are defined in the magnetron cavities to drive oscillation in the π-mode [46].
2. B field priming, by which the magnetic field in the interaction region is modulated to drive oscillation in the π-mode [47].
3. Cathode priming, by which the electron injection pattern is manipulated in ways that promote oscillation in the π-mode [28], [48], [49].

Note that both RF priming and B field priming are simulation techniques, since they involve fields being defined into the simulation, though it should be noted that some RF-priming-like techniques such as RF back injection via the use of phase locked loops has been researched quite extensively in recent years [77-79]. On the other hand, with the GFEAs-based cathode discussed in Chapter four, cathode priming is potentially feasible.

The examination of magnetron cathode priming in simulations is one of the core-focuses of this research.

CHAPTER SIX: DATA ANALYTICS

6.1 Types of VSim Simulation-Generated Data and Their Formats

The data generated by a VSim simulation can be divided into two categories. The first category contains all the data tracked by user-defined histories. These are relatively small datasets; each dataset usually only contains a single column of double precision entries. The small sizes of these history data sets allow them to be tracked and recorded every timestep. The second category contains particle and field data; these are very large datasets. To put the size of these datasets in context, for the CWM-75kW simulation model, the combined size of particle and field datasets per timestep usually exceed 500 MB, and a typical 300 ns simulation takes around 600,000 timesteps to complete. Recording the particle and field data for every timestep would result in 300 TB of data; hence, particle and field data are usually recorded periodically, like once per 1,000 timesteps, and this recording period is known as a “dump period.” The word “dump” refers to the process in which data is copied from random access memory (RAM) to some form of non-volatile media for permanent storage. Note that a data dump basically acts as a snapshot of the instantaneous particle and field state of the simulation; the particle and field states between dumps would be unknown to the user, since they are updated and overwritten in RAM with the progression of each timestep.

VSim outputs data in HDF5 (Hierarchical Data Format 5), which is a data structure instead of a simple matrix; additional processing is required to access the data matrix. Figure 0-1 shows a sample electron data matrix from a single data dump after some basic processing (coordinate system conversion and time stamp attachment). Each row of the matrix represents information about one electron; the first three columns show the special position of the electron in three-axis; columns 4-6 show the velocities of the electron in three-axis; column 7 shows the particle's tag (not activated in the example); column 8 shows the macroparticle weight, and column 9 is the time stamp. The example shown omits more than one million rows; hence, one data matrix has around ten million entries, and all entries are in double precision.

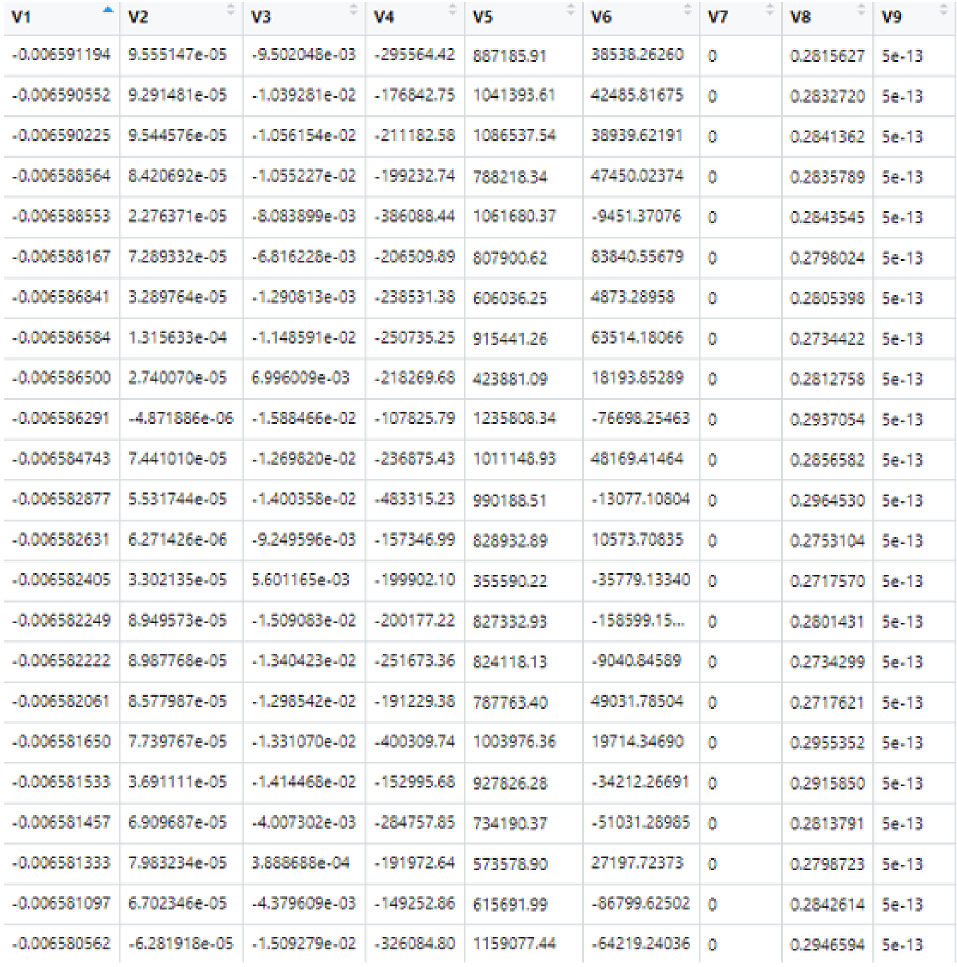

V1	V2	V3	V4	V5	V6	V7	V8	V9
-0.006591194	9.555147e-05	-9.502048e-03	-295564.42	887185.91	38538.26260	0	0.2815627	5e-13
-0.006590552	9.291481e-05	-1.039281e-02	-176842.75	1041393.61	42485.81675	0	0.2832720	5e-13
-0.006590225	9.544576e-05	-1.056154e-02	-211182.58	1086537.54	38939.62191	0	0.2841362	5e-13
-0.006588564	8.420692e-05	-1.055227e-02	-199232.74	788218.34	47450.02374	0	0.2835789	5e-13
-0.006588553	2.276371e-05	-8.083899e-03	-386088.44	1061680.37	-9451.37076	0	0.2843545	5e-13
-0.006588167	7.289332e-05	-6.816228e-03	-206509.89	807900.62	83840.55679	0	0.2798024	5e-13
-0.006586841	3.289764e-05	-1.290813e-03	-238531.38	606036.25	4873.28958	0	0.2805398	5e-13
-0.006586584	1.315633e-04	-1.148591e-02	-250735.25	915441.26	63514.18066	0	0.2734422	5e-13
-0.006586500	2.740070e-05	6.996009e-03	-218269.68	423881.09	18193.85289	0	0.2812758	5e-13
-0.006586291	-4.871886e-06	-1.588466e-02	-107825.79	1235808.34	-76698.25463	0	0.2937054	5e-13
-0.006584743	7.441010e-05	-1.269820e-02	-236875.43	1011148.93	48169.41464	0	0.2856582	5e-13
-0.006582877	5.531744e-05	-1.400358e-02	-483315.23	990188.51	-13077.10804	0	0.2964530	5e-13
-0.006582631	6.271426e-06	-9.249596e-03	-157346.99	828932.89	10573.70835	0	0.2753104	5e-13
-0.006582405	3.302135e-05	5.601165e-03	-199902.10	355590.22	-35779.13340	0	0.2717570	5e-13
-0.006582249	8.949573e-05	-1.509083e-02	-200177.22	827332.93	-158599.15...	0	0.2801431	5e-13
-0.006582222	8.987768e-05	-1.340423e-02	-251673.36	824118.13	-9040.84589	0	0.2734299	5e-13
-0.006582061	8.577987e-05	-1.298542e-02	-191229.38	787763.40	49031.78504	0	0.2717621	5e-13
-0.006581650	7.739767e-05	-1.331070e-02	-400309.74	1003976.36	19714.34690	0	0.2955352	5e-13
-0.006581533	3.691111e-05	-1.414468e-02	-152995.68	927826.28	-34212.26691	0	0.2915850	5e-13
-0.006581457	6.909687e-05	-4.007302e-03	-284757.85	734190.37	-51031.28985	0	0.2813791	5e-13
-0.006581333	7.983234e-05	3.888688e-04	-191972.64	573578.90	27197.72373	0	0.2798723	5e-13
-0.006581097	6.702346e-05	-4.379609e-03	-149252.86	615691.99	-86799.62502	0	0.2842614	5e-13
-0.006580562	-6.281918e-05	-1.509279e-02	-326084.80	1159077.44	-64219.24036	0	0.2946594	5e-13

⋮

(1M+ Rows Omitted)

Figure VI-1 Sample electron data generated by VSim at one instance of time.

6.2 External Information and Internal Information

In the context of this document, “external information” refers to the simulation-generated data that can be directly accessed and plotted by the user with minimal to no processing. For the magnetron simulations that this research is concerned with, notable datasets that fall into the classification of “external information” are:

- Voltages within the resonant cavities and their Fast Fourier Transforms (FFTs)
- DC voltage between the cathode and the anode
- Strength of the applied magnetic field
- Current emitted from the cathode
- Current absorbed by the anode
- Current absorbed by the cathode (back-bombardment current)
- The total number of particles in the simulation
- Output power level
- Instantaneous electron positions
- Instantaneous electric and magnetic fields

On the other hand, “internal information” refers to the datasets and plots that are not directly generated by the simulation; instead, they are derived from various simulation-generated data via means such as statistical processing and mathematical transformations. The derivation of internal information usually involves computationally heavy and mathematically complex processes.

External information and internal information are not mutually exclusive; rather, internal information is derived from external information. The goal of deriving internal information is to gain additional insights into magnetron startup physics that are not easily noticeable by observing external information. It was noticed in the process of this research that external information, such as the datasets noted above, show the results of magnetron startup physics, but give little insight into what the physics are. Hence, techniques were developed to reveal the internal information that are hidden in the simulation results in an attempt to explain why certain events, such as magnetron oscillation, happen rather than to simply observe their occurrences.

6.3 Cross-Sectional Analysis and Time-Series Analysis

By default, simulation-generated data which contains particle and field states is cross-sectional, meaning all observed entities (electrons, fields, etc.) within a given dataset are at the same time instance. Cross-sectional analysis processes the data within the timestep, and the processed results from different timesteps are only linked together at the final stage of analysis. On the other hand, in time-series analysis, the observed entities are tracked and analyzed in temporal order across different timesteps. In the context of analyzing magnetron simulation results, cross-sectional analysis can generate useful statistics such as distributions of electron positions and velocities at a given time and linking these statistics together would reveal how electron position distributions and velocity distributions change over time. Time series analysis with the aid of particle tags discussed in section 5.4.4 enable the tracking of unique particle trajectories, which enables studies into how the cycloid radius of the particle trajectories behave at different stages leading up to magnetron oscillation and how these behaviors are autocorrelated.

6.4 Cross-Sectional Electron Population Analysis

Analysis techniques have been developed as a major part of this work to generate statistics of the attribute of the electron population and of how these statistics are impacted by different priming conditions. Codes have been developed to extract the radial position distributions, radial velocity distributions, azimuthal position distributions, and azimuthal velocity distributions of the electrons as functions of time. The specialty data analytic language R was used for the analysis below; the language was selected for its ability to handle high data throughput and its exceptional computational scalability.

The electron population analysis is a cross-sectional analysis. The method analyzes all electrons within the same time instance; then it attaches results from all time-instances together to form a complete picture. All calculations were performed within the data matrices of individual time instances; this approach is the reason that electron tags were not needed for this analysis.

For this cross-sectional analysis, only the first six columns of each data matrix are used; the R code first parallel reads all *m* number data dumps and converts all data points from Cartesian coordinates to cylindrical coordinates. The code then works on individual data dumps; within each data dump, for each column, the user identifies the relevant data range (for example, the relevant data range for the r position would be from the cathode radius to the anode radius) and equally divides this data range into *n* sub-ranges. Then the code bins the entries within each column into their sub-ranges. Lastly, the code counts the number of elements within each bin and divides this number by the total number of elements, which yields **the normalized probability** of a random element falling into a particular bin. This process applies to every column in the first six columns. After this processing scheme, every data matrix has n rows, and the **entries in every column sum to 1**. Now, the code extracts every individual column and attaches all the columns that have the same column number across all data matrices and orders them by time. This process results in six matrices (separated positions and velocities statistics in three axes) each having n rows and m columns.

To illustrate the meaning of these matrices, without loss of generality, the first matrix would have all the r positional values, which is the distance of the electron from the cathode. The rows represent the probability that an electron is a certain distance from the cathode; the column would represent time. The range of r has a minimum of the cathode radius and a maximum of the anode radius. Note that this radius is the inner most radius of the anode vanes. After being divided into n bins, the $\lceil n/2 \rceil$th row represents the likelihood of a particle being found at the half-way point between the cathode and the anode; likewise, the entry at the cross-point of the $\lceil n/2 \rceil$th row and the $\lceil m/2 \rceil$th column would represent the likelihood of finding an electron at the half-way point between the cathode and the anode when the time is at half of the total simulation time. These matrices can then be plotted as **intensity plots** to give visualizations of the charge in these quantities over time. For example, in this magnetron research the radial position, azimuthal position, radial velocity, and azimuthal velocity are rendered as intensity plots. A simplified flowchart illustrating this processing scheme is shown in Figure 0-2. Note that for electron datasets generated from 2D simulations, only the first 4 columns of the electron data matrices are needed, since there would only be 2 axes, so the index v would only go up to 4 instead of 6.

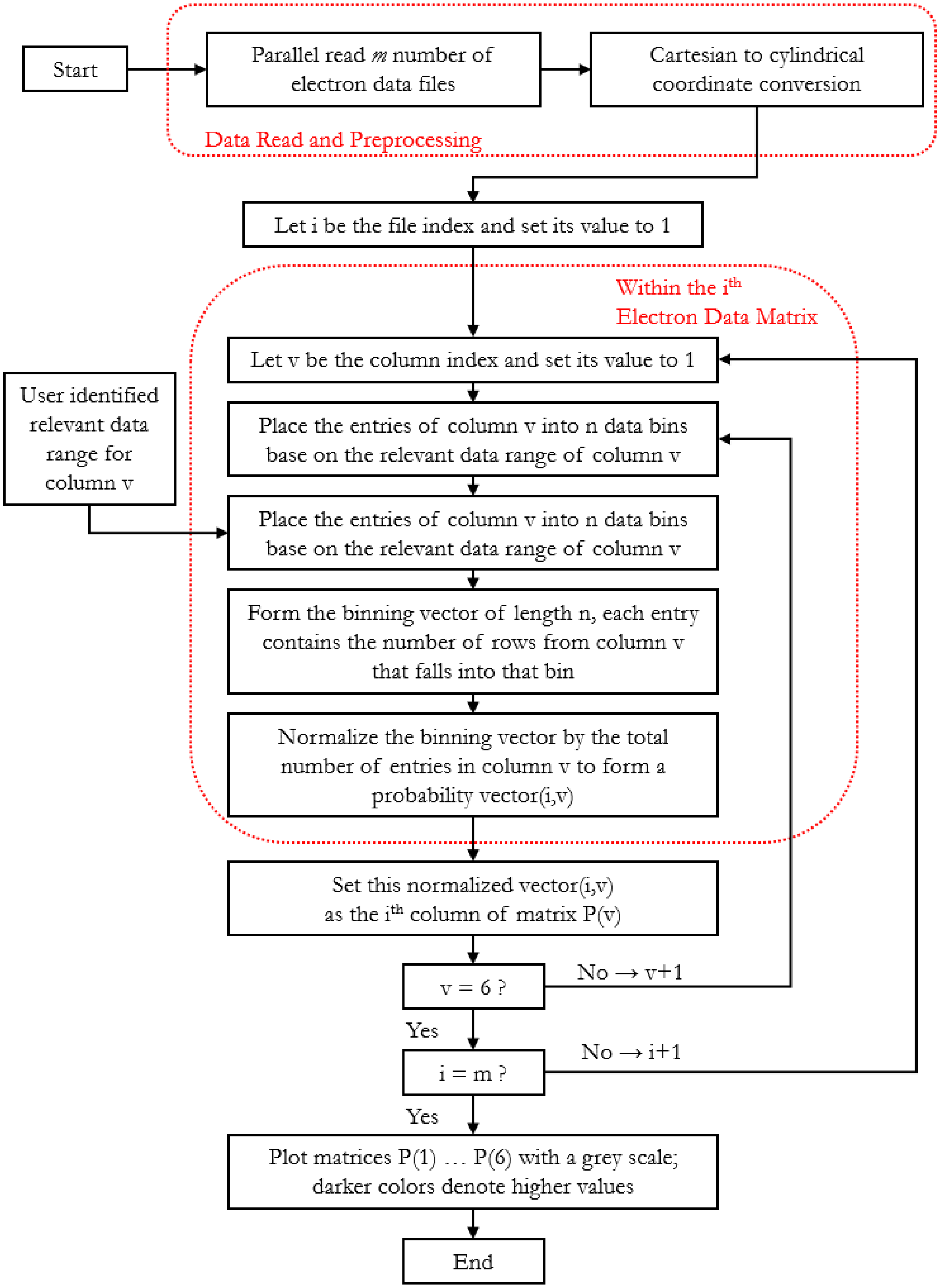

Figure VI-2 Simplified flowchart of the data processing scheme.

6.5 Breadth Ratios

The breadth ratio analysis is developed to visualize directional behaviors of electron motion on a large scale. This analysis is also known as an “advancer vs. decliner” analysis [50]. First, a “direction of advancement” is defined. In the radial direction, the positive radial direction is defined as the direction of advancement since electrons move from the cathode to the anode in an oscillating magnetron. In the azimuthal direction, the direction of advancement is the direction of electron spoke rotation, which can be the positive azimuthal direction or the negative azimuthal direction depending on the direction of the applied magnetic field.

In the radial direction, a particle with a positive radial velocity is considered an “advancer” and a particle with a negative radial velocity is considered a “decliner.” In the azimuthal direction, a particle traveling in the direction of spoke rotation is considered an “advancer” and a particle traveling in the direction counter to the direction of spoke rotation is considered a “decliner.” The breadth ratios are the ratios between the number of electron macroparticle advancers and decliners in each individual axis.

The subcategorization of particles into advancers and decliners arises from the cycloidal nature of electron motion in the presence of a cross-field. In a way, the breadth ratios describe how cycloidal the electron motions are. For the bulk of the electrons to migrate toward the anode, the breadth ratio in radius must be greater than 1:1, which would indicate there are more advancers than decliners. By the same principle, the breadth ratio must hold above 1 for maintaining charge transfer from the cathode to the anode. In the azimuthal direction, a low breadth ratio would indicate the electrons are highly cycloidal; in the case when the electron cycloidal flow collapsed to Brillouin flow as discussed in section 2.2.2, the breadth ratio in azimuth should have a very large value (ideally approaching infinity). Figure 0-3 illustrates the relationship between the electron cycloidal motion and the breadth ratio in azimuth discussed above. A more cycloidal electron has a higher portion of its overall trajectory in the azimuthally declining state; an electron population made up with a higher portion of cycloidal electrons would have a lower breadth ratio in azimuth. By the same principle, the breadth ratio in azimuthal would increase in the positive direction when the electrons are less cycloidal and lesser portions of their trajectories are in the azimuthally declining state. If the electron population is in Brillouin flow, then ideally there would be no declining electrons, which would lead to an ideally infinite breadth ratio in azimuth.

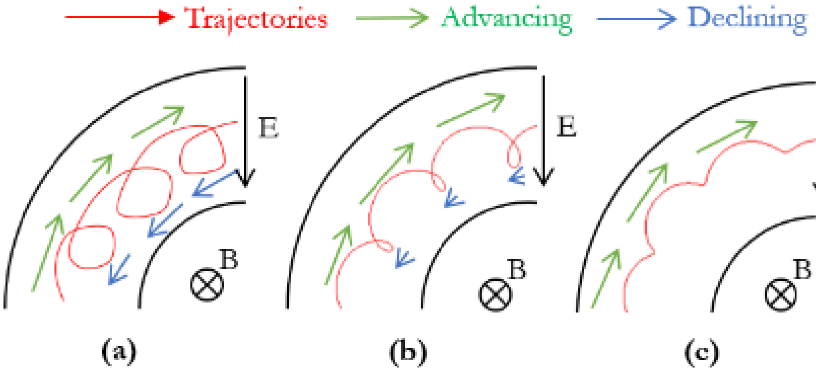

Figure VI-3 Illustration of the relationship between the electron cycloidal motion and the breadth ratio in azimuth. (a) A highly cycloidal electron; (b) a less cycloidal electron; (c) a near-Brillouin flow electron [51].

CHAPTER SEVEN: SIMULATION OF THE RISING SUN MAGNETRON

7.1 Simulation Setup for the Rising Sun Magnetron

The geometry of the Rising Sun magnetron was constructed with CAD drawings based on dimensions used in previous research [15-17]. Two sets of geometries were constructed, one with a cylindrical cathode (Figure 0-1) and the other with a 10-sided faceted cathode (Figure 0-2); the relevant dimensions are summarized in Table 0-1.

The simulation domain has a dimension of 204 mm by 204 mm and was divided into 2 mm by 2 mm cells. The resulting simulation mesh is rather coarse; however, since the 2D Rising Sun geometry does not have small features such as straps, with the aid of the Dey-Mittra algorithm, this mesh size is deemed acceptable. The timestep size was set to 1.0417 ps; this value was chosen since the π-mode of the device is known to be around 960 MHz, and a timestep size of 1.0417 ps would allow easier extraction of data that are in increments based on one RF period. This timestep is also compliant with the CFL condition.

Because of the nature of the 2D geometry, power extraction in this model was performed with a loaded cavity (shaded areas in Figure 0-1 and Figure 0-2). The loaded cavity acts as a field sink, and diagnostics were set up to record the RF power absorbed by this cavity. The 2D nature of the simulation restricts the use of wave launching ports, so the way for setting up the DC voltage is relatively limited. The DC voltage in this case was set up by using a dynamic feedback current source placed before the ampere updater within every timestep. This current source holds the DC voltage between the anode and the cathode at a predefined level by taking in voltage readings from history and then compares the measured voltage to the predefined voltage goal; the result of this comparison is used to adjust levels of the current source, which is then updated to the electric field after being passed through the field updaters.

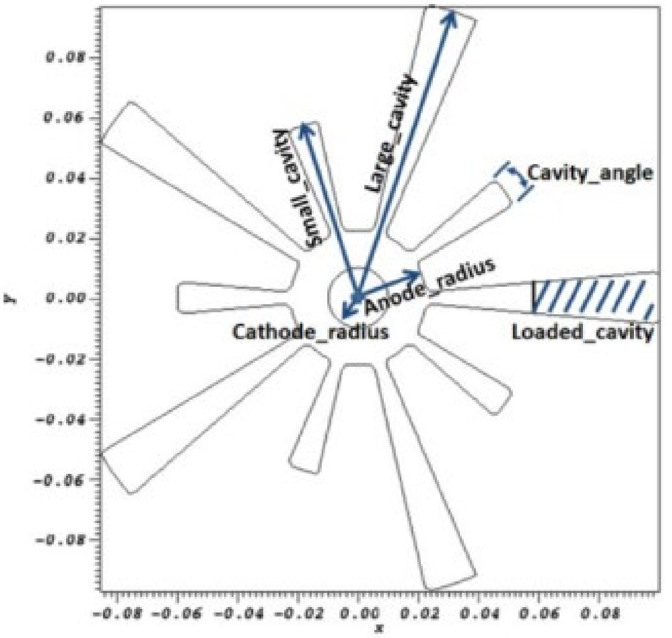

Figure VII-1 Rising Sun magnetron with a cylindrical cathode [52].

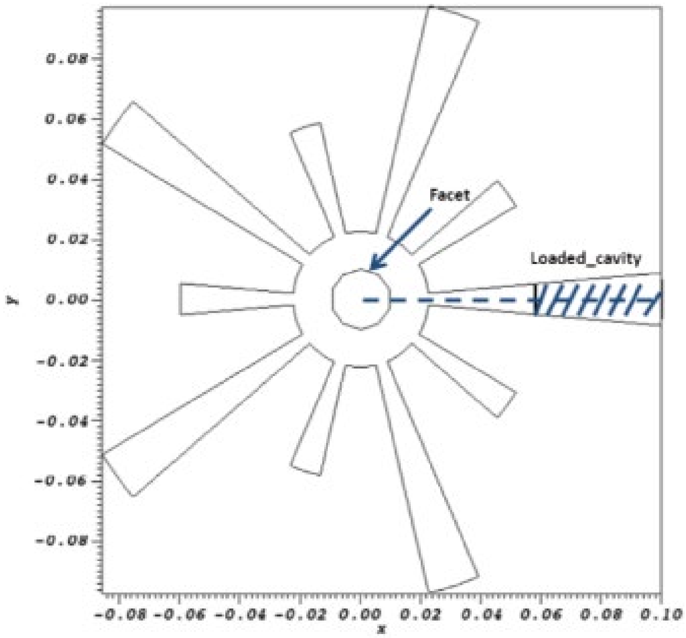

Figure VII-2 Rising Sun magnetron with a 10-sided faceted cathode [52].

Table VII-1 Rising Sun magnetron dimensions [52].

Cathode Radius (cm)	Anode Radius (cm)	Facet Width (cm)	Small Cavity Outer Radius (cm)	Large Cavity Outer Radius (cm)	Cavity Angle (degrees)
1.0	2.24	0.618	6.0	10.0	10

Current injection is based on a simple user defined current density; VSim reads the user's input and then automatically calculates the number of particles to be emitted based on the dimensions of the cathode to achieve the desired current density. All emitted particles have a zero mean velocity and a thermal velocity of 1.5×10^5 m/s. Both the anode geometry and the cathode geometry are setup as particle sinks. Back-bombarding electrons are absorbed by the cathode, and back-bombardment current is recorded by the simulation as "cathode current". The simulation model does not take account the effect of secondary electron emission.

7.2 Frequency Response Simulation

Before simulating the startup of the device, simulations were conducted to find out if the frequency response of the cavity was consistent with expectation. The π-mode is expected to be around 960 MHz. To simulate the frequency response of the magnetron cavity, a short (~20 ns) distributive current pulse containing multiple frequencies was defined inside of one of the magnetron resonators. This current induces fields that contain multiple frequencies, and the cavity will only resonate with frequencies that match the cavity resonance, and frequencies that do not match will be suppressed. Then the frequency response of the cavity can be identified by extracting the frequency components of the resonate cavity voltage after steady-state has been reached. No particles or additional electric or magnetic fields other than those induced by the current pulse were used. The simulation cavity frequency response of the Rising Sun magnetron is shown in Figure 0-3. For the desired π-mode at 960 MHz, the phase velocity is about 2.7×10^7 m/s.

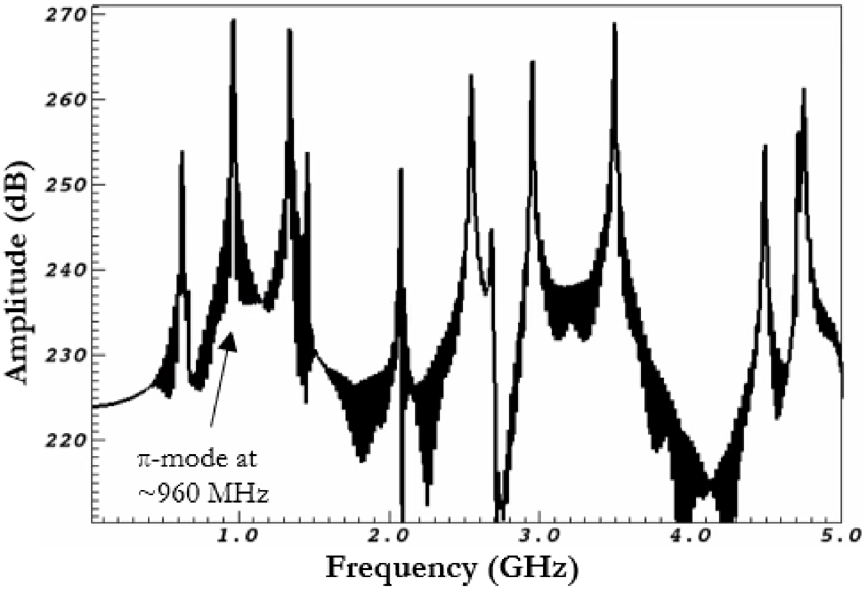

Figure VII-3 Frequency response of the Rising Sun magnetron from 0 to 5 GHz.

Usually, the π-mode is at the lowest resonant frequency; however, the Rising Sun magnetron has two sets of resonant cavities as it is unstrapped. As the result, the desired π-mode is at the second to the lowest resonant frequency. The lowest resonant frequency, at about 650 MHz, is significant as will be seen in results presented later in this chapter.

7.3 Reference Case: No Priming

In the first case, the 2D Rising Sun magnetron was simulated without priming to establish a reference case. The Rising Sun model is capable of reaching oscillation without priming. The model was simulated at 26 kV, 1200 G, and the emission current was set to 1000 A/m. Figure 0-4 shows the electron distribution at various times during the simulation. Since the device has ten vanes, the π-mode is expected to have a five-spoke pattern. While the electron distribution eventually converged to a five-spoke pattern (Figure 0-4.d), it went through a period of time when the electron distribution showed a three-spoke pattern, which corresponds to the 3π/5-mode (Figure 0-4.b).

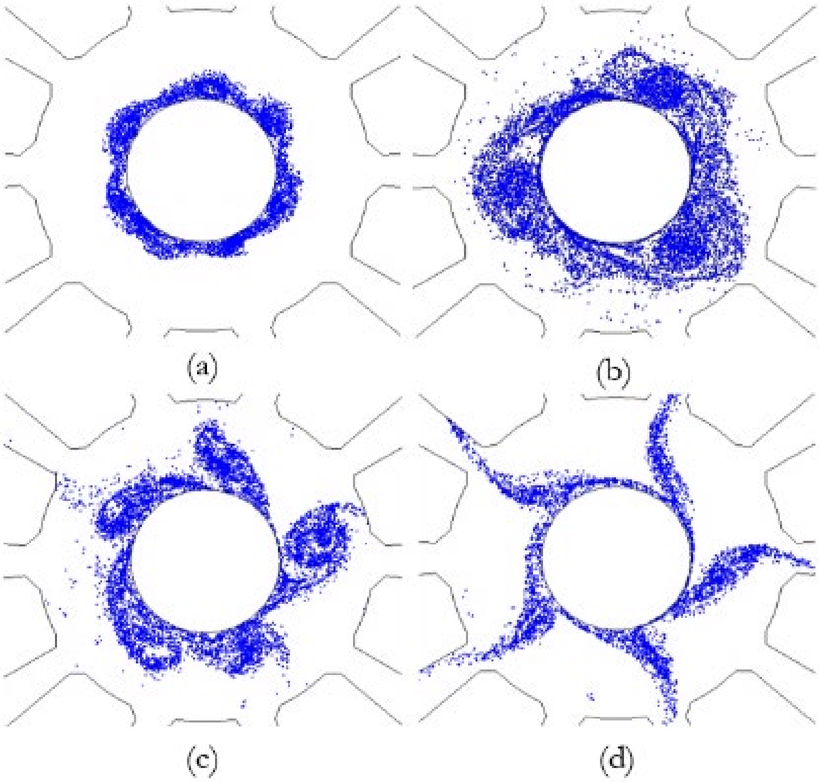

Figure VII-4 Simulated electron distribution of the Rising Sun magnetron without priming. a) 10 ns; b) 100 ns; c) 150 ns; d) 250 ns. Blue dots are electron maroparticles.

Figure 0-5 shows the simulated cavity voltage, anode and cathode currents, particle counts, and RF power vs time. Cavity voltage oscillation began shortly after 100 ns and grew to its full strength at around 300 ns. The current analysis plot shows most emitted electrons back-bombarded the cathode at the beginning of the simulation, before 100 ns. Then this back-bombardment current decreased when electrons began to reach the anode after 100 ns. Note that the anode current plot first shows a “spiky” pattern

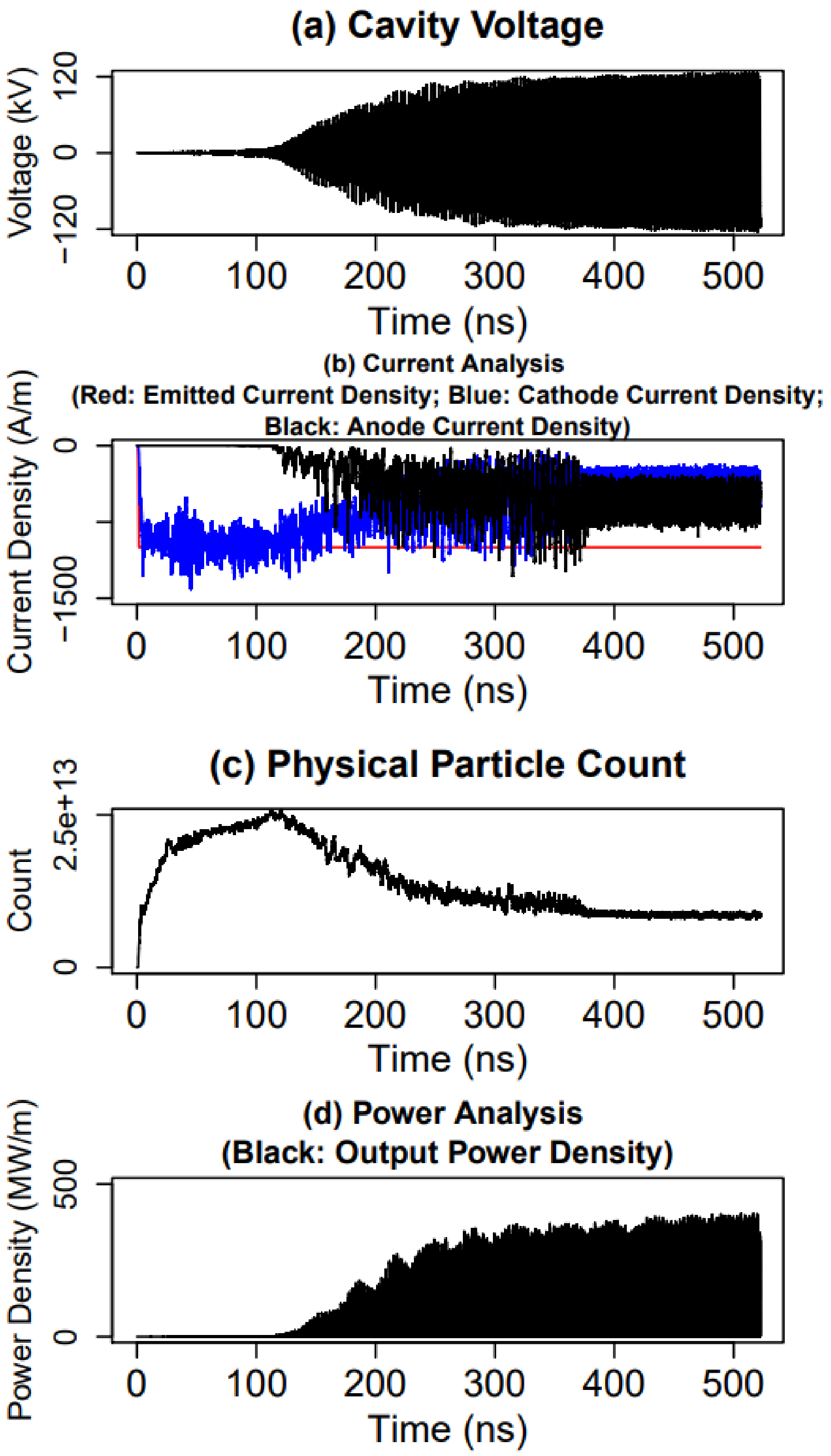

Figure VII-5 Simulation results for the Rising Sun magnetron simulation without priming showing (a) cavity voltage; (b) emission, anode, and cathode currents densities; (c) number of simulated macroparticles; (d) RF power density.

between 100 ns and 350 ns, indicating some kind of instability, and then shows a much cleaner pattern after 350 ns, which indicates the instability had been overcame. The particle count plot shows an initial build up until some critical number was reached, about 25 trillion electrons in this case; then the count began to decrease. The timing when the particle count began decreasing coincides with the timing of when the anode begins absorbing current. The particle count appears to begin stabilizing at a relatively constant level after 350 ns, which is the same time as when the anode current begins to stabilize. The output power plot shows a steady growth of RF power that is directly proportional to the amplitude of the cavity voltage. Figure 0-6 shows the FFT of the cavity voltage plot (Figure 0-5.a); besides the prominent π-mode at 960 MHz, there is the 3π/5-mode at 625 MHz that is about 30 dB less compared to the π-mode.

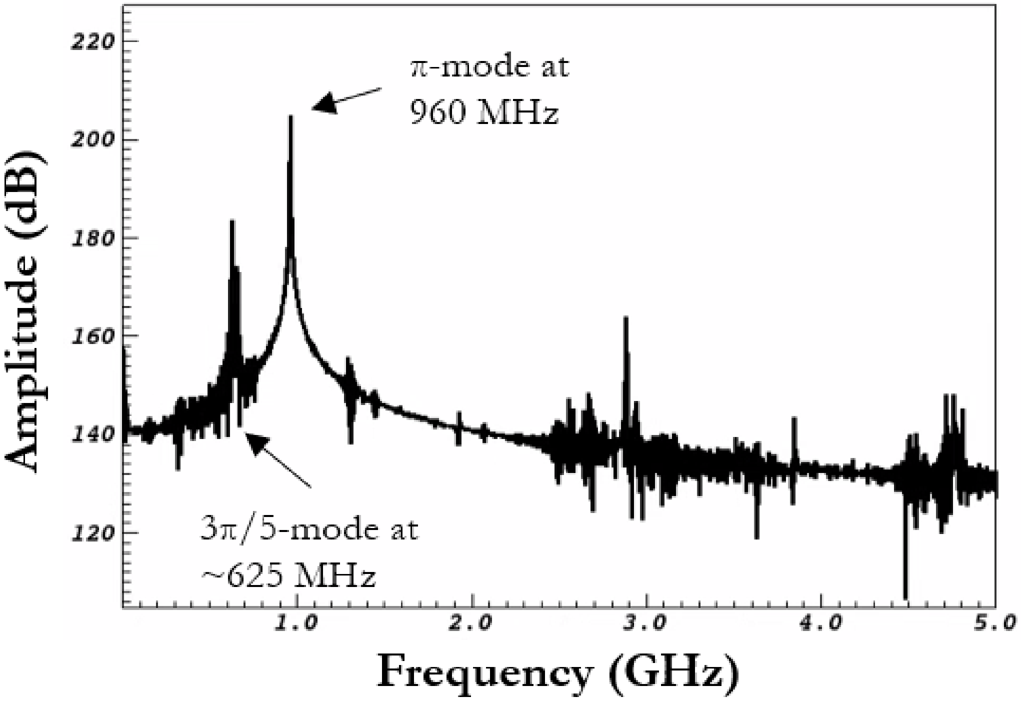

Figure VII-6 FFT of the simulated cavity voltage for the Rising Sun magnetron simulation without priming.

Figure 0-7 shows the electron population plots for the Rising Sun magnetron simulation without priming. All plots are divided at the same time locations into four regions for discussion. In all simulations of the Rising Sun magnetron, electron data was dumped once per 1000 timesteps. Since the timesteps size, 1.0417 ps, is exactly one thousandth of the RF period, the electron data dumps are exactly at the end of every RF period (1.0417 ns).

The radial position plot confirms that electrons reached the anode shortly after 100 ns (Figure 0-7.a, region 2), and then there was continuous electron transfer from the cathode to the anode. Note that even after the oscillation entered steady state after 350 ns (Figure 0-7.a, region 4), and the average electron position (Figure 0-7.a, red line) stayed close to the cathode. The radial velocity plot shows the radial velocity was compressed around zero just before 200 ns (Figure 0-7.b, regions 1&2) and the average line (Figure 0-7.b, red line) stayed flat at zero, which means the bulk of the electron population was not migrating toward the anode. The radial velocity behavior dramatically changed after 200 ns (Figure 0-7.b, region 3); the overall velocity distribution shows a greatly increased variance while the average radial velocity moves further and further into the positive ranges until a steady state is reached at 350 ns (Figure 0-7.b, region 4). The average line in region 4 becomes very stable and flat.

Since the data dumps are right at the end of each RF period in this case, ideal oscillation in the π-mode should result in five perfectly horizontal lines for the azimuthal position plot. At the beginning of the simulation, before 100 ns (Figure 0-7.c, region 1), the azimuthal position plot shows a lack of pattern, indicating a random particle distribution evenly around the cathode. A clear five-spoke π-mode pattern begins to emerge after 100 ns, but the five high intensity regions are not horizontal, indicating the frequency in this region is not 960 MHz (Figure 0-7.c, region 2). The five high intensity regions stayed relatively horizontal after 200 ns (Figure 0-7.c, region 3); however, the plot shows a lot of noise, which hints at frequency instability that is likely caused by mode competition. The azimuthal position plot stabilizes after 350 ns (Figure 0-7.c, region 4), showing a clean horizontal five-spoke π-mode pattern and indicating a stable oscillation frequency. It is worth noting that although the electron distribution plot

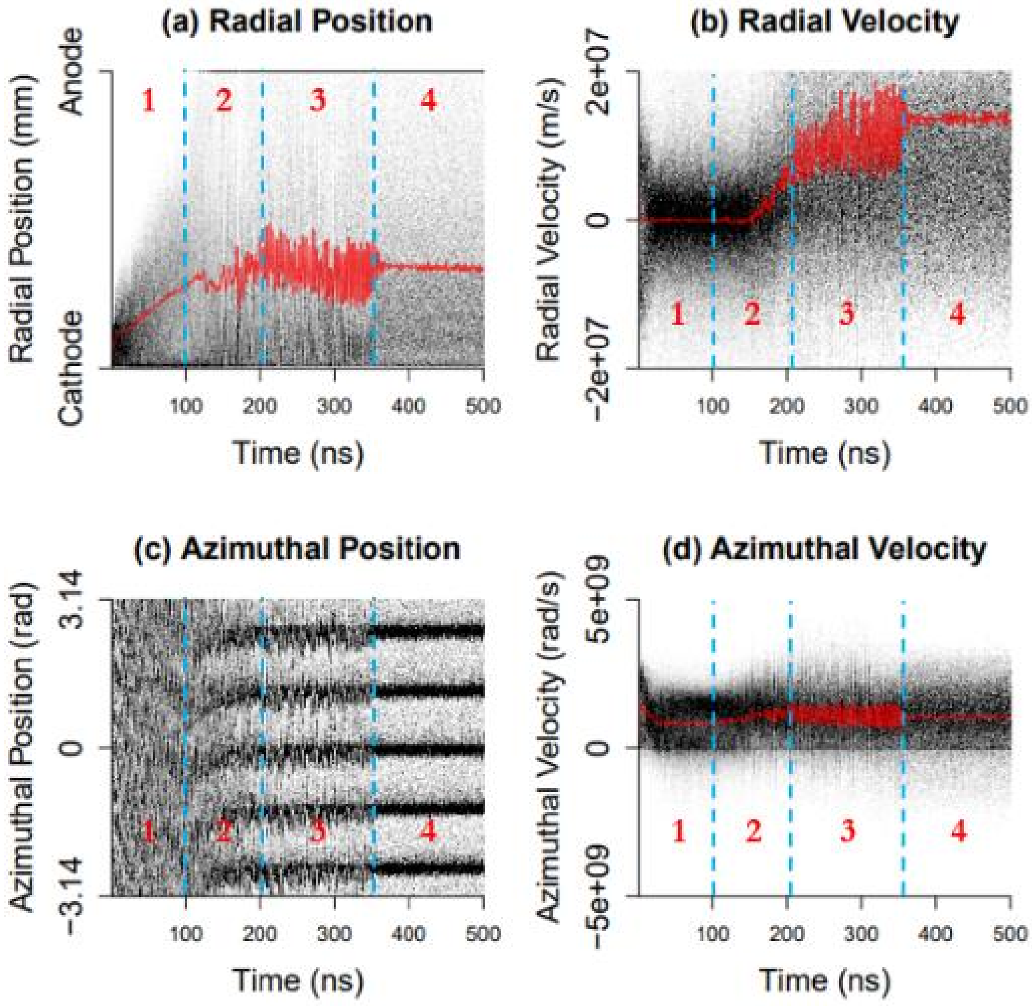

Figure VII-7 Electron population plots for the Rising Sun magnetron simulation without priming showing (a) radial position; (b) radial velocity; (c) azimuthal position; (d) azimuthal velocity. In subplots (a), (b), and (d), red lines indicate average. Darker color denotes higher probability.

(Figure 0-4.b) showed a three-spoke 3π/5-mode pattern, such mode never shows up in the azimuthal position plot (Figure 0-7.c, region 2).

The azimuthal velocity plot (Figure 0-7.d) shows a “dip” towards the zero line in regions 1 and 2, before electrons began to migrate toward the anode, which suggests the electron population is highly cycloidal since a significant number of electrons are moving slowly in the azimuthal direction at the bottom of their cycloidal trajectories. The plot pattern is, again, noisy in region 3 like the other 3 plots, and the average azimuthal velocity value appears to be oscillating (Figure 0-7.d, region 3, red line), which again indicates mode competition. The plot pattern and the average value both stabilized in region 4 like the other plots. Note that there appears to be particles with negative azimuthal velocities, which means their motion in the azimuthal direction was counter to the direction of spoke rotation, throughout the simulation. This means the electron cycloidal flow never collapsed to full Brillouin flow throughout this simulation. The meaning of this plot will be discussed in more detail later.

Figure 0-8 shows the plots of breadth ratios; the regions are divided at the same time locations as in Figure 0-7. The breadth ratio in radius initially stayed around 1:1 (Figure 0-7.a, region 1), which indicates no net electron migration towards the anode since the total number of outward-moving electrons (advancers) is about the same as the total number of inward-moving electrons (decliners), resulting in nearly zero net movement in the radial direction. In region 2, the breadth ratio begins to increase, indicating an increasing percentage of electrons begin to move toward the anode. This pattern continues in region 3; however, the pattern becomes noisy due to mode competition. Finally, in region 4, the breadth ratio in radius stabilizes around 3.8:1

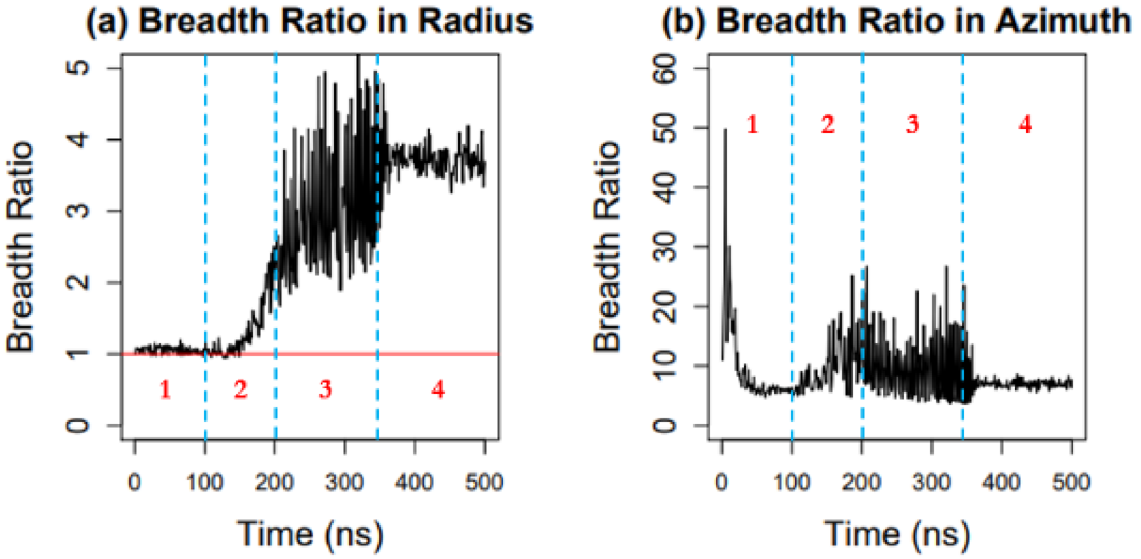

Figure VII-8 Breadth ratios for the Rising Sun magnetron simulation without priming. (a) Breadth ratio in the radial direction; (b) breadth ratio in the azimuthal direction.

positive demonstrating that more electrons are moving toward the anode than toward the cathode as would be expected. This now constant value is the result of a balance between electrons being injected to the cathode and electrons leaving the system by collecting on the anode.

The breadth ratio in azimuth had an initial surge in the positive direction to as high as 50:1 positive (Figure 0-8.b, region 1); however, the ratio quickly collapsed down to under 10:1 positive, which suggests the electron population gets dramatically more cycloidal compared to when the simulation first starts. The ratio has another move in the positive direction during region 2; however, after some noisy pattern in region 3, the ratio stabilizes at around 8:1 positive when steady state is reached in region 4. This result once again confirms the previous observation that the electron cycloidal flow never collapsed to full Brillouin flow (in which case the breadth ratio in azimuth should approach infinity). However, this effect is likely the result of newly injected electrons entering the population as these electrons will be highly cycloidal in trajectory when they first enter the interaction space. The azimuthal breadth ratio during stable oscillation could well be related to the newly injected electrons compared to those electrons moving toward the anode for collection as part of the oscillation process.

7.4 RF Priming

In this case, a very small RF signal (less than 1% of the device's full oscillation power density) was excited between the resonant cavities to induce the π-mode. This signal is active only during the first 50 ns of the simulation. The model was simulated at identical parameters as the no priming case. The simulation results for this case are very similar to that of the no priming case, but steady state oscillation is reached much quicker (100 ns with RF priming vs. 350 ns without). Figure 0-9 shows the electron distribution at various times during the simulation. Compared to the no priming case, the five-spoke π-mode pattern formed much sooner due to the effect of the RF priming, and the electron distribution did not undergo a period with a three-spoke pattern.

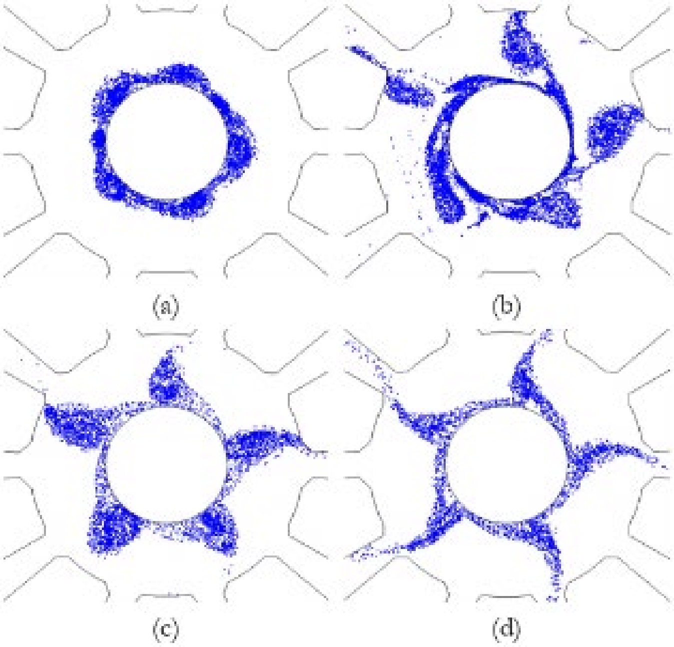

Figure VII-9Simulated electron distribution of the Rising Sun magnetron with RF priming. a) 10 ns; b) 25 ns; c) 50 ns; d) 100 ns.

Figure 0-10 shows patterns of cavity voltage and current densities very similar to that of Figure 0-5. The cavity voltage plot (Figure 0-10.a) shows the oscillation voltage grew to near maximum at about 50 ns. The current plots (Figure 0-10.b) show electrons began reaching the anode as early as around 30 ns, and a period of instability was again observed before steady state was reached at about 100 ns. The particle count plot (Figure 0-10.c) confirms that the simulation reached steady state at 100 ns. The output power plot (Figure 0-10.d) shows near maximum output was reached at around 60-70 ns, which is much faster compared to the no prime case (about 350 ns, Figure 0-5.d). Figure 0-11 shows the FFT of the cavity voltage plot (Figure 0-10.a), which shows the same pattern as Figure 0-6. The π-mode at 960 MHz is prominent and the 3π/5-mode at 625 MHz is about 30 dB less compared to the π-mode.

Figure 0-12 shows the electron population plots for the Rising Sun magnetron simulation with RF priming; all plots are divided at the same time locations into three regions for discussion. The radial position plot shows the electron population migrated towards the anode as soon as the simulation started (Figure 0-12.a, region 1); then the plot shows an instability period (Figure 0-12.a, region 2) before steady state is reached (Figure 0-12.a, region 3). The radial velocity plot shows the radial velocity compression around zero (Figure 0-12.b, region 1), though very briefly, before oscillation begins. This is same as the no priming case (Figure 0-7.b, regions 1 and 2). Then there is an instability period before steady state (Figure 0-12.b, regions 2 and 3). The azimuthal position plot (Figure 0-12.c) and the azimuthal velocities plot (Figure 0-12.d) show the same process as the radial plots (Figure 0-12.a and b). Two points worth mentioning are that the azimuthal position plot indicates sustained stable

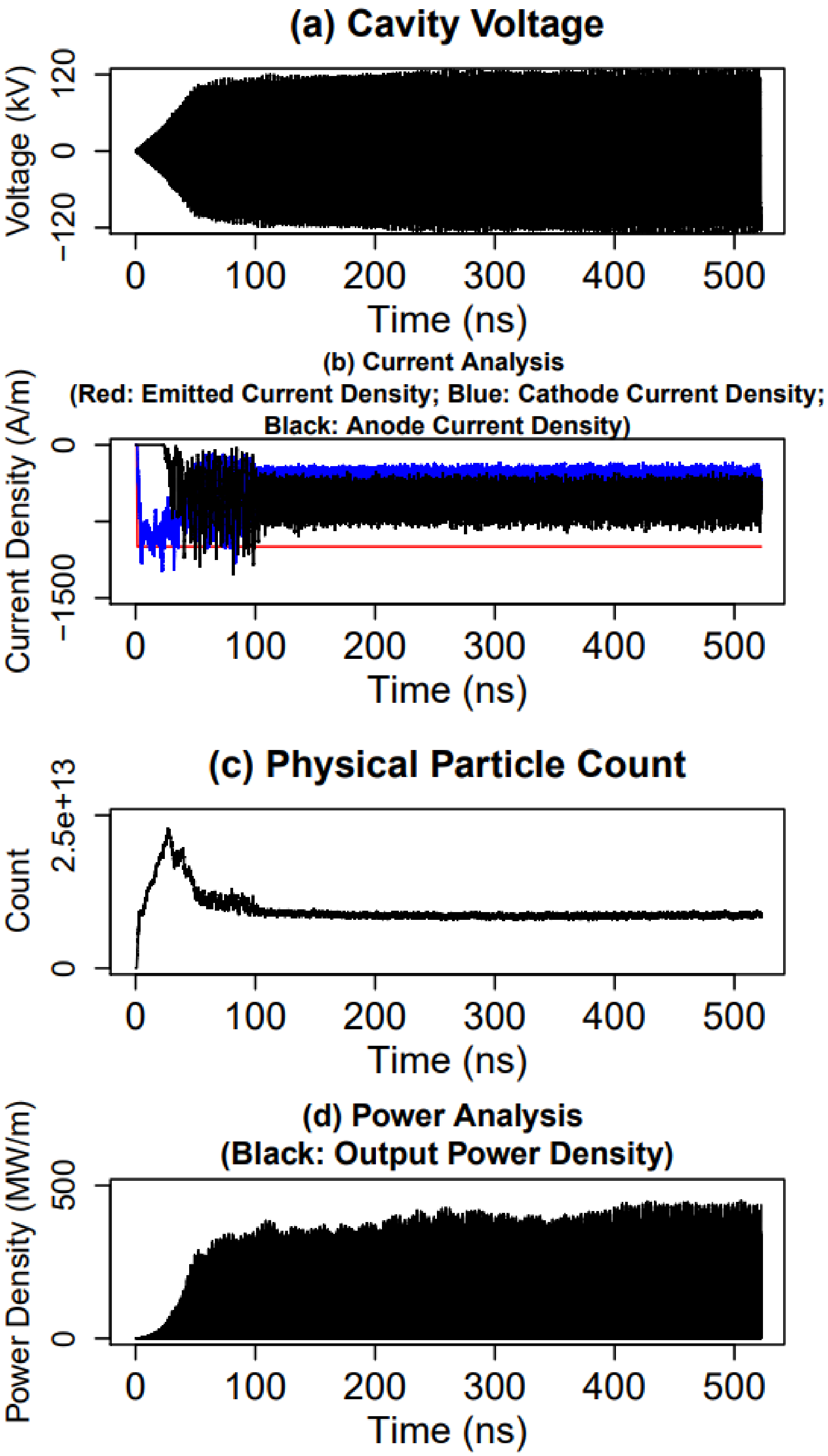

(a) Cavity Voltage

(b) Current Analysis (Red: Emitted Current Density; Blue: Cathode Current Density; Black: Anode Current Density)

(c) Physical Particle Count

(d) Power Analysis (Black: Output Power Density)

Figure VII-10 Simulation results for the Rising Sun magnetron simulation with RF priming showing (a) cavity voltage; (b) emission, anode, and cathode currents densities; (c) number of simulated macroparticles; (d) RF power density.

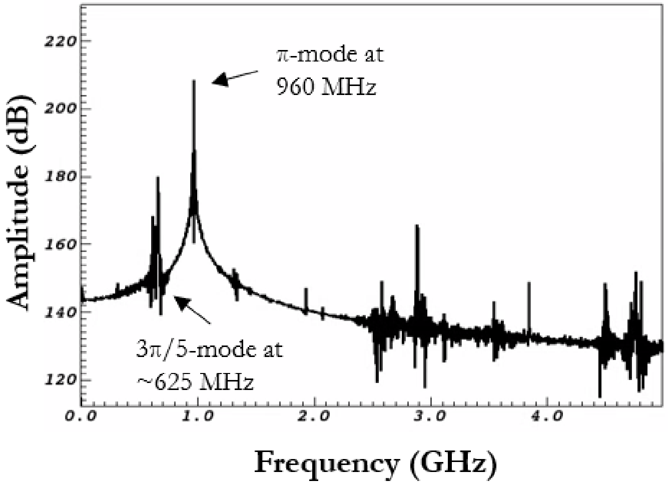

Figure VII-11 FFT of the simulated cavity voltage for the Rising Sun magnetron simulation with RF priming.

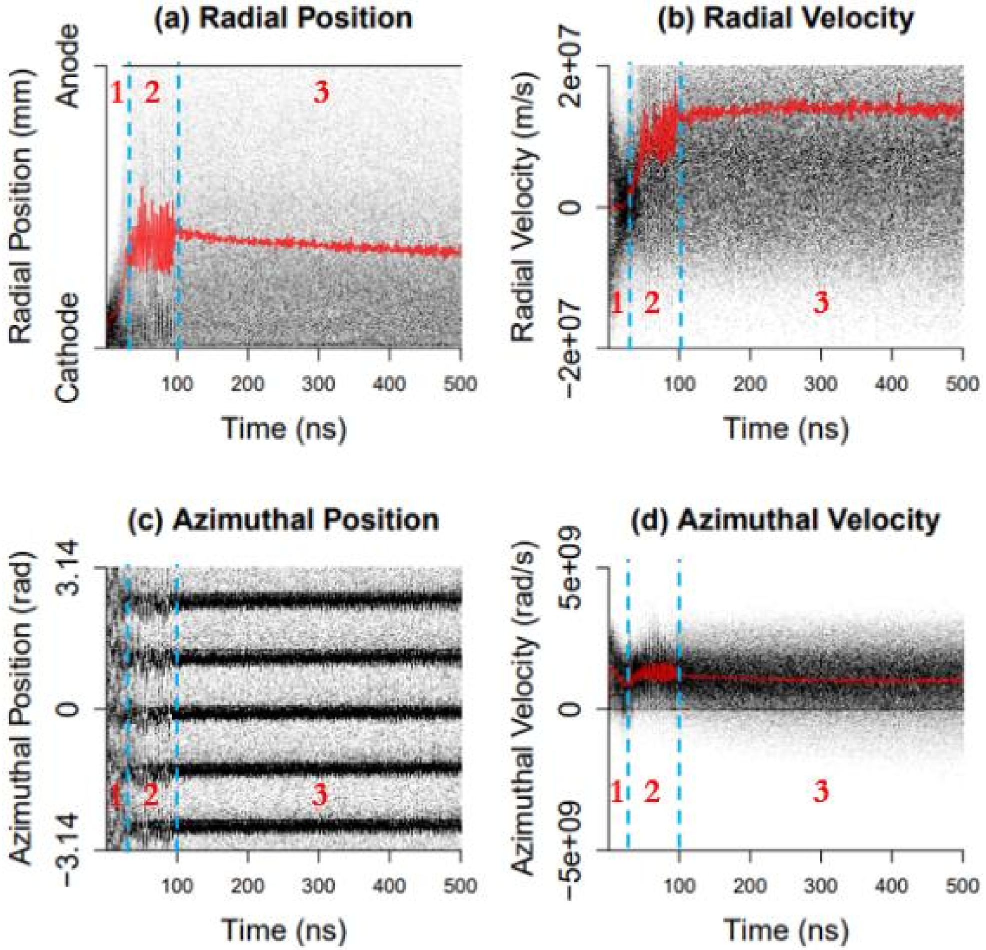

Figure VII-12 Electron population plots for the Rising Sun magnetron simulation with RF priming showing (a) radial position; (b) radial velocity; (c) azimuthal position; (d) azimuthal velocity. In subplots (a), (b), and (d), red lines indicate average. Darker color denotes higher probability.

oscillation after steady state was reached (Figure 0-12.c, region 3), and the azimuthal velocity plot shows the azimuthal velocity dips toward zero right before oscillation begins to ramp up (Figure 0-12.d, end of region 1). Again, this transition in azimuthal velocity before oscillation is also observed in the no priming case.

The breadth ratio plots (Figure 0-13) mostly agree with the observations made in the previous plots. The breadth ratio in radius (Figure 0-13.a) begins to increase in the positive direction as soon as the simulation starts, unlike that of the no priming case (Figure 0-7.a) where the ratio stayed around 1 for a period of time before increasing into the positives. On the other hand, despite the fact that steady state was reached more quickly in the RF primed case compared to the no priming case, the breadth ratio in radius in both cases stabilized at 3.8:1 positive when the simulations are in steady state implying this value is fixed during stable oscillation and could be viewed as an indicator of stable oscillation. The breadth ratio in azimuth in this RF primed case

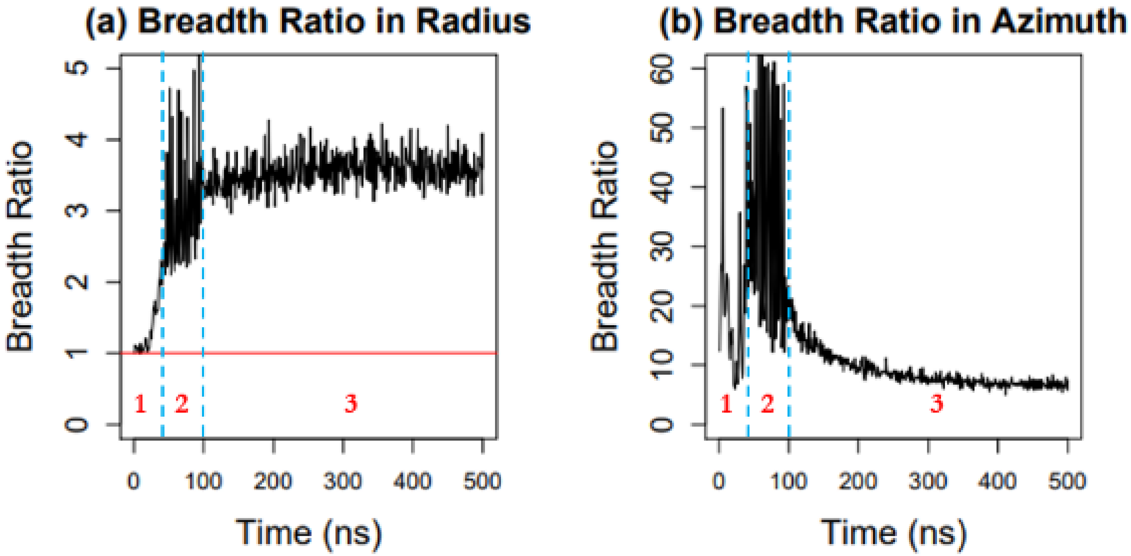

Figure VII-13: Breadth ratios for the Rising Sun magnetron simulation with RF priming. (a) Breadth ratio in the radial direction; (b) breadth ratio in the azimuthal direction.

(Figure 0-13.b) shows a much higher value (50-60) during the instability period (region 2) compared to that of the no priming case (Figure 0-7.a, region 2); nonetheless, the breadth ration in azimuth again converges to about the same value as with no priming, 8:1 positive, after steady state is reached. Again, this value is likely skewed lower since, in steady state oscillation, the electron population is constantly being replenished by newly injected electrons, which are cycloidal.

7.5 Cathode Modulation

In this cathode modulation case, electrons were injected at five discrete, evenly spaced locations and these injection locations rotate to match the RF phase. This case was simulated at the parameters used in the previous research (22.2 kV, 900 G) [15-17]; this work intends to apply new analysis techniques to previous results. The modulated electron injection frequency was set to 960 MHz, same as the previous research. Figure 0-14 shows the electron distribution at various time locations. Figure 0-14.a shows

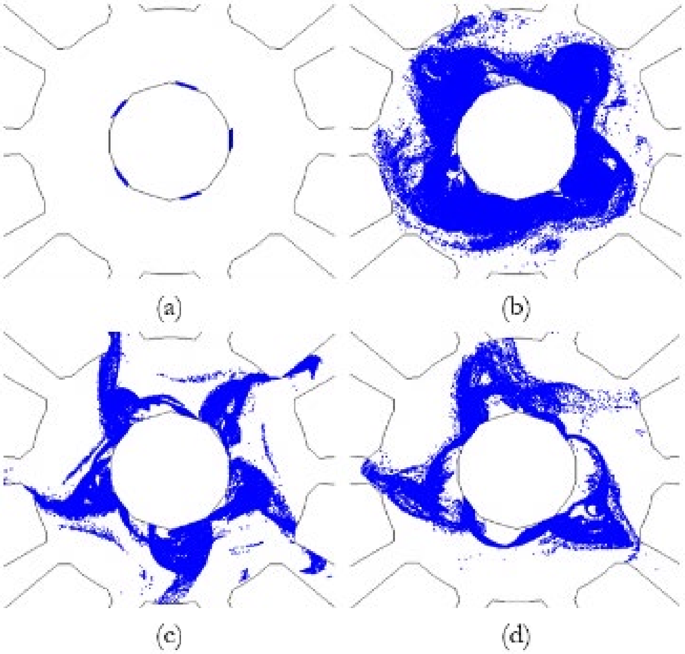

Figure VII-14 Simulated electron distribution of the Rising Sun magnetron with cathode modulation. a) 1 ns; b) 50 ns; c) 100 ns; d) 450 ns.

the very beginning of the simulation when the five discrete injection locations are clearly visible. At 50 ns (Figure 0-14.b), the electron distribution shows a four-spoke pattern; this is surprising since the modulated injection is intended in priming the five-spoke π-mode. At 100 ns (Figure 0-14.c), the magnetron was already oscillating in π-mode. In fact, this oscillation started as early as 80 ns (as it will be shown in later plots); this oscillation timing is consistent with results from the previous research. However, the π-mode oscillation did not sustain and the electron distribution ends up showing a three-spoke 3π/5-mode pattern near the end of the simulation (Figure 0-14.d).

Both the cavity voltage plot and the output power plot Figure 0-15.a and d show very unstable patterns. Note that the output power from the previous two cases (Figure 0-5.d and Figure 0-10.d) show the output power level increased to about 400 MW/m shortly after oscillation starts; however, in this case (Figure 0-15.d) the output power level after oscillation started at about 80 ns holds at a relatively low level (~200 MW/m) for more than 200 ns before increasing again. A couple observations can be made from the current plots. First, the emitted current (Figure 0-15.b, red line) appears to be decreasing before oscillation begins at 80 ns, indicating the electron injection is space charge limited due to the high electron concentration at the discrete injection locations. Second, the pattern of the cathode current plot (Figure 0-15.b, blue line) indicates intense electron back-bombardment from 200 ns to 350 ns; this is likely caused by the lack of electron injection in between the five injection locations, which leads to a lack of repulsive force from the cathode against electrons that are already in the interaction space. This phenomenon was observed in the previous research, and the solution was to have a small portion (5-10%) of the electrons be injected uniformly while keeping the

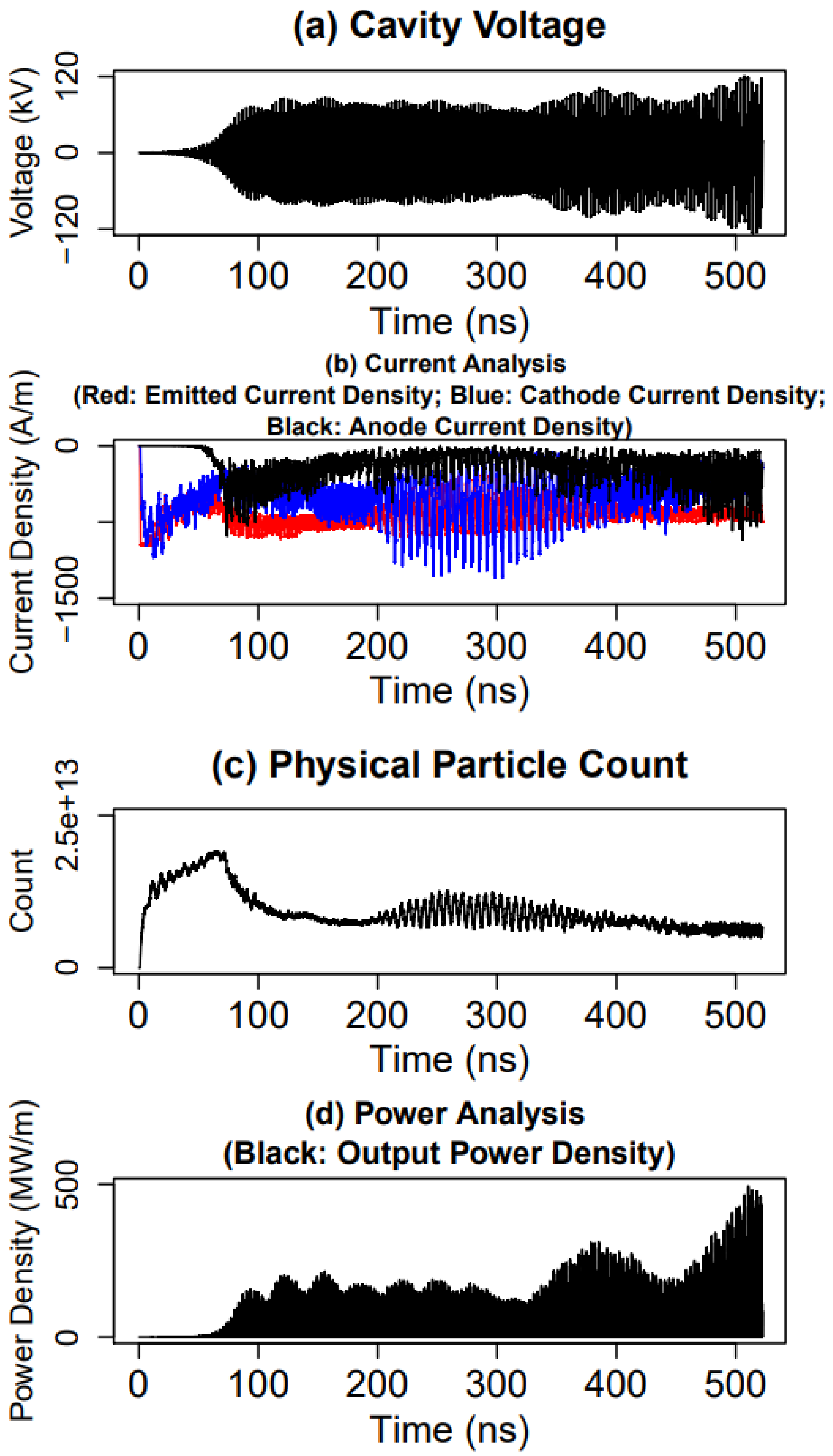

Figure VII-15 Simulation results for the Rising Sun magnetron simulation with cathode modulation showing (a) cavity voltage; (b) emission, anode, and cathode currents densities; (c) number of simulated macroparticles; (d) RF power density.

rest of the electrons in modulated injection. The particle count plot (Figure 0-15.c) shows that despite the various issues observed in the other plots, the total number of particles held at a relatively constant level after oscillation began. Figure 0-16 shows the FFT for the cavity voltage plot (Figure 0-15.a); although the π-mode at 960 MHz still has the highest amplitude, the 3π/5-mode at 625 MHz is much more prominent compared to the previous two cases. This observation is consistent with the fact that the magnetron oscillated with a three-spoke 3π/5-mode pattern near the end of the simulation (Figure 0-14.d).

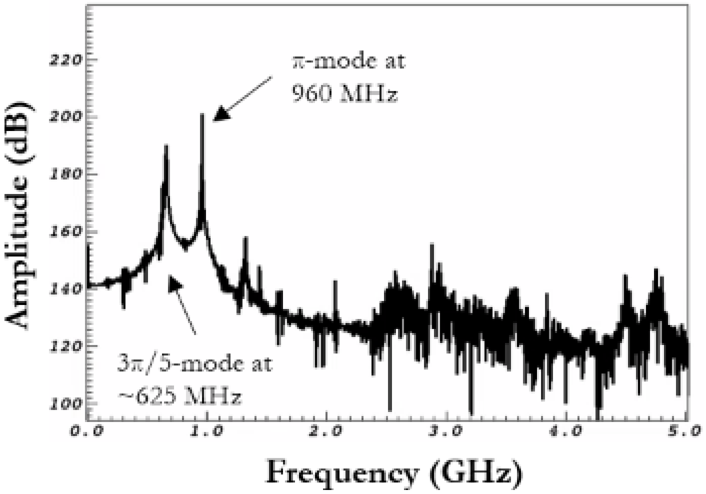

Figure VII-16 FFT of the simulated cavity voltage for the Rising Sun magnetron simulation with cathode modulation.

Figure 0-17 shows the electron population plots for the simulation with modulated electron injection. The radial position plot shows the electron population migrated toward the anode at the beginning of the simulation (Figure 0-17.a, region 1); however, for the reminder of the simulation, the radial position distribution shows a lot of instability (Figure 0-17.a, regions 2,3&4). The radial velocity plot (Figure 0-17.b) indicates the average radial velocity failed to fully break away from the zero line throughout the simulation. The azimuthal position plot shows that although the magnetron was in π-mode when oscillation begins, the oscillation frequency was not stable in reference to the expected 960 MHz frequency (Figure 0-17.c, region 2). And for the reminder of the simulation, the azimuthal velocity plot shows very chaotic patterns (Figure 0-17.c, regions 3&4), which suggests the oscillation never converged to a stable mode. The oscillation pattern in region 3 of the azimuthal velocity plot (Figure 0-17.d) suggests intense mode competition, which is likely a result of electron back- bombardment discussed previously. In region 4, though the average value of the

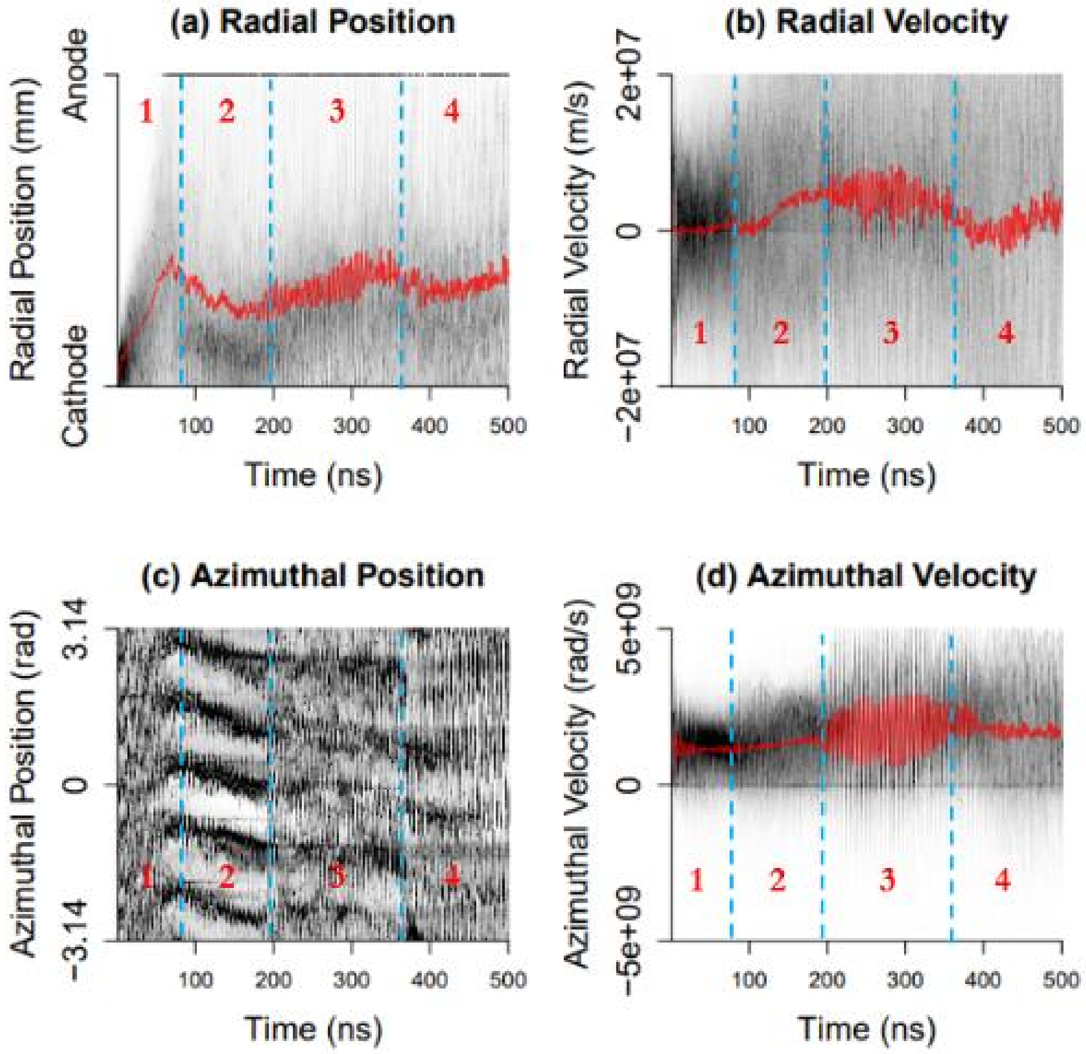

Figure VII-17 Electron population plots for the Rising Sun magnetron simulation without cathode modulation showing (a) radial position; (b) radial velocity; (c) azimuthal position; (d) azimuthal velocity. In subplots (a), (b), and (d), red lines indicate average. Darker color denotes higher probability.

azimuthal velocity appears to hold at a stable value, the overall distribution shows large variance, which is also a sign of instability.

The breadth ratio plots (Figure 0-18) confirm the observations made from previous plots. The breadth ratio in radius (Figure 0-18.a) struggles to break away from 1:1 and advance further into the positives; there was never sufficient internal support for charge transfer from the cathode to the anode throughout the simulation. Region 3 of the breadth ratio in azimuth plot (Figure 0-18.b) shows oscillation of the ratio between rather dramatic readings, from about 3:1 positive to over 60:1 positive, which again indicates instability. Hence, in these simulations the results do not reproduce the prior simulation results.

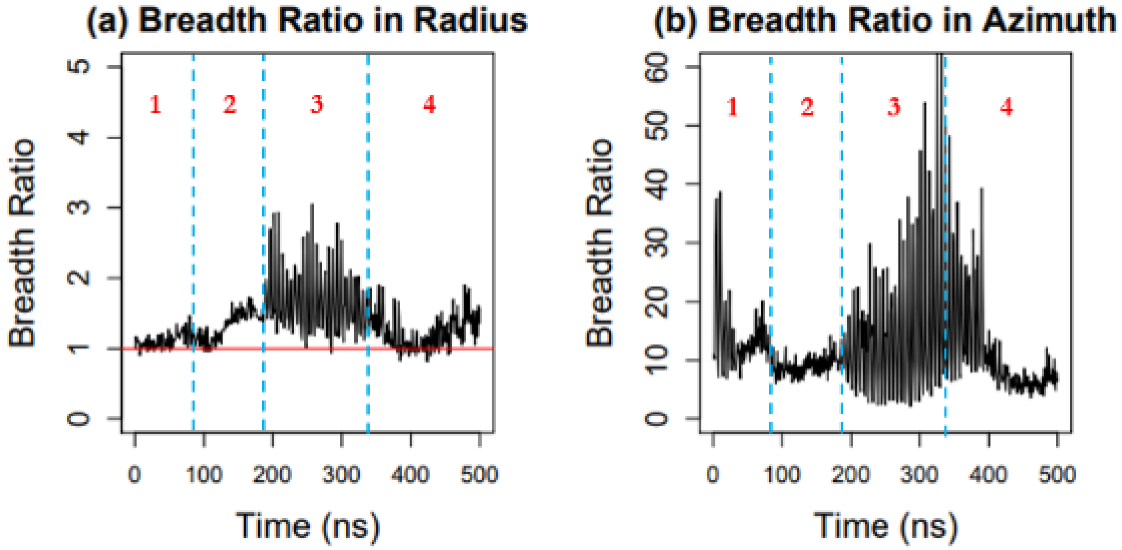

Figure VII-18 Breadth ratios for the Rising Sun magnetron simulation with cathode modulation. (a) Breadth ratio in the radial direction; (b) breadth ratio in the azimuthal direction.

7.6 Summary and Analysis

In the simulations of the 2D Rising Sun magnetron model, the model was able to reach oscillation in all three priming cases. The simulation with no priming and the simulation with RF priming reached oscillation following a highly similar process. First, there was an initial buildup period in which the electron population built up around the cathode and the outer edge of the electron population slowly expanded away from the cathode. For the simulation with no priming, this step took about 100 ns to complete (Figure 0-7, region 1); for the RF priming case, this step occurred extremely fast, within 30 ns, due to the priming (Figure 0-12, region 1). Oscillation began when the out edge of the electron population reached the anode and the charge begin to transfer from the cathode to the anode. However, in both the no priming case and the RF priming, there were periods of instability when oscillation first began (Figure 0-7 region 3 and Figure 0-12 region 2). These instabilities periods were likely due to mode competition. After the instabilities settle, the simulations were able to reach steady state. When the simulations were in steady state, the breadth ratios in radius stabilized at about 3.8:1 positive, which indicate sustained internal support for charge transfer from the cathode to the anode.

In both cases, increased electron cycloidal motions were observed during the period leading up to oscillation. These observations are characterized by the probability distributions of their azimuthal velocities dipping toward the zero line prior to oscillation, accompanied by the breadth ratios in azimuth also dipping down. This “dipping” of the azimuthal velocity distributions and breadth ratios are illustrated in Figure 0-19. In these cases, the dip appears to be a precursor to the start of oscillation. As the physical manifestation of the velocity dip is that electrons are at low azimuthal velocity (maximum potential energy) and near the cathode in their cycloidal orbit, this may affect the behavior of the electron population as will be discussed in Chapter Nine. After the dip, the velocities and breadth ratios increase and become very unstable in time. The higher breadth ratio indicates a more Brillouin like flow and the higher average velocity is moving toward the electron spoke rotation velocity needed for oscillation. Hence, the dip represents a time frame where the electrons appear to gather at lower azimuthal velocity with greater cycloidal motion before or nearly simultaneously with greater movement towards the anode (breadth ratio in radius).

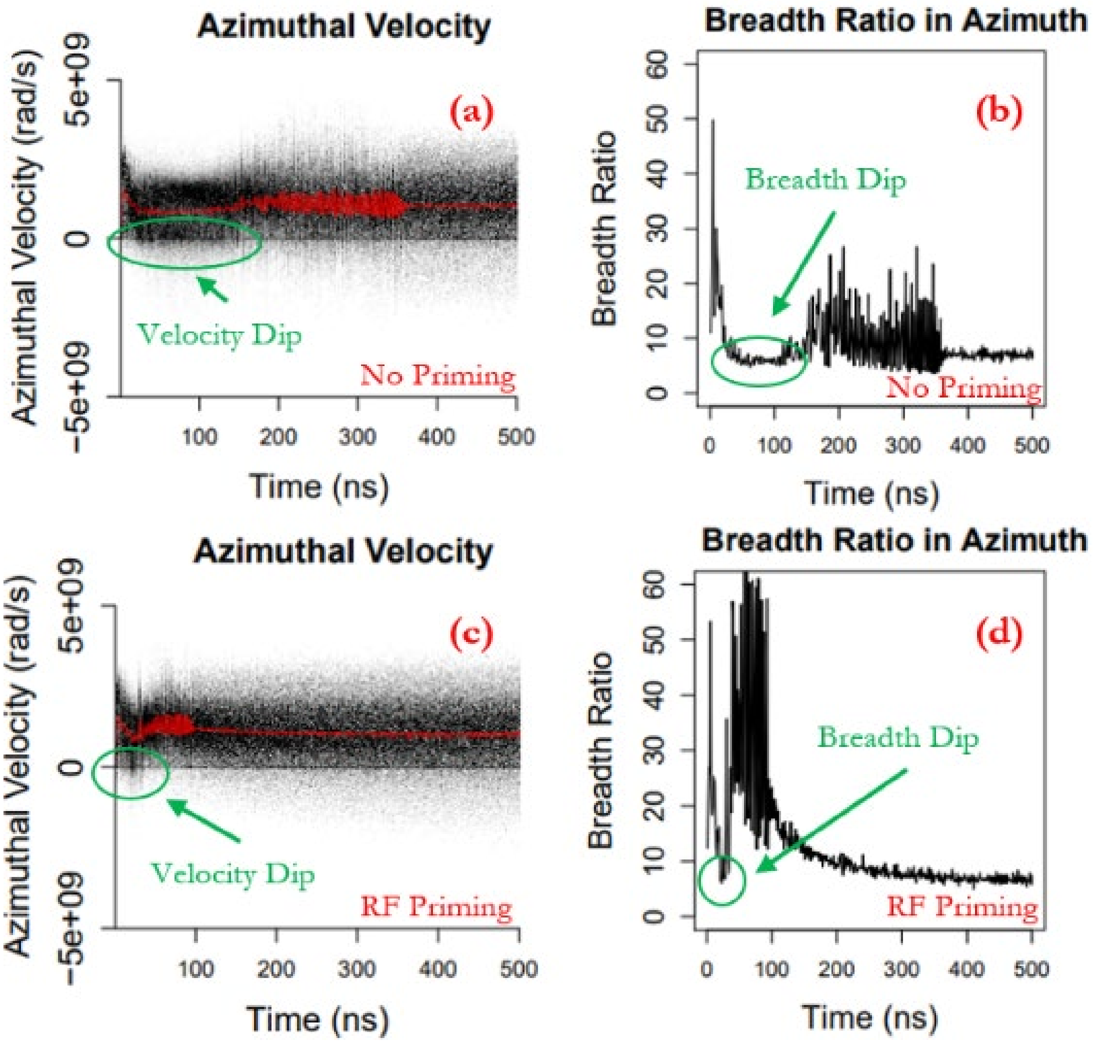

Figure VII-19 Illustrations showing the azimuthal velocities and the breadth ratios dip prior to oscillation began. (a) azimuthal velocity distribution for the no priming case; (b)breadth ratio in azimuth for the no priming case; (c) azimuthal velocity distribution for the RF priming case; (d) breadth ratio in azimuth for the RF priming case.

The simulation case with cathode modulation yielded very different results in comparison. The biggest difference being that, in this case, steady state oscillation was not reached at the end of the 500 ns simulation and that the oscillation mode seems to be converging to the 3π/5-mode near the end of the simulation instead of the π-mode. The breadth ratio in radius for this case struggled to break away from 1:1, indicating a lack of internal support for charge transfer from the cathode to the anode. The current setups (V and B) for this simulation case are not optimal and will be studied and adjusted in the future.

In all three simulation cases, the breadth ratios in azimuth seem to gravitate toward the 8:1 positive level. As new electron must be injected into the system to main steady state current transfer to the anode, it is, of course, expected that a steady state breadth ratio value must also occur. The reason that the results stabilize at this exact value is currently unclear and requires further investigation. As discussed previously, this 8:1 positive ratio is relatively low, which indicates the electron population is not in full Brillouin flow. Note that the Brillion flow theory was developed for a single-particle system and does not consider the effects of newly injected electrons. Even with a relatively low 8:1 positive breadth ratio in the azimuth, some of the electrons in the system could well be in near-Brillouin flow states. However, since the current breadth ratio analysis accounts for every electron in the system, the ratios are affected by electrons that are newly injected, which tend to have very different behavior compared electrons that have stayed in the system for longer. In planned future research, breadth ratio analyses will be performed in different radial regions so that the electron population close to the cathode is analyzed separately from the electron population farther from the cathode. This separation should mitigate the skewing effect of newly injected electrons on the analysis results.

CHAPTER EIGHT: SIMULATION OF THE L3HARRIS CWM-75KW[1]

8.1 Simulation Setup for the L3Harris CWM-75kW

The detailed 3D geometry of the L3Harris CWM-75kW was constructed with CAD based on measurements provided by L3Harris Technologies (as seen in Figure 0-1). The scale of the simulated geometry and the physical geometry of the CWM-75kW is 1:1, resulting in a size of 110 mm by 110 mm by 127 mm for the simulation domain, which was then uniformly subdivided into rectangular cells. The cell size was determined based on the smallest geometry in the domain, which was the 3.9 mm gap between the circuit straps.

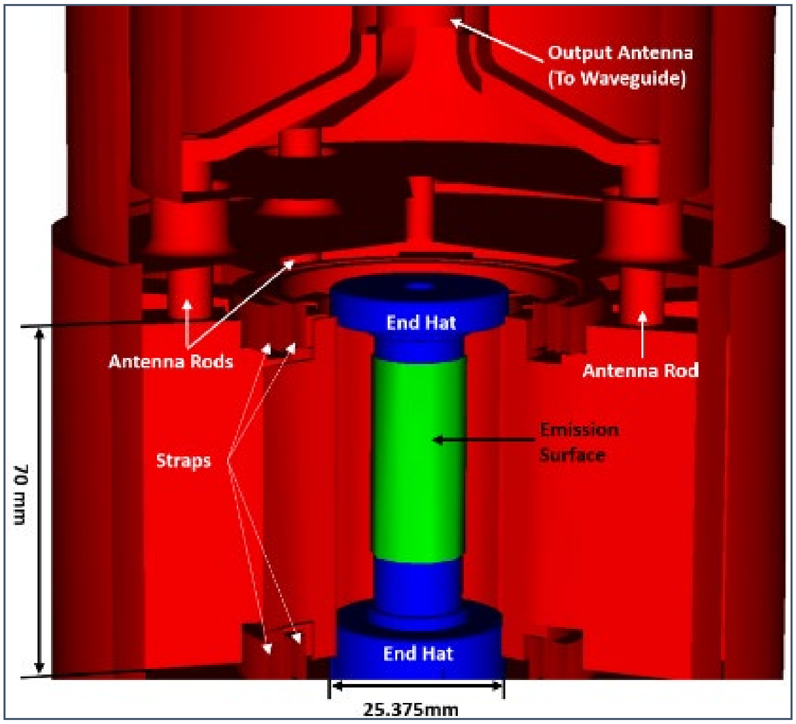

Figure VIII-1 Geometric model of the CWM-75kW used in simulations.

---

[1] Parts of this chapter have been published by Andong Yue, et. al. in Journal of Vacuum Science & Technology B 39, 022201 (2021); https://doi.org/10.1116/6.0000809

These constraints result in a cell size of 0.5 mm by 0.5 mm by 1 mm. This rather coarse simulation grid was used to keep the computational time as short as possible, while adequately resolving the strap geometry. The time step size is 0.5 ps, which is compliant with the CFL condition, and the macroparticle size is about 10^6. In the original assembly, the output antenna is embedded inside of an output waveguide, which was not included in the simulation to reduce the size of the simulation domain for shorter computational time. The loading effect of the output waveguide onto the cavity was mimicked by adjusting the setting for the upper-z simulation boundary in VSim. A 300 ns simulation takes roughly two days to compute when 16 cores of computational power are used.

A constant external magnetic field was defined over the entire simulation domain in the -z direction. The DC voltage between the anode and the cathode was achieved by defining a constant, 1-cell-thick, electric field between the anode geometry and the cathode geometry at the lower-z boundary. The upper-z boundary was defined as an open boundary to represent a perfectly matched output waveguide. Particles were emitted from the emission surface with a Richardson-Dushman emission profile:

$$J = M \times \left(\frac{4\pi m e}{h^3}\right) \times T^2 \exp\left(-\frac{W}{T}\right), \qquad \text{Eq. 0-1}$$

where J is the resulting magnitude of the current density (A/m^2), M is the multiplier, m is the electron mass (kg), e is the electron charge, h is Planck's constant, T is the temperature (K), and W is given by:

$$W = W_0 - \left(\frac{e}{4\pi\epsilon_0}\right) \times |\boldsymbol{E}f|, \qquad \text{Eq. 0-2}$$

where E is the surface electric field (V/m), f is the enhancement factor, and W_0 is the work function (eV) [45]. For the simulation results to be presented, a work function (W_0)

of 4.5 was selected, and the multiplier M was iteratively tuned to achieve the 4.75 A of emission current from the cathode to match the device operating parameters.

As will be shown, the magnetron model will not oscillate in a reasonable simulation time (<1,000 ns) without some form of priming to start the oscillations. This is not unexpected, as this magnetron typically begins oscillation in milliseconds, although it should be noted that others have shown this magnetron can start oscillation within 1,000 ns in simulation under space charge limited conditions [45-46]. Several types of priming have been studied over the years, including RF priming, cathode modulation priming, and magnetic field priming to initiate oscillation within PIC simulations [15-17, 39, 54, 75-76]. Some simulations, such as the Rising Sun magnetron, can oscillate without priming [15-17, 45-46].

It is important to note that, in the simulation of the CWM-75kW magnetron, the combination of the 0.5 ps timestep and the 1,000 timestep dump period does not result in data being dumped at the end of each RF period like in the Rising Sun magnetron simulation presented in the previous chapter. For this reason, the azimuthal position plots are not expected to show a five-line horizontal pattern even when the simulated device is oscillating in the π-mode with stable phase; the patterns in the azimuthal position plots are expected to be more random compared to the azimuthal position plot patterns presented in the previous chapter.

8.2 Frequency Response Simulation

As before, simulations were conducted to find out if the frequency response of the cavity was consistent with the expectation. The load-free resonant frequency of the π-mode should be around 908 MHz. The simulated frequency response of the cavity is shown in

Figure 0-2. The π-mode is at the lowest resonance frequency, which is 908 MHz according to the simulation result shown. Unlike the Rising Sun magnetron, all resonant cavities of the CWM-75kW are identical and the magnetron is strapped. The simulated π-mode frequency matched the known device π-mode frequency, which indicates that the simulated cavity geometry is correct. For this desired π-mode at 908 MHz, the phase velocity is approximately 1.63×10^7 m/s.

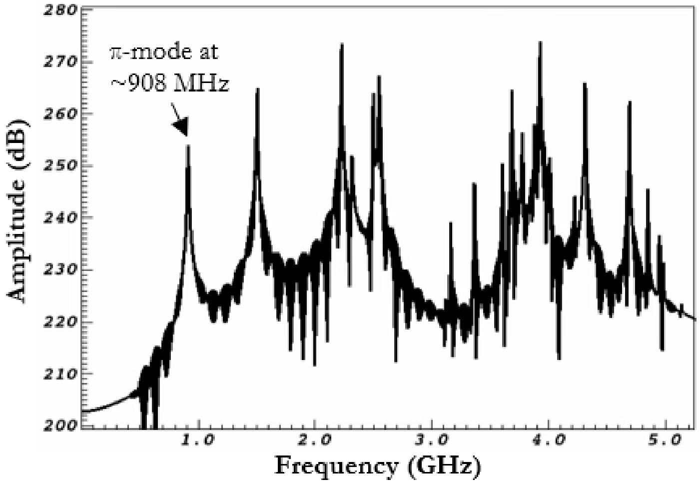

Figure VIII-2 **Frequency response of the L3Harris CWM-75kW from 0 to 5 GHz.**

8.3 Reference Case: No Priming

Before applying priming techniques to the simulations, the model was simulated without priming to establish a baseline. The simulation was run for the typical operating parameters shown in Table 0-1. The cavity RF voltage is extremely low (~20 V). Figure 0-3 shows the 2D cross-sectional electron distribution plot at the center plane of the cavity at the end of the simulation time; it shows a ring-shaped electron hub near the cathode. There is little to no interaction between electrons and the anode, which indicates an absence of oscillation. Figure 0-4 shows the typical result of the RF voltage in the resonant cavities over time; no meaningful oscillation can be observed before the simulation ended at 1,000 ns.

Figure 0-5 shows the FFT of the simulation cavity voltage; it appears that many frequencies, including the 0 Hz DC frequency, have been excited and no dominant mode can be identified. This result is consistent with the expectation that some kind of priming technique is required to start the device in a reasonable amount of simulation time.

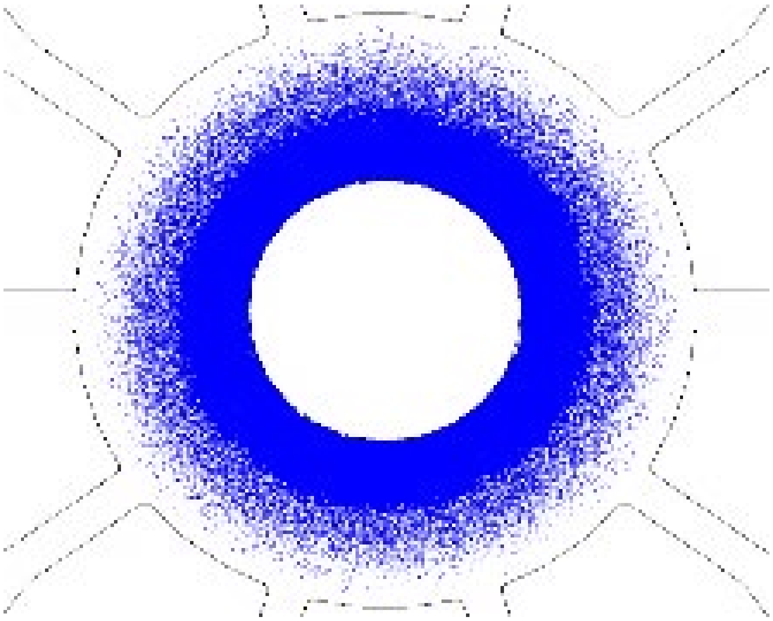

Figure VIII-3 2D cross-sectional electron distribution plot from VSim at the center plane of the cavity at the end of the simulation with no priming. Blue dots represent electron macro-particles.

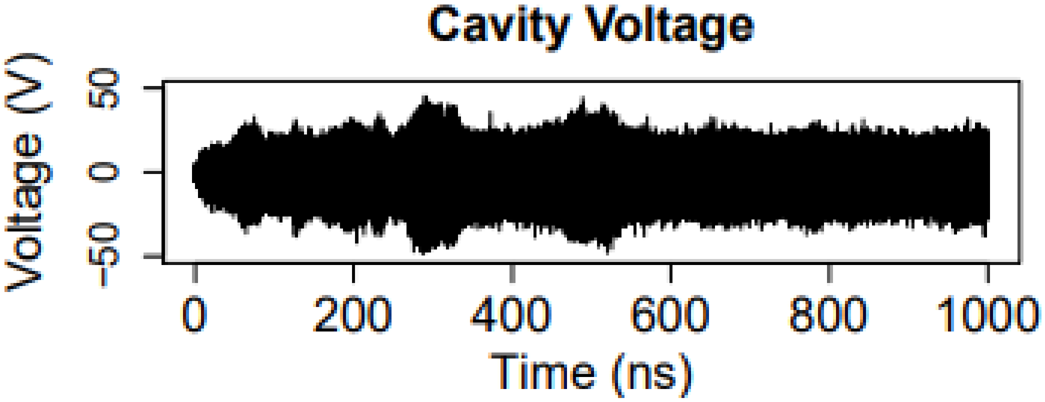

Figure VIII-4 Voltage in the resonant cavities over time with no priming in VSim; note that the amplitude of the voltage oscillation is minimal.

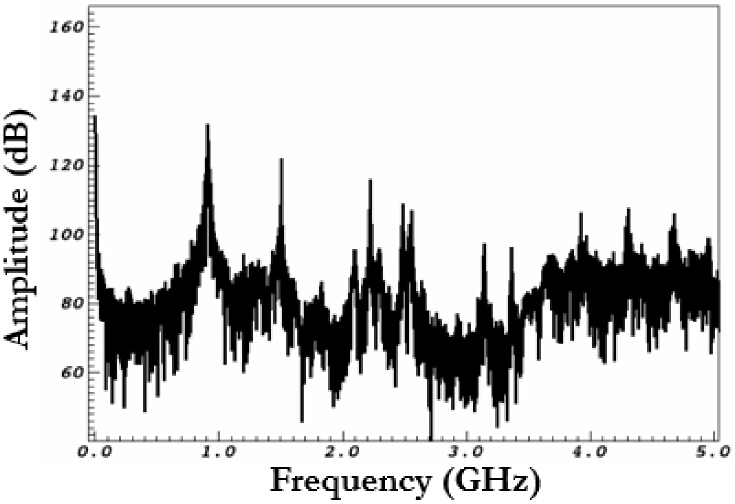

Figure VIII-5 FFT of the simulated cavity voltage for the CWM-75kW magnetron simulation without priming.

Figure 0-6 shows the electron population distribution when there is no priming. The plots are divided into 2 regions for discussion. In this case, the radial position plot showed that the electrons initially appear to move away from the cathode (Figure 0-6.a, region 1); however, the process quickly reversed, and the bulk of the electrons collapsed back to the cathode (Figure 0-6.a, region 2);. The radial velocity plots showed a similar result; when the simulation first started, the velocity distribution diverged from the centerline, which is zero, indicating an abundance of movement in the radial direction (Figure 0-6.b, region 1); however, the velocity distribution quickly collapsed back to the zero-line, which suggests the initial activity has faded (Figure 0-6.b, region 2). In the azimuthal direction, both plots show a lack of activity (Figure 0-6.c and d, region 2). The pattern at the azimuthal position suggested that, after the initial activity fades, there were hardly any orderly electron movements in the azimuthal direction. The azimuthal velocity plot shows that the azimuthal velocities were random and spread out, which indicates a lack of bunching. Note that the dig in azimuthal velocity seen in the 2D Rising Sun simulations are not observed here.

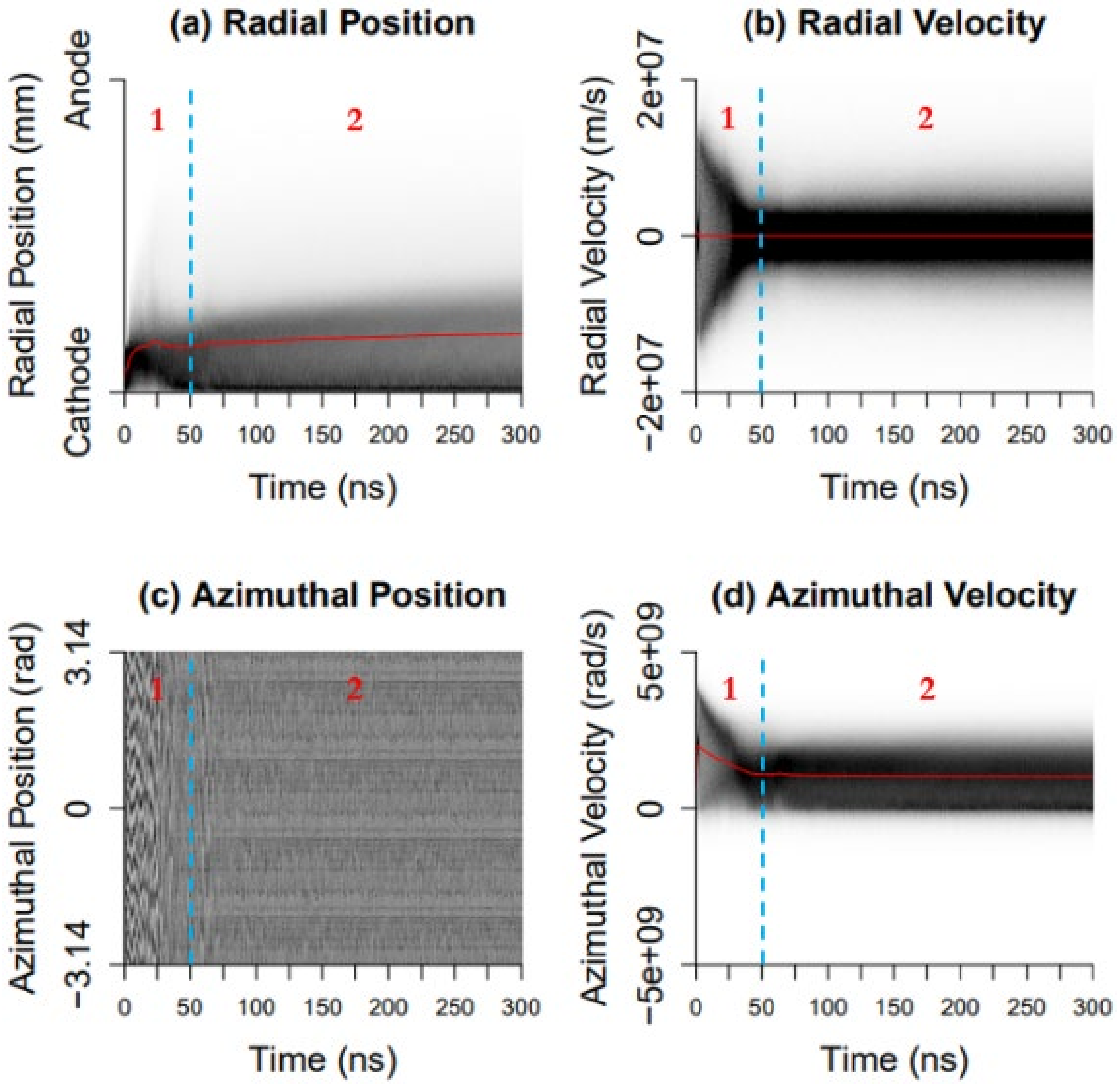

Figure VIII-6 Electron population plots for the CWM-75kW magnetron simulation without priming showing (a) radial position; (b) radial velocity; (c) azimuthal position; (d) azimuthal velocity. In subplots (a), (b), and (d), red lines indicate average. Darker color denotes higher probability.

Figure 0-7 shows the breadth ratios. The breadth ratio in radius (Figure 0-7.a) was at 1:1 for the entire duration of the simulation; indicating no net electron movement in the radial direction. The breadth ratio in azimuth (Figure 0-7.b) converged to about 15:1 positive after have some slightly more positive levels at the beginning of the simulation. Again, unlike the 2D simulations, no dip in the breadth ratio in azimuth (Figure 0-7.b) is observed.

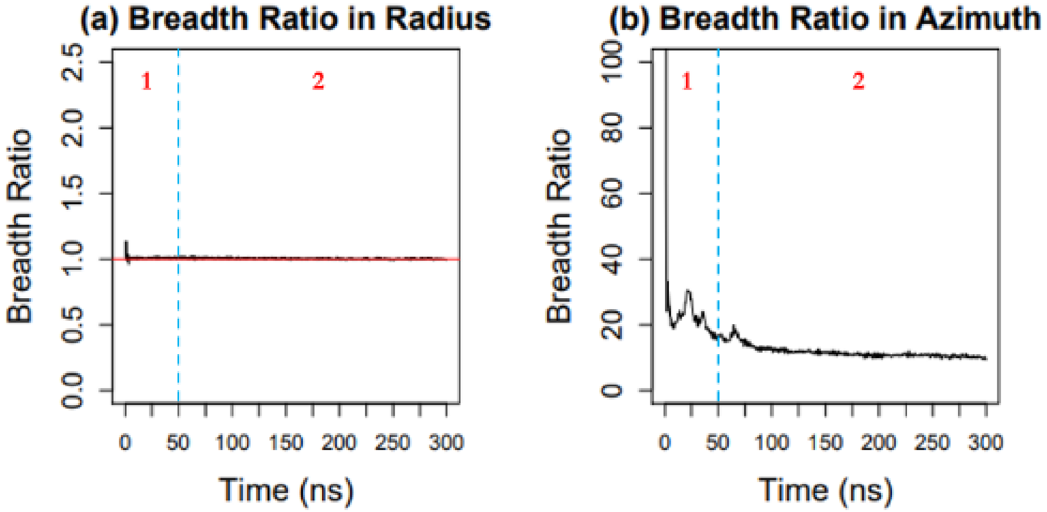

Figure VIII-7 Breadth ratios for the CWM-75kW magnetron simulation without priming. (a) Breadth ratio in the radial direction; (b) breadth ratio in the azimuthal direction.

8.4 Magnetron Startup with RF Priming

For this simulation, a current was defined in the resonator cavities in a way that induces the π-mode at 908 MHz. The input power of this priming was tuned to 40 kW, about half of the operating power of the magnetron. This driving current was turned on at the beginning of the simulation and was shut off after 50 ns, and then the magnetron was allowed to free run. Figure 0-8 shows the cross-sectional electron distribution at various time instances. At the beginning of the simulation, Figure 0-8.a, electrons are being emitted uniformly from the cathode, and the π-mode RF priming is active; Figure 0-8.b shows the electron distribution pattern when the RF priming current shuts down (50 ns). The RF priming current creates an electric field that pulls electrons away from the cathode and forms a five-spoke π-mode pattern. This pattern gradually collapses after the RF priming current is turned off at 50 ns, as Figure 0-8.c shows that the spokes are not well-defined at 100 ns. At this point, it looks as if the device is not going to oscillate, but then the five-spoke π-mode pattern reemerges at about 140 ns, and Figure 0-8.d shows the device begins to oscillate to full power at 150 ns.

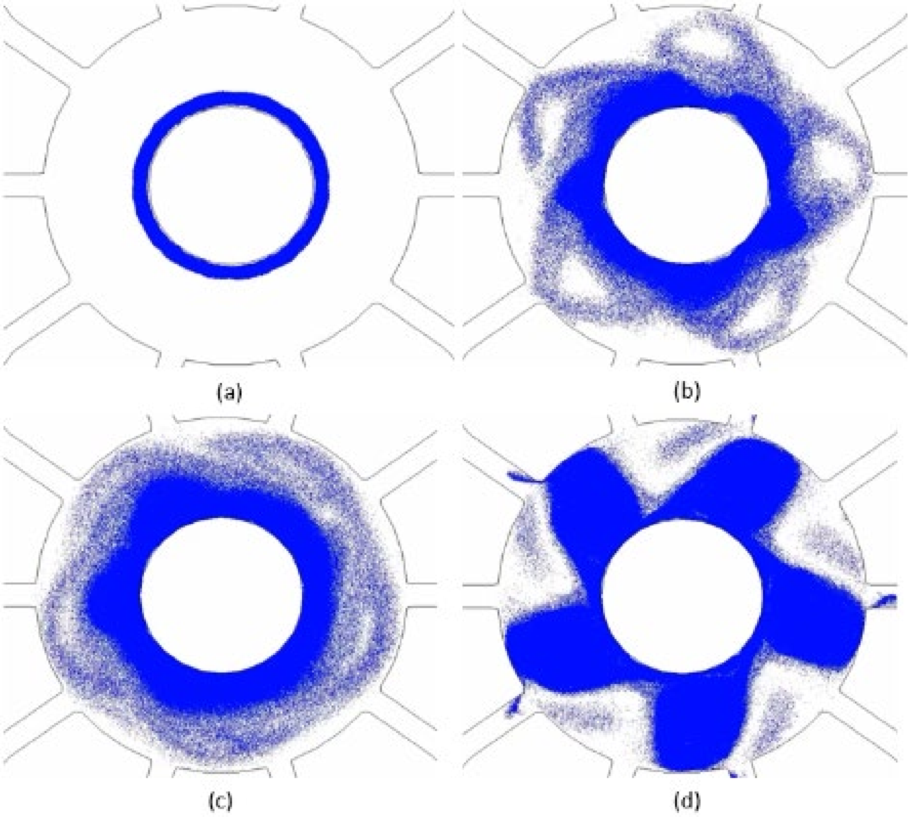

Figure VIII-8 Cross-sectional electron distribution with RF priming. a) 0.5 ns; b) 50 ns; c) 100 ns; d) 150 ns.

Figure 0-9 shows the RF cavity voltage, anode and cathode currents, particle counts, and RF power vs time. After the RF priming current was turned off at 50 ns, both the cavity voltage and the power gradually decreased, with the cavity voltage decaying to as low as 25% of the peak cavity voltage during priming and the output power decaying to below 10% of the peak output power during priming. However, around the 150 ns mark, the device suddenly begins oscillation, and the output power is near the 75kW operating power of the device. The FFT of the cavity voltage, in Figure 0-10, confirms the simulated device was oscillating at 908 MHz. Although the RF priming current drove up the cavity voltage when it was active during the first 50 ns of the simulation, the anode current remained low. Additionally, when the device begins to oscillate at 150 ns, the anode current spikes to as high as 10 A, but the cathode current did not drop to near zero, indicating strong electron back-bombardment. Also, a rapid drop in particle count was observed. This indicates the existence of "super spokes," which occur when an unsustainably large number of electrons are absorbed by the anode in a short time window [15-17]. Then the oscillation broke down and does not reemerge for the remainder of the simulation.

Figure 0-11 shows the electron population distribution when there is RF priming during the first 50 ns of the simulation; these results are intriguing. Here the plots are divided into 4 regions. RF priming was active until 50 ns (Figure 0-11, region 1), during which time the radial position plot shows the RF priming pulling electrons toward the anode; the azimuthal position plot shows a striation pattern, which indicates electron bunching. This bunching is also confirmed by the convergence of azimuthal velocity. But the bunching did not appear to be sustained after the RF priming was shut off (Figure 0-11, region 2) based on the azimuthal position plot. However, the azimuthal velocity shows that the velocity convergence continued even after the RF priming was shut off. Oscillation then occurred at 150 ns (Figure 0-11, region 3) at which point the azimuthal velocity shows strong convergence, and the striation pattern can once again be seen in the azimuthal position plot; the radial position plot shows that electrons were being rapidly collected at the anode within a 10 ns window. Then the oscillation collapsed due to this rapid loss of electrons. This collapse is confirmed by the divergence

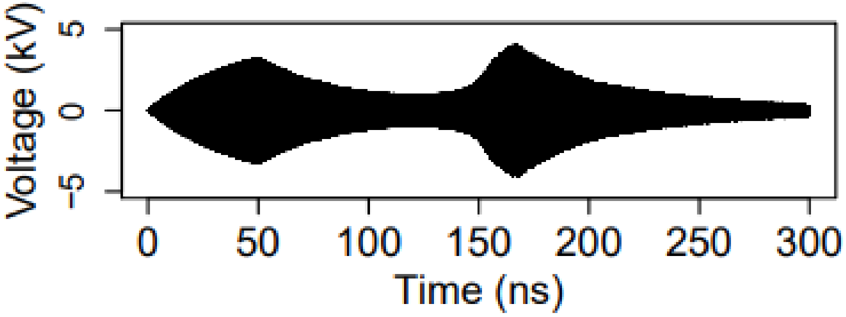

(a) Cavity Voltage

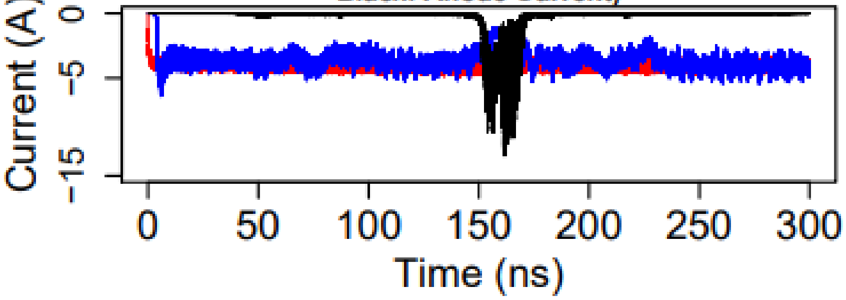

(b) Current Analysis
(Red: Emitted Current; Blue: Cathode Current;
Black: Anode Current)

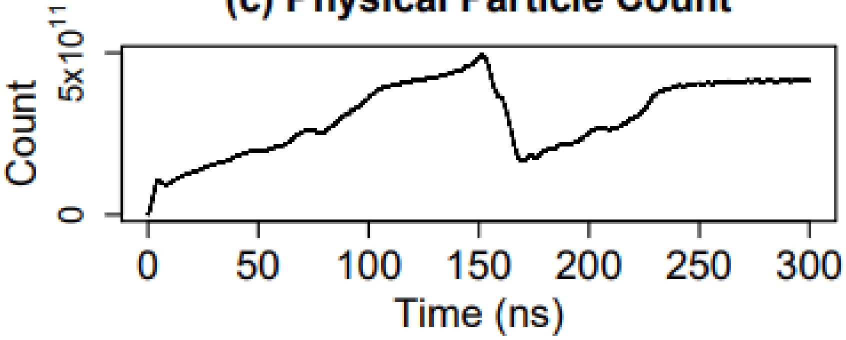

(c) Physical Particle Count

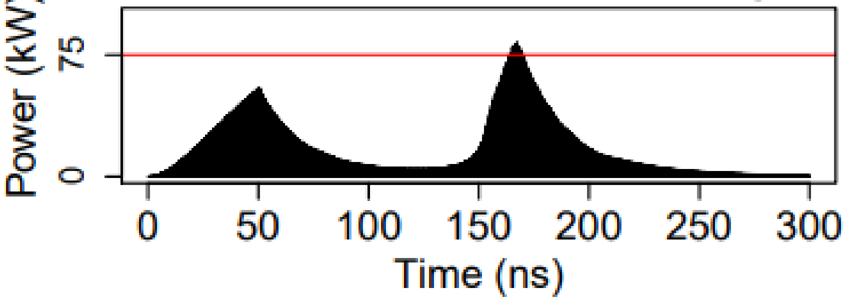

(d) Power Analysis
(Black: Output Power; Red: Power Target)

Figure VIII-9 Simulation results for the CWM-75kW magnetron simulation with RF priming showing (a) cavity voltage; (b) emission, anode, and cathode currents; (c) number of simulated macroparticles; (d) RF power (red line denotes the power target at 75 kW).

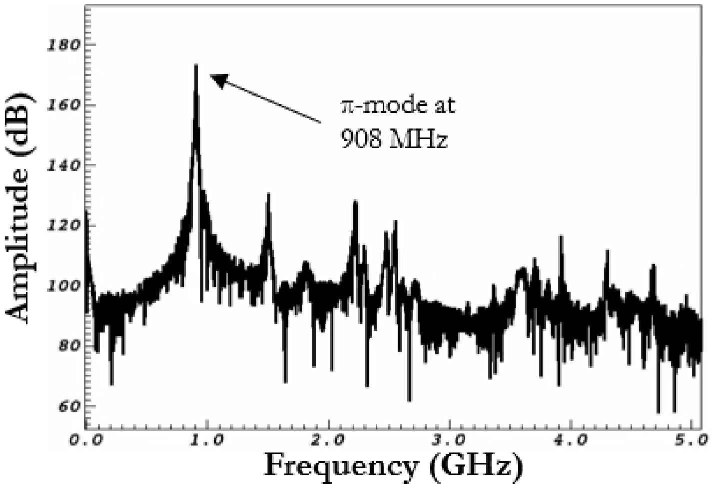

Figure 0-10 FFT of the simulated cavity voltage for the CWM-75kW magnetron simulation with RF priming.

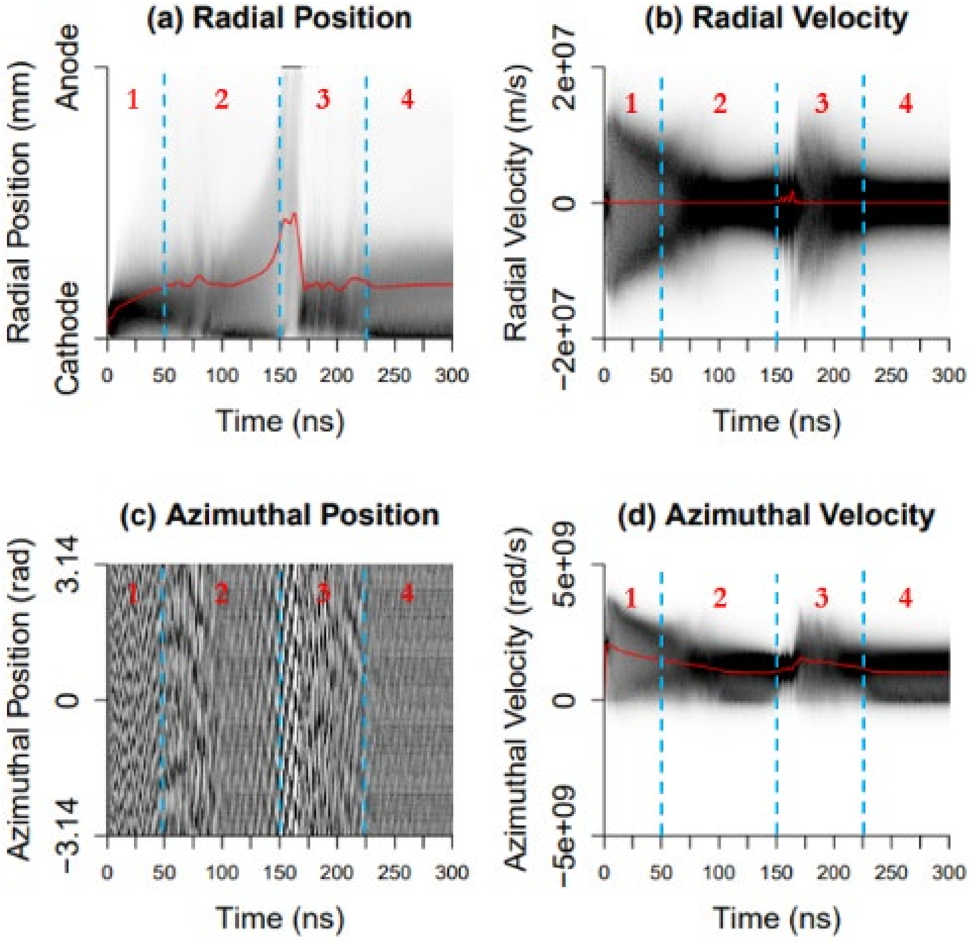

Figure VIII-11 Electron population plots for the CWM-75kW magnetron simulation with RF priming showing (a) radial position; (b) radial velocity; (c) azimuthal position; (d) azimuthal velocity. In subplots (a), (b), and (d), red lines indicate average. Darker color denotes higher probability.

in radial and azimuthal velocity. The oscillation never reoccurs for the remainder of the simulation (Figure 0-11, region 4). Note that the azimuthal position plots do not show the clear spoke horizontal lines as the data dump time did not match the oscillation frequency.

The device has a loaded Q of about 100. The cavity voltage should decay in tens of nanoseconds after the RF priming was shut off; however, as can be seen from the cavity voltage plot in Figure 0-9.a, after some initial decay, from 50 ns to 100 ns, the cavity voltage held at a relatively constant level from approximately 100 ns to 140 ns, before expanding again right before oscillation. Some factors prevent further decay of the cavity voltage after 100 ns and hold it at a relatively constant level before oscillation. It appears that some aspect of electron population, possibly the azimuthal velocity distribution, allows oscillation to start at 150 ns. This speculation is based on the convergence of the azimuthal velocity distribution persisting after the RF priming was shut off at 50 ns until the device reaches oscillation at 150 ns. Striations in the azimuthal position plot also show some positional remnants clearly related to RF priming, but how these patterns describe the device operation is not yet clear. As seen in the cavity voltage plot (Figure 0-9.a), there is still an oscillating cavity voltage long after RF priming is terminated (many RF periods); hence some part of the electron population appears to be supporting this field.

The breadth ratio in radius (Figure 0-12.a) stayed around 1:1 other than the brief 20 ns period in regions when the ratio tried to break away above 1:1. It is worth noting that even though a super-spoke event occurred at this time, in which a large number of electrons were absorbed by the anode, the breadth ratio only went to as high as 1.5:1

positive, which is still a low value. The breadth ratio in azimuth surged to as high as 100:1 positive in region 3 before collapsing and eventually settled at about 15:1 positive, which is the same level observed in the case without priming. Note the dipping pattern in the plot for breadth ratio in azimuth is observed before oscillation similar to the observations made in the 2D cases.

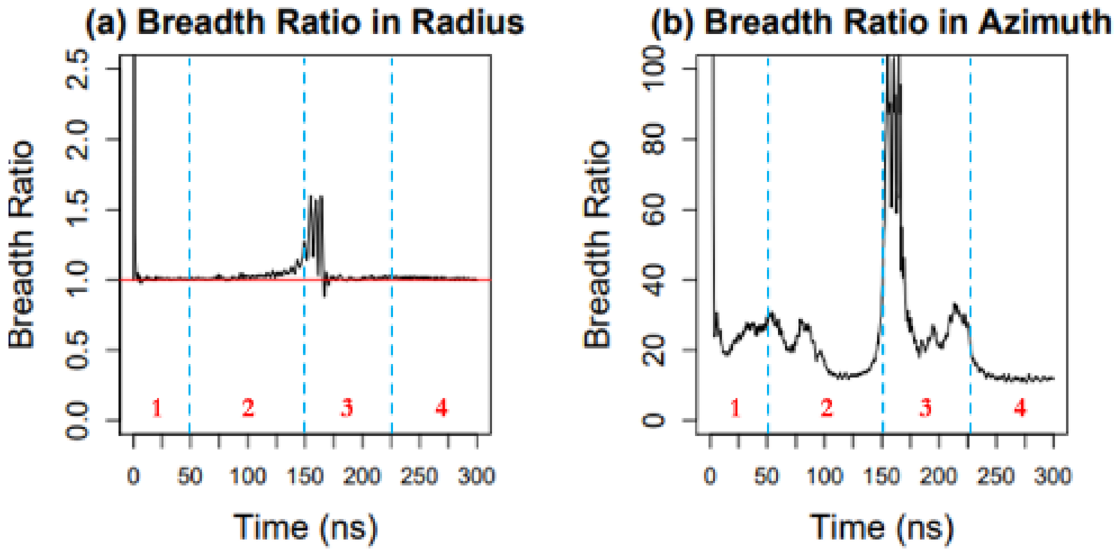

Figure VIII-12 Breadth ratios for the CWM-75kW magnetron simulation with RF priming. (a) Breadth ratio in the radial direction; (b) breadth ratio in the azimuthal direction.

8.5 Magnetron Startup with Cathode Modulation

In this case, electrons were injected in five evenly spaced locations around the cathode, and these injection spots rotate around the cathode as a function of time at 908 MHz to drive the π-mode. This approach is similar to that described here [15-17]. Additionally, a ten-sided cathode was used to match the planned experimental cathode approach as also described for the previous Rising Sun research [15-17]. Figure 0-13 shows the cross-sectional electron distribution at various time instances: (a) 0.5 ns, (b) 10 ns, (c) 100 ns, and (d) 180 ns.

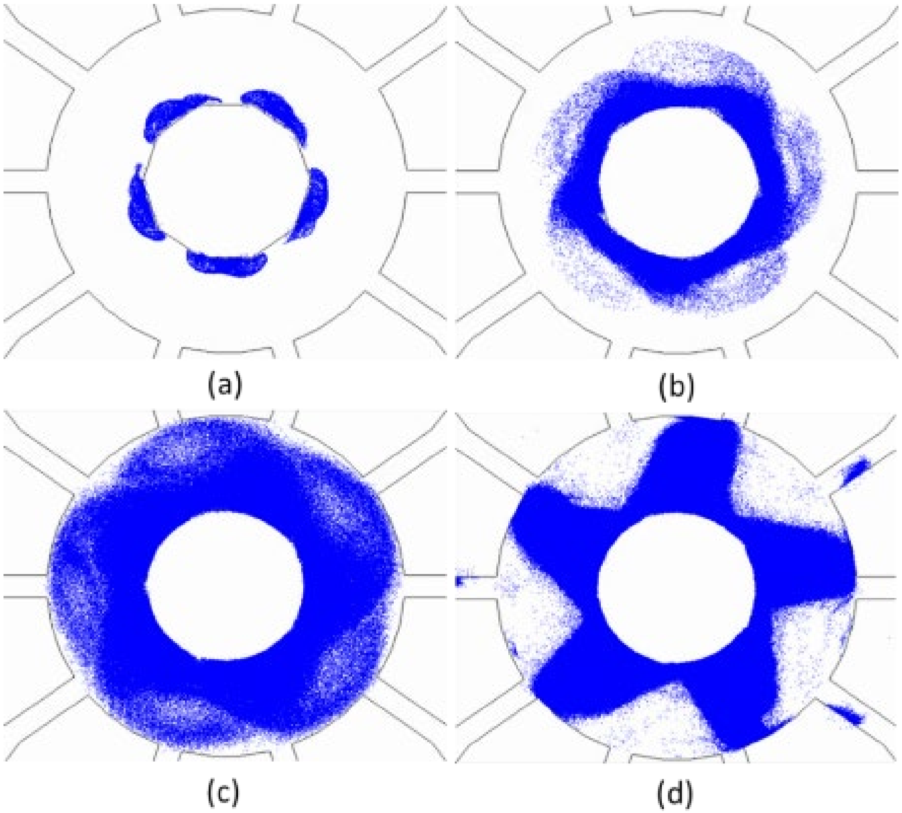

Figure VIII-13 **Cross-sectional electron distribution under cathode priming. a) 0.5 ns; b) 10 ns; c) 100 ns; d) 180 ns.**

In this case, the five-spoke π-mode pattern emerged right away, within 10 ns, and became more and more pronounced with time. Unlike in the RF primed case, the spokes had a steady build-up with no breakdown in the process. The results shown in Figure 0-14 confirm this observation. The cavity voltage and power build-up were steady. Once oscillation begins, a spike in the anode current like that of the RF priming case was observed, which again indicates the existence of super-spokes. Nonetheless, this cathode priming case showed much better oscillation stability than the RF priming case in the

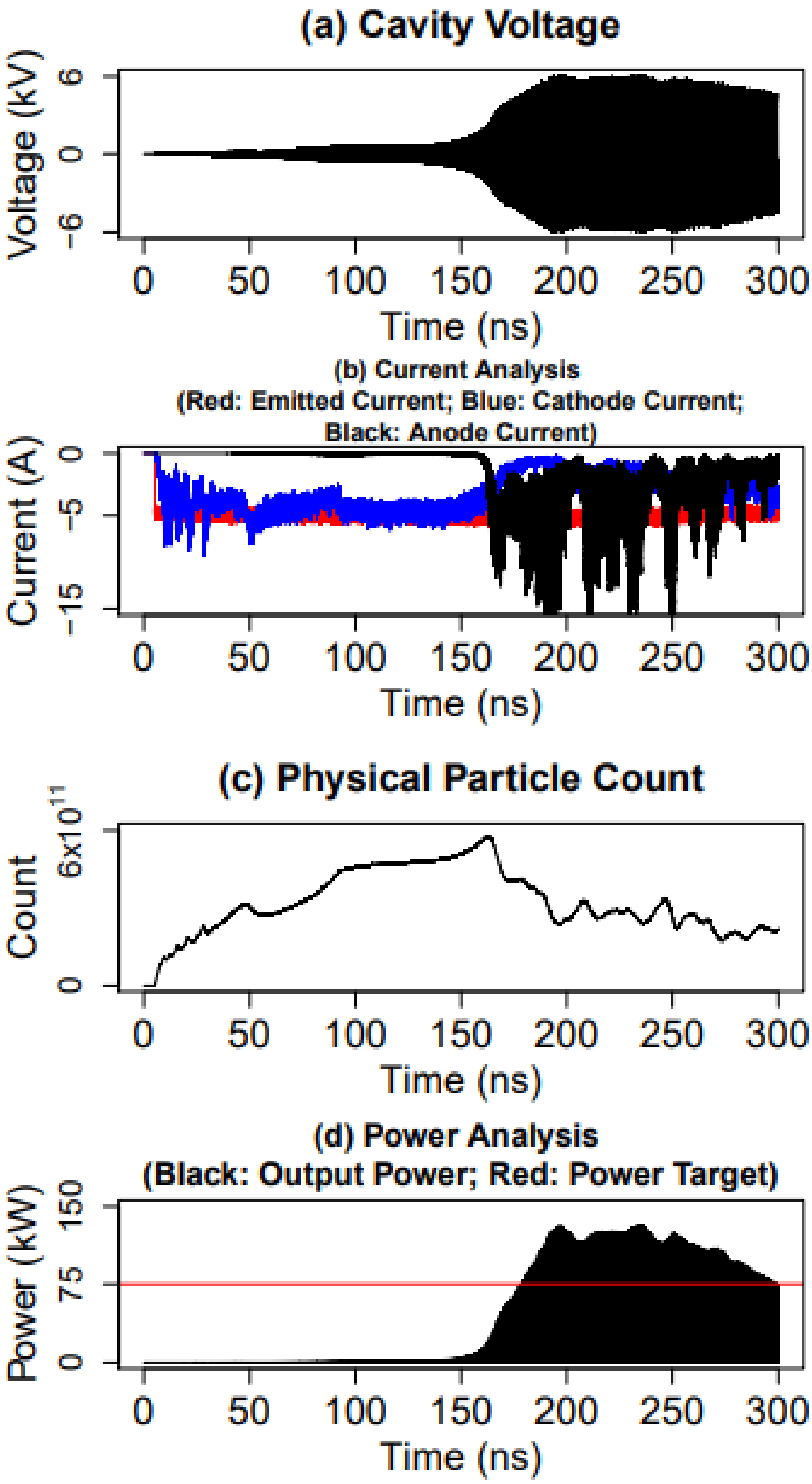

Figure VIII-14 Simulation results for the CWM-75kW magnetron simulation with cathode modulation showing (a) cavity voltage; (b) emission, anode, and cathode currents; (c) number of simulated macroparticles; (d) RF power (red line denotes the power target at 75 kW).

sense that cavity voltage oscillation lasted much longer and did not collapse right away. Curiously, the FFT of the cavity RF voltage, shown in Figure 0-15, shows the simulated device was oscillating at 910 MHz, slightly more than the 908 MHz π-mode frequency, which is also the frequency of the modulated electron injection. This shift in frequency is possibly caused by a loading effect; however, the precise mechanism of this loading effect and why it was not observed in the previous cases is currently unclear.

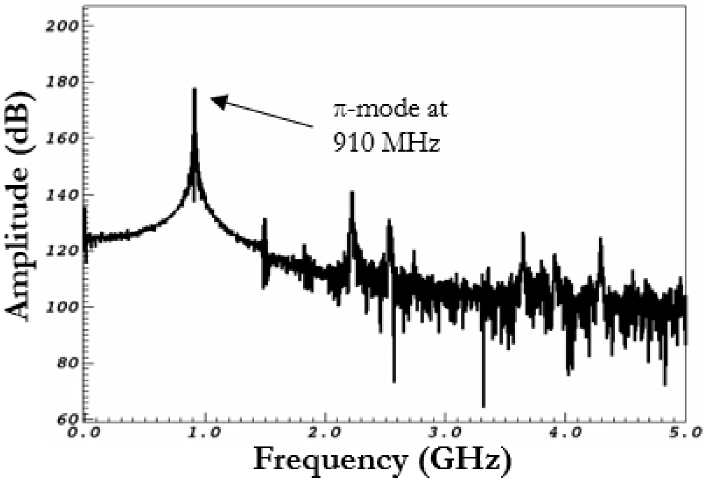

Figure VIII-15 FFT of the simulated cavity voltage for the CWM-75kW magnetron simulation with cathode modulation.

Cathode priming was applied continuously throughout this simulation. The electron population plots for this case (Figure 0-16) showed many different patterns compared to the previous two cases. The plots are divided into 4 regions. In this case, there was sustained spoke formation before the oscillation was finally reached. The radial position plot does not show the majority of electrons collapsing back after their initial attempts to move into the anode-cathode gap, like the previous two cases; instead it seems that the simulated device tried to begin oscillation shortly after startup but failed (Figure 0-16, regions 1 and 2), and the radial velocity collapsed while the radial position did not (Figure 0-16, region 3). Once the device began oscillating at 180 ns, the radial velocity plot shows increased and then sustained activity (Figure 0-16, region 4). The azimuthal position and velocity plots both indicate strong and sustained bunching after the oscillation began. The striations in the azimuthal and radial position plots are intriguing and show the transition of the

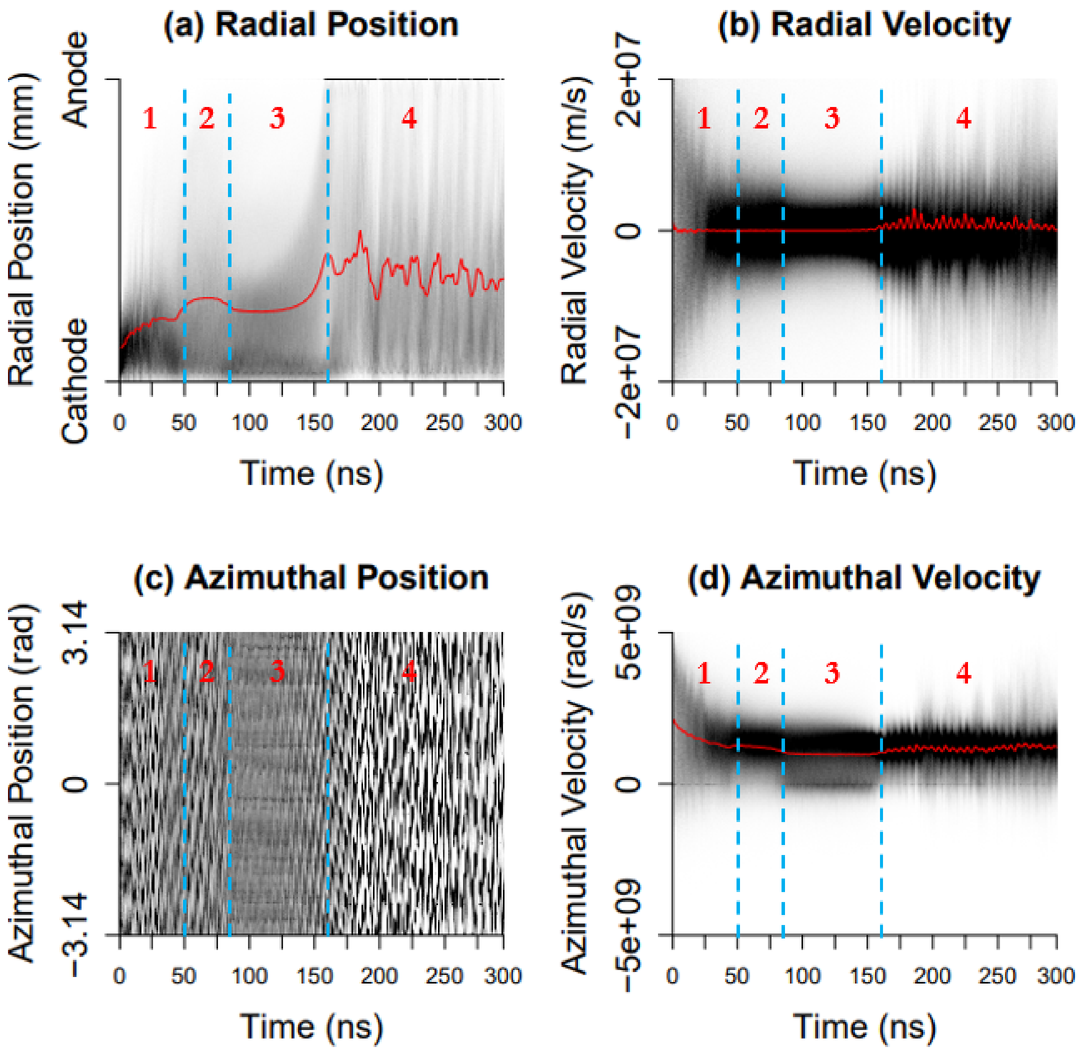

Figure VIII-16 Electron population plots for the CWM-75kW magnetron simulation with cathode modulation showing (a) radial position; (b) radial velocity; (c) azimuthal position; (d) azimuthal velocity. In subplots (a), (b), and (d), red lines indicate average. Darker color denotes higher probability.

magnetron from spoke formation to actual oscillation. On the other hand, the clean striation pattern in the azimuthal position only lasts for about 40 ns at the beginning of

Figure 0-16 region 4 (from 150 ns to 190 ns); then the pattern begins to fall apart. It is likely that there are undesired modes present. Again, the device physics indicated by these results still needs to be understood.

The breadth ratio in radius (Figure 0-17.a) stayed around 1:1 before the simulated device began to oscillate at about 160 ns; note that the breadth ratio only went to as high as 2:1 positive after oscillation began and appears to be collapsing near the end of the simulation. In this case, the breadth ratio in azimuth (Figure 0-17.b) holds at about 10:1 positive in the 70 ns leading up to oscillation (region 3), suggesting high cycloidal electron motions. After oscillation began, the ratio had an initial surge to as high as 80:1 positive, but then the ratio appears to be collapsing heading into the end of the simulation. Note the dipping pattern in the plot for breadth ratio in azimuth is once again observed before oscillation.

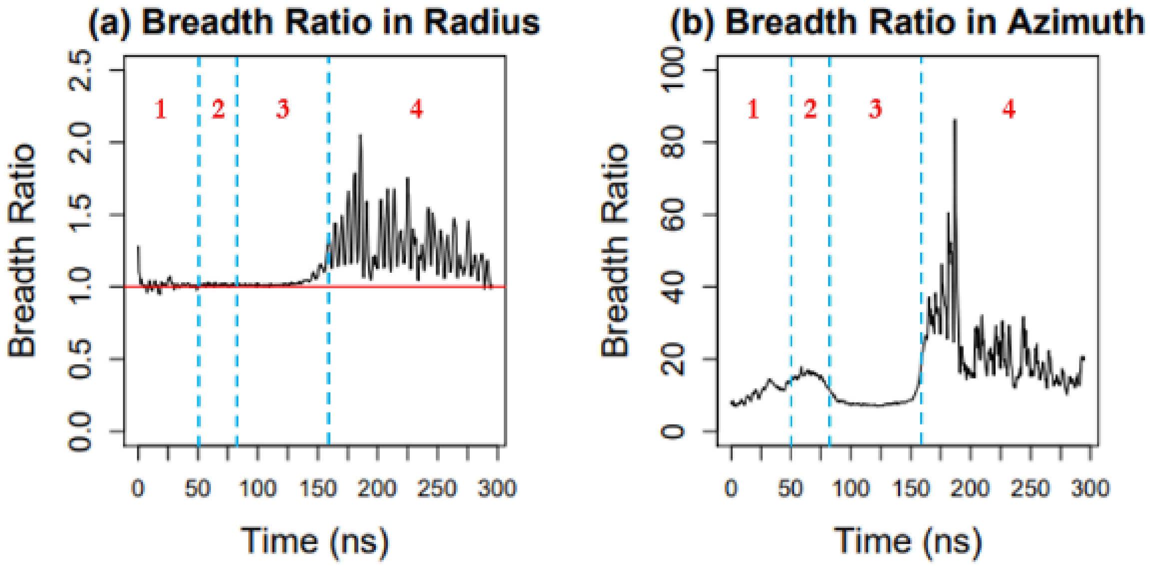

Figure VIII-17 Breadth ratios for the CWM-75kW magnetron simulation with cathode modulation. (a) Breadth ratio in the radial direction; (b) breadth ratio in the azimuthal direction.

8.6 Comparison to 2D Rising Sun Magnetron Results

In the RF priming case, while the modulation eventually induced oscillation, the electron population went through a transition, with spoke formation, collapse, and oscillation, unlike the prior 2D Rising Sun simulations where there was continued spoke formation leading up to oscillation. In the cathode modulation case of the 3D magnetron simulation, the electron spokes did not collapse; however, unlike our prior 2D Rising Sun magnetron results, the startup in the 3D simulation takes much longer (180 ns vs. 80 ns), and the RF phase of the oscillation is not stable. Hence, while the cathode modulation technique generated magnetron startup and led to a stable oscillation, the startup was much slower, and there is a clear period in which oscillation appears ready to occur (40-80 ns), but oscillation appears to be stalled. Understanding the cause of this effect requires consideration of the electron population.

8.7 Effects of the 10-sided Cathode

It was observed in both the current 3D model and the prior 2D Rising Sun model that the 10-sided cathode geometry leads to better startup behavior; there were even cases when the model would only oscillate with the 10-sided cathode geometry under certain priming conditions. The issue here, however, is that the simulation grid that was used is still relatively coarse, since everything is simulated in Cartesian coordinates, curved edges are handled by the Dey-Mittra cut cell algorithms [40]. When the edges are smooth, as it is the case for the circular cathode, the cut cell algorithm seems to handle the curved surface well, but the 10-sided polygon geometry involves sharp corners, which the cut cell algorithm does not seem to resolve very well, due to the discontinuity in the first and second derivatives of the geometry. Hence, although the geometry for the cathode is a 10-sided polygon, it is uncertain whether the simulation actually resolves a polygon. One potential solution is to adjust the mesh size and study its impact on the polygon geometry; another solution is to customize the simulation mesh so that all the polygon vertices are only on the mesh nodes. These solutions are for future study as they require much greater computational resources.

8.8 Study of Velocities

Figure 0-18 offers a direct comparison of the velocity (radial and azimuthal) plots across all three cases. In the no priming case, the radial velocity establishes an approximately equal magnitude of positive and negative traveling electrons as would be expected with no modulation. The priming cases show very different behavior. In cathode modulation, the electron population clearly made an early attempt to migrate toward the anode, but then the population collapsed. As indicated by the blue lines, the radial velocity plots begin to converge, and then “spikes” are seen at the beginning of oscillation for both priming cases. These spikes increase in amplitude during oscillation, showing some part of the electron population is increasing in radial velocity. In the RF priming case, this effect decreases as the oscillation collapses, but in the cathode modulation case, it continues with oscillation.

The azimuthal velocity plots show a far more intriguing result. In the no priming case, after an initial increase, the azimuthal velocity dips down, and the bulk of the electrons are relatively uniform with some electrons showing an azimuthal velocity dropping near zero. However, for the modulation cases, a very clear pattern is observed just before oscillation. While again the bulk of the electrons create a tighter azimuthal velocity pattern, some electrons dip in velocity. The dip patterns in the azimuthal velocity

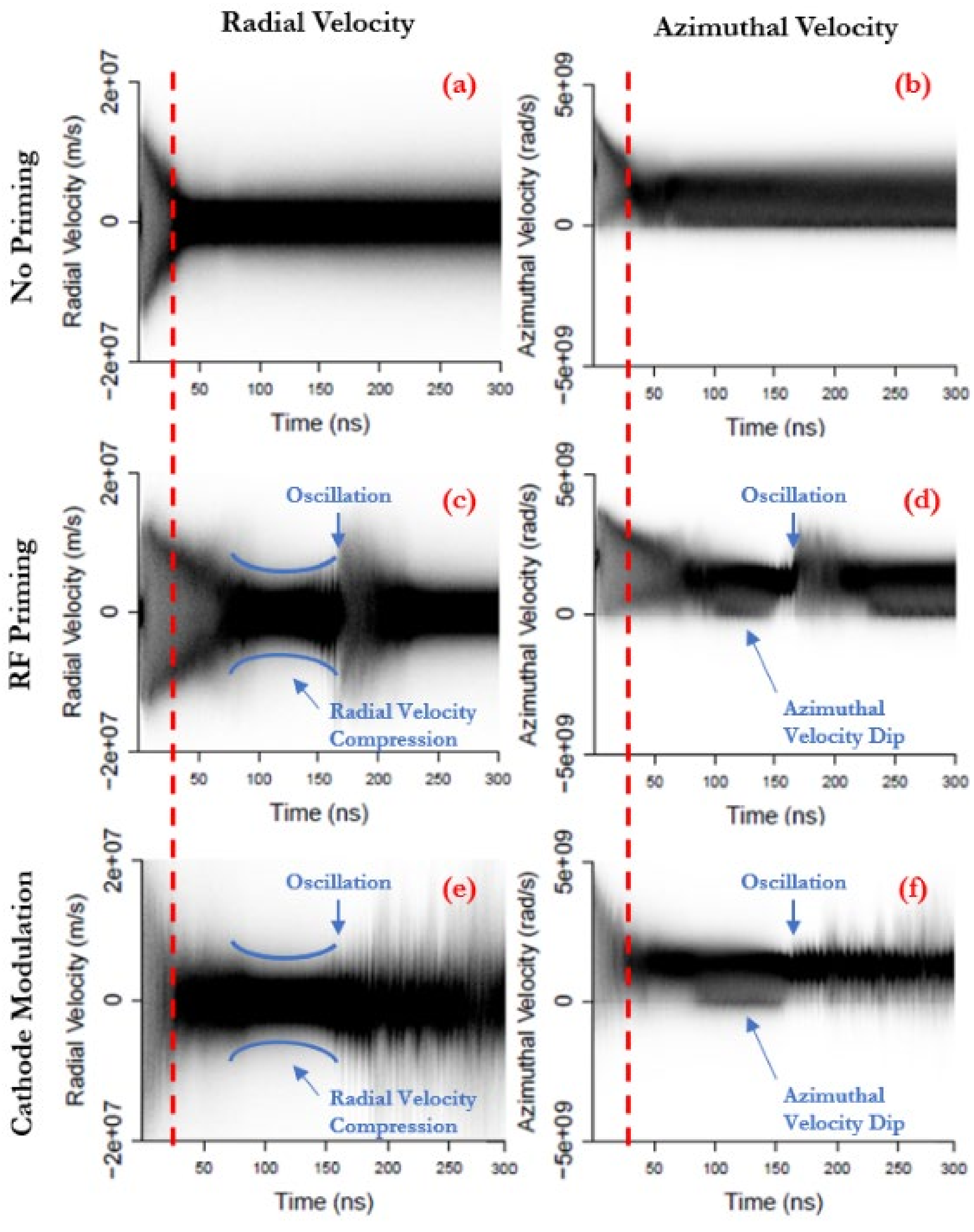

Figure VIII-18 Comparison of the radial and azimuthal velocities across three cases. (a) radial velocity for the no priming case; (b) azimuthal velocity for the no priming case; (c) radial velocity for the RF priming case; (d) azimuthal velocity for RF priming case; (e) radial velocity for the cathode modulation case; (f) azimuthal velocity for the cathode modulation case.

indicate portions of the electron population are traveling slower in the azimuthal direction, which suggest that these electrons' cycloidal motion have increased "hairpin" radii at the bottom of their cycloid, when the radial velocity goes to zero. In the cathode modulation case, leading up to oscillation, a portion of the azimuthal velocity even dipped deeply into the negative velocity direction, indicating a portion of the electron population is traveling counter to the direction of spoke rotation in the azimuthal direction as they form a loop at the bottom of their cycloidal motion. Then the azimuthal velocity shows a narrowing of the velocity spread, followed by clear spikes in the distribution. In both cases, the azimuthal velocity patterns show the narrowing and the transition to oscillation. The RF priming case has a very large velocity excursion, possibly indicating spoke collapse, before returning to the same pattern as before. The cathode modulation case, in contrast, shows smaller velocity spikes and a relatively stable pattern as oscillation continues. The precise implications of these observations still require further investigation, including a better understanding of the electron kinetic vs. potential energy and the electron momentum distributions [6], [23].

CHAPTER NINE: ELECTRON POPULATION COMPARATIVE ANALYSES

There were some reoccurring observations in analyzing the breadth ratios for both the 2D cases and the 3D cases. To make the comparison easier, Figure 0-1 compares all breadth ratio plots from the 2D Rising sun magnetron simulation and Figure 0-2 compares all plots from the 3D CWM-75kW magnetron simulations.

For all breadth ratios in radius, the 1:1 level is always an important reference level because this is the break-even level of the net motion of the electron population in radius. As discussed previously, for there to be charge transfer from the cathode to the anode (i.e. net electron motion toward the anode), the breadth ratio in radius must be above the 1:1 level. For there to be steady state oscillation, the breadth ratio in radius must hold at some positive level above the 1:1 level. In a narrow sense, magnetron startup is a process in which the breadth ratio in radius breaks away from the 1:1 break-even level and moves above 1:1.

Out of all six cases across the two models, the only two cases that reached steady state oscillation are the 2D Rising Sun magnetron simulations with no priming and with RF priming. For both cases, the breadth ratios in radius show a “break away and hold” pattern. This region is seen in Figure 0-1 as indicated by the green ovals for the breadth ratio in radius. This pattern seems to signify clean and successful startups. On the other end of the spectrum, in the no priming case for the CWM-75kW magnetron simulation, the breadth ratio fails to break away from the 1:1 level throughout the simulation, which corresponds to a complete failure to oscillate. This region is again indicated in

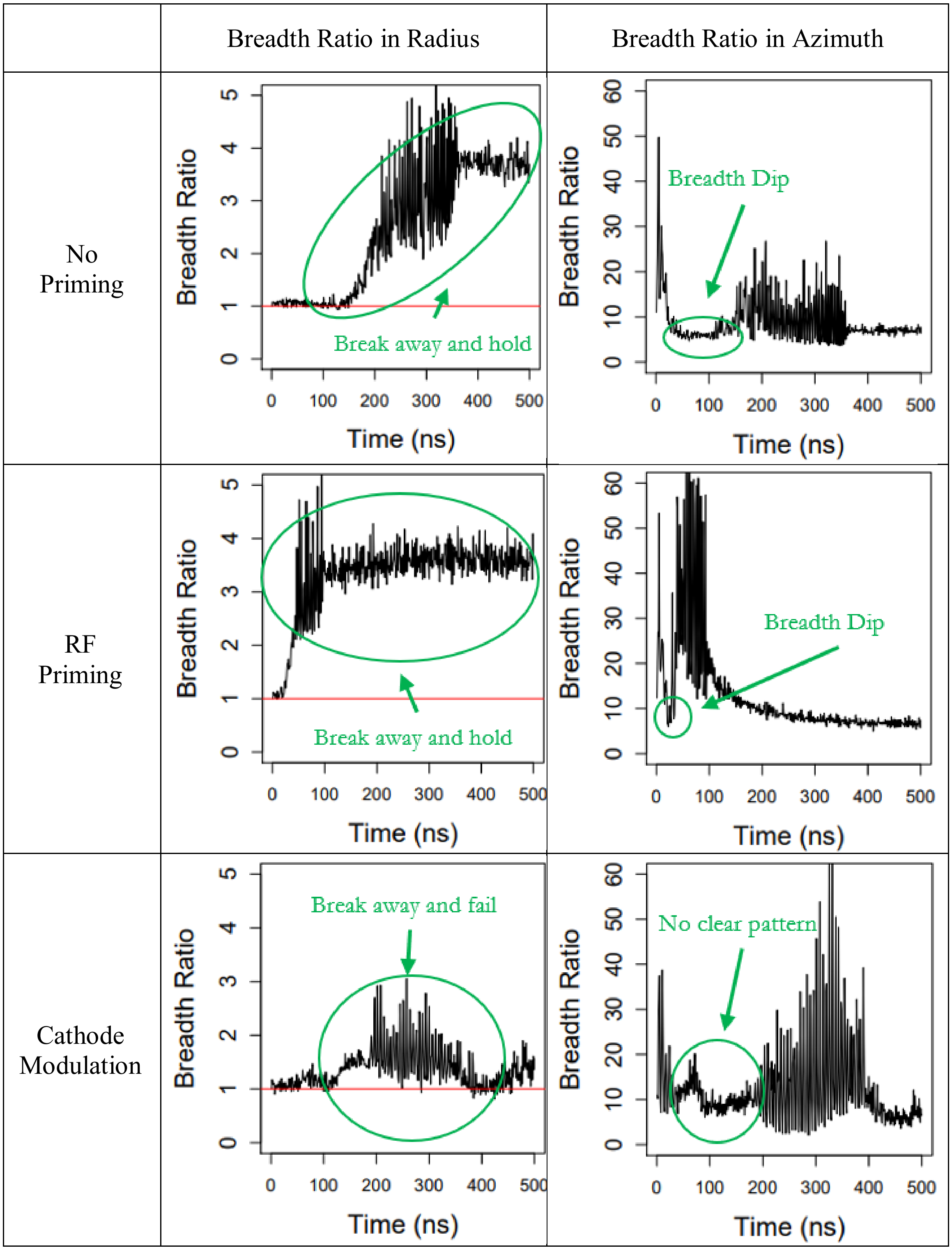

Figure IX-1 Breadth ratios from all 2D Rising Sun magnetron simulation cases.

	Breadth Ratio in Radius	Breadth Ratio in Azimuth
No Priming	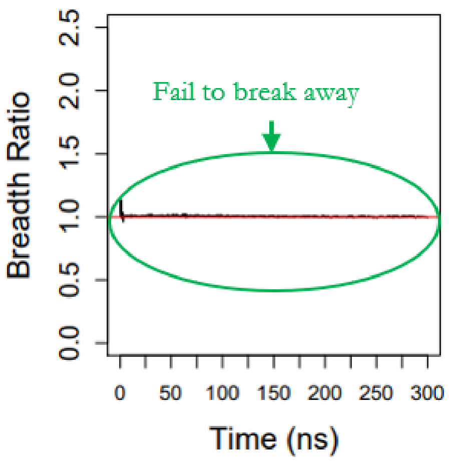	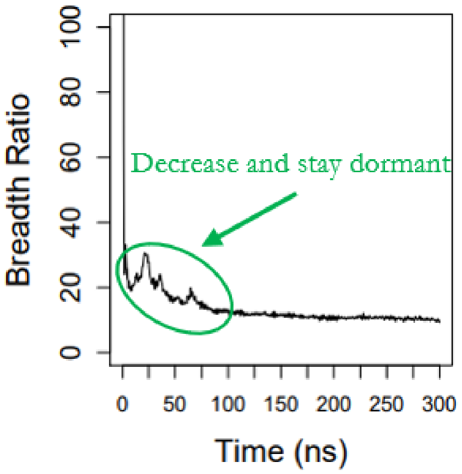
RF Priming	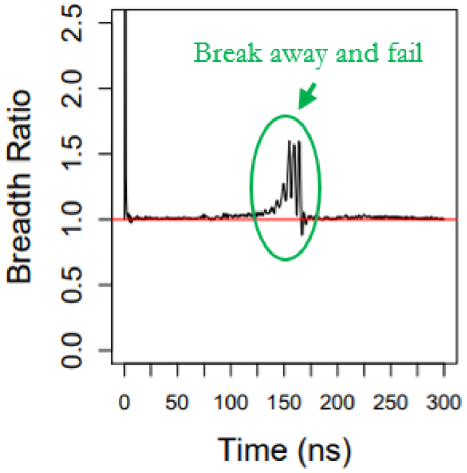	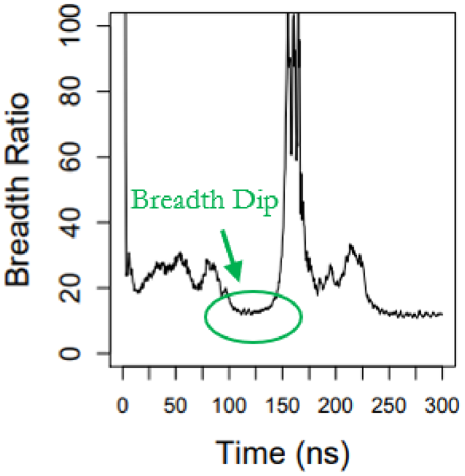
Cathode Modulation	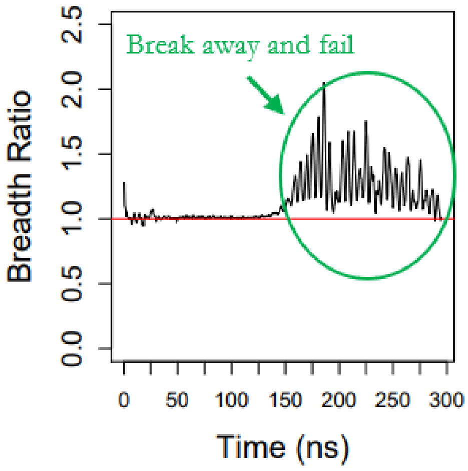	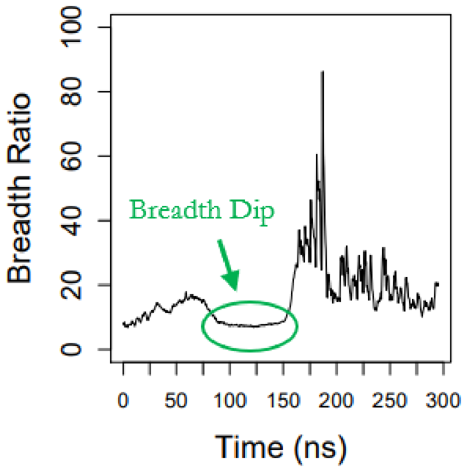

Figure IX-2 Breadth ratios from all 3D CWM-75kW magnetron simulation cases.

Figure 0-2 for the 3D model with no priming. In the other three cases, the 2D Rising Sun magnetron simulation with cathode modulation, the CWM-75kW magnetron simulations with RF priming and cathode modulation, the breadth ratios in radius all display a "breakaway and fail" pattern as indicated. As the ratio breaks away from 1:1, it eventually collapses back toward the 1:1 level. The breadth ratio in radius falling back to the 1:1 level corresponds to the electron spokes collapsing and the electron population losing internal support for moving towards the anode.

Note the observations discussed in the previous paragraph suggest that the breadth ratio in radius is a concurrent indicator with respect to the state of oscillation. Its values seem to change simultaneously with the state of oscillation. As oscillation begins, the breadth ratio in radius breaks away from the 1:1 level and moves into the greater than 1 regime. Whether the breadth ratio in radius hold at levels within the greater than 1 regime seems to correlate strongly with the stability of the oscillation. Hence, the breadth ratio in radius is concurrent with the state of oscillation, and it clarifies the state of oscillation.

In contrast, the breadth ratio in azimuth consistently shows a dipping pattern during the period before oscillation begins. This pattern is observed in all simulation cases that oscillated except for the 2D Rising Sun magnetron simulation with cathode modulation case; it is probable that this case is an anomaly, since this is the only case in which the emission current was space charge limited from the beginning of the simulation to the time when oscillation begins, as shown in Figure 0-3 where the emission current is observed to reach saturation quickly. This effect is likely due to the injection of electron into existing spoke regions. Based on this observation, it is probable that oscillation was reached in the 2D Rising Sun magnetron simulation with cathode modulation case with very different mechanisms compared to the other simulation cases that reached oscillation, in which cases a space charge limited emission current was not observed.

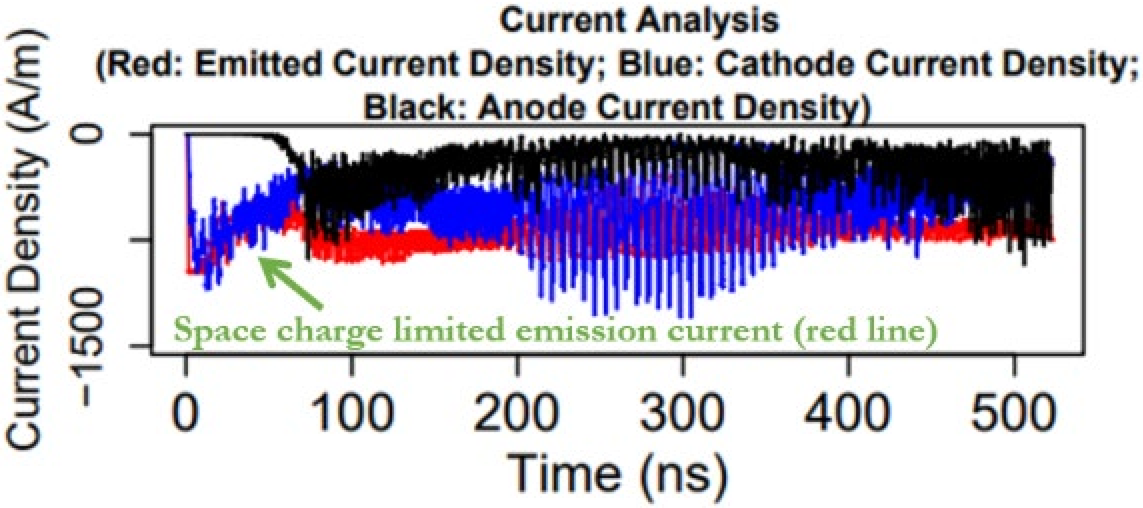

Figure IX-3 Replica of Figure 0-15(b) with added comments showing the emission current was space charge limited from the beginning of the simulation to the time when oscillation begins in the 2D Rising Sun magnetron simulation with cathode modulation case.

Different from the breadth ratio in radius, the breadth ratio in azimuth seems to behave as a leading indicator with respect to the start of oscillation. The dipping pattern consistently appears during the period before oscillation begins. To further examine this dipping pattern in the azimuthal breadth ratios, the ratios are plotted alongside each with the radial position probability distribution plots and the breadth ratios in radius. This combination of plots was chosen because they reveal some interesting insights when analyzed in conjunction. Figure 0-4 shows the combination plots for the CWM-75kW magnetron simulation results with RF priming and cathode modulation. Note that the observations to be discussed blow are also true for the 2D Rising Sun magnetron simulation results with no priming and with RF priming, though the resulting plot

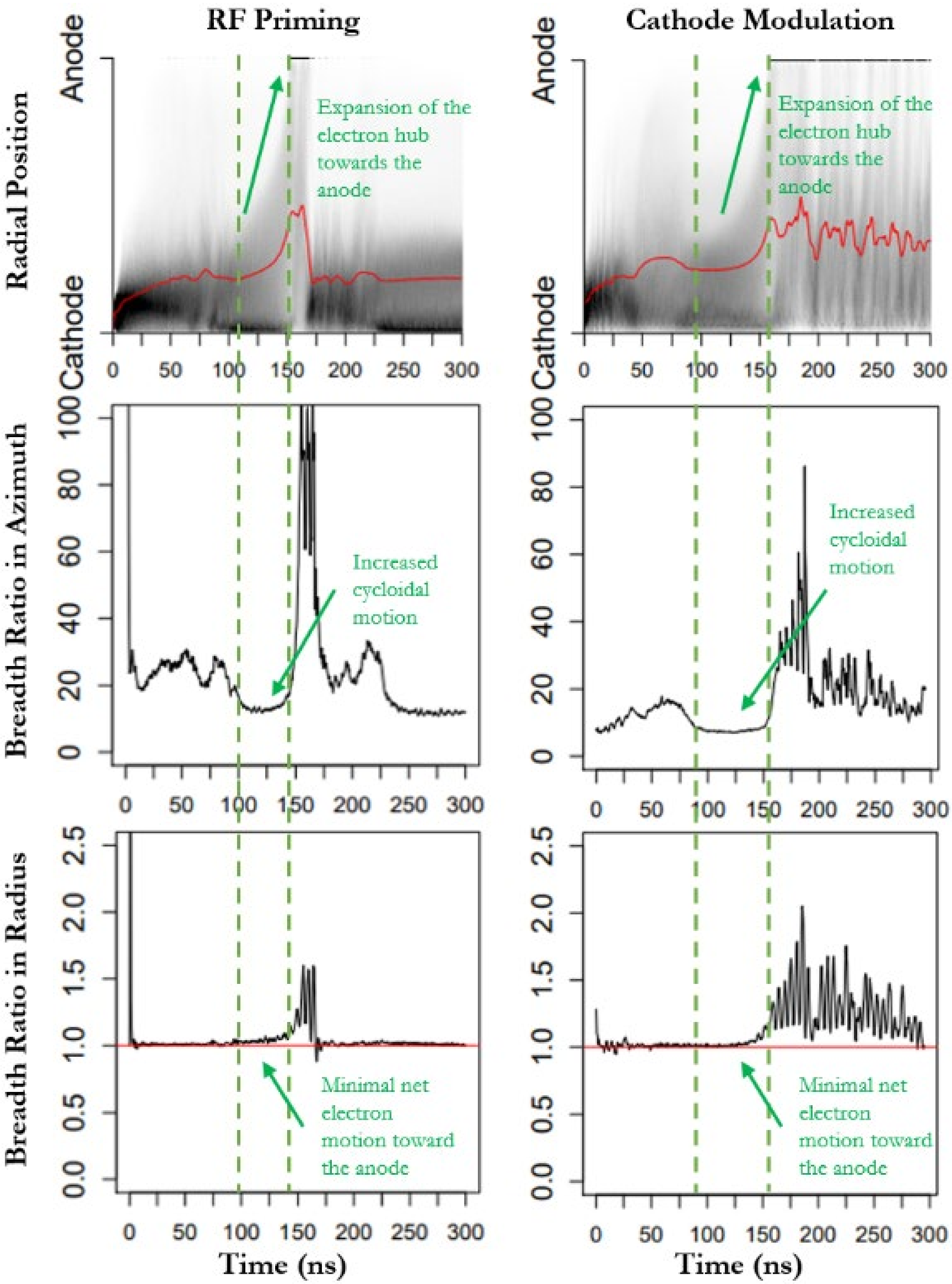

Figure IX-4 Selected analysis results from the CWM-75kW magnetron simulation with RF priming and with cathode modulation. For each case (column), the radial position probability distribution plots (first row), the breadth ratios in azimuth (second row), and the breadth ratio in radius (third row) are shown.

patterns from the Rising Sun magnetron simulations are less pronounced. The CWM-75kW magnetron simulation result with no priming is not shown as the simulated model did not oscillate. The Rising Sun magnetron simulation result with cathode modulation was also not used due to the space charge limited emission current issue discussed previously.

Both cases shown in Figure 0-4 display nearly identical patterns during the period leading up to oscillation, as annotated in the plots. The interesting aspect of this comparison is that the radial breadth ratios for both cases stayed very close to the 1:1 level before oscillation begins, indicating minimal net electron motion toward the anode, yet the radial position probability distribution plots show the outer edges of the electron hubs expanding toward the anode (100-150 ns time range) as indicated by the arrow. This observation suggests that the expansion of the electron hub towards the anode prior to oscillation is not supported by <u>net electron motion</u> toward the anode in the radial direction, but by some other mechanisms. This observation is supported by the radial breadth ratio plots which have values near 1:1 as annotated. Hence, while electrons are moving toward the anode in this time period just before oscillation, an approximately equal number of electrons are moving back toward the cathode. With this observation, it is natural to look at the correlation between breadth ratio in azimuth and the expansion of the electron hub. By the patterns shown in Figure 0-4, there exist strong correlations between the expansion of the electron hubs during periods before oscillation and the increased cycloidal motion of the electron populations, as shown by the azimuthal breadth ratios. Note that these correlations do not necessarily imply causation one way or the other; nevertheless, what these observations have clearly shown is that the expansion of the electron hubs during periods before oscillation and the increased cycloidal motion of the electron populations occur concurrently.

The precise explanations of these observations require future investigation. One hypothesis is that the increased cycloidal motion of the electron population results in agitation that forces the electron hub to expand in radius, because the re-entrant nature of the electron hub in a cylindrical geometry limits the electron hub from expanding azimuthally. Once the outer edge of the electron population reaches the anode, the radial breadth ratio breaks away from the 1:1 level, which enables charge transfer from the cathode to the anode and starts oscillation. Note that this expansion of the electron hub is affected by the strength of confinement determined by the E/B ratio; it is also affected by feedbacks from the anode circuit. The mechanisms of these interactions are also topics for future research.

CHAPTER TEN: CONCLUSIONS AND FUTURE WORK[2]

10.1 Conclusions from Current Results

This dissertation surveyed important aspects of magnetron physics, as well as some of the recent state-of-the-art research on the magnetron. A comprehensive description of the inner workings of the VSim PIC-FDTD simulation code was offered along with detailed descriptions of two novel data analytic techniques developed for this research to analyze VSim simulation results: the electron population analysis and the breadth ratio analysis. The electron population analysis aims to answer the question, “what is the likelihood of finding an electron at a certain special location at a specific time”, by constructing the normalized probability distribution of the positions and velocities of the electron population in separate cylindrical axes and plotting them against time. The electron population analysis reveals ways by which the positions and velocities of the electron population are behaving; these behaviors are not easily recognizable by observing a simple electron distribution plot. The breadth ratios analyses extracts, for each axis, the ratio between electrons moving one way versus electrons moving the other way. The breadth ratio in radius indicates the strength of the internal support for charge transfer from the cathode to the anode; the breadth ratio in azimuth indicates how cycloidal the electrons are. These data analytic schemes enable unique insights into the

---

[2] Parts of this chapter have been published by Andong Yue, et. al. in Journal of Vacuum Science & Technology B 39, 022201 (2021); https://doi.org/10.1116/6.0000809

behavior of the electron population that could lead to potential breakthroughs in the understanding of magnetron physics.

The 2D Rising Sun magnetron model was simulated with three different priming conditions. While the simulation model was developed in previous research performed at Boise State University, this research applies the new data analysis schemes to the simulation results and reveals physical insights that were not available to the previous research. The analysis result show that there was intense mode competition during start up. In both the no priming case and the RF primed case, the simulations were able to reach steady state and oscillate in the π-mode. Despite the RF priming power being less than 1% of the device's output power density in full oscillation, the RF primed case reached steady state oscillation much quicker than the no priming case (100 ns vs. 350 ns). This observation indicates that the 2D Rising Sun model is very sensitive to priming. For the cathode modulation case, while the modulated electron injection led the simulation to oscillate in the π-mode as early as 80 ns, the oscillation did not stabilize and soon collapsed to the 3π/5-mode, which is not the desired mode.

Previous research has found that the addition of a small percentage of uniformly injected current greatly mitigates the instability in the cathode modulation case [52]; however, the analysis of such a setup has not been conducted and will be work for the future. In both cases that reached steady state oscillation, the breadth ratio in radius stabilized at about 3.8:1 positive, which indicates steady internal support for charge transfer from the cathode to the anode after steady state was reached; the breadth ratio in azimuth stabilized at about 8:1 positive, which suggests the electron population was still cycloidal even after the simulation was oscillating in steady state, likely because of the continuous injection of new electrons.

There are several conclusions from the simulation results of the CWM-75kW: 1) the RF priming case shows the device to oscillate at 150 ns when the electron hub seemingly collapsed after RF priming was shut off at 50 ns, which indicates the device retained some property as the result of the RF priming; 2) the cathode modulation case suggests that cathode modulation offers better oscillation stability, at least in this particular simulation model, when compared to RF priming; 3) the increased “hairpin” radii of the electron cycloidal motion and compression of the radial velocities were observed leading up to oscillation in both the RF priming case and the cathode modulation case. In both cases, the oscillation collapsed due to super-spokes, which cause spikes in the anode current that lead to rapid loss of electrons. The causes of these super-spokes are unclear at this point. The azimuthal velocity probability distribution plot for the RF priming case shows a converging pattern that persisted after the RF priming was shut off, which suggests that some aspect of startup is stored in the azimuthal velocity. In the cathode modulation case, the disorder in the azimuthal position plot that emerged 40 ns after oscillation indicates the existence of undesired RF modes. The suppression of these undesired modes could be the key to improving the magnetron phase drift. The azimuthal velocity plots just prior to oscillation show that some electrons reach a low velocity at the bottom of the cycloid orbit and some electrons even move in the opposite direction. This dip is very similar to that seen in the 2D simulation. It is unclear if this is a cause or an effect of the oscillation start but could provide a method to study magnetron oscillation startup by programming the electron population. The breadth ratios in radius were low across all three cases. Even during the times when super spokes were observed, the breadth ratios in radius only went to as high as 2:1 positive and quickly collapsed to 1:1. The low breadth ratios in radius indicate a lack of internal support for the electrons to migrate toward the cathode, which suggest aspects of the simulation model's set up is likely not optimal; future work will refine and optimize the current simulation model.

The comparative analyses of all results across the two simulation models show that there exist strong correlations between increased cycloidal motion of the electron population and the expansion of the electron hub toward the anode. And a net electron motion towards the anode does not occur until some part of the electron hub reaches the anode and the device begins to oscillate.

It is worth noting here that these new analysis schemes, while still in the early stages of their development, have shown promise in revealing a better understanding of the electron device physics in magnetron startup. Although these analysis schemes are developed for analyzing magnetron simulation results, they might be applied to analysis of electron populations of other vacuum electron devices and possibly plasma devices.

10.2 Future Work

The next steps for this research include further improvements to the analysis schemes in terms of accuracy and resolution; an improvement in resolution is expected to reveal additional details that could lead to further understanding of the electron population during magnetron startup. The relationships between the observations, such as the azimuthal breadth dip, and the event of oscillation startup will be studied quantitatively as statistical correlations. The azimuthal position and velocity plots will be broken down into different radial sections in future analysis. These spatial regions will show the differences in the electron populations near the cathode compared to those near the anode as oscillation starts.

The results presented in Chapters Seven and Eight are all cross-sectional analysis, in the sense that particle statistics were performed within discrete timesteps. Analysis schemes and codes are currently being developed to analyze the data in terms of time-series, in which particles are tracked across timesteps to form trajectories, and then statistics can be performed, based on the particle trajectories, to extract a distribution of trajectories. This new tool will further enable the study of particle trajectory behaviors within the magnetron's interaction space during startup under different priming conditions. These efforts include studies of the Slater orbits and particle trajectory autocorrelation. Of particular interest is the breakdown of the electron cycloidal flow into Brillouin flow by studying the electron orbits and their effects on oscillation. The goal is to investigate what types of particle trajectory behavior create a favorable environment for the magnetron to oscillate.

Studies of the trajectory autocorrelation could reveal important information regarding the mechanisms by which particle-field interaction and azimuthal velocity bunching occur during the magnetron's startup process. Some preliminary work has been performed to study the trajectory autocorrelation; however, the analysis so far on particle trajectory autocorrelation was performed based on a very small portion of the electron population and no clear observation has been made. The next step is to scale up the analysis to include the entire electron population.

New preliminary work focuses on studying the physics of the electron population via the simulation of a model with a simple coaxial geometry. The coaxial model studied in recent simulations is a 2D model with a cathode radius of 0.01 m and an anode radius of 0.0244 m. The cathode and anode radii are the same as that of the 2D Rising Sun magnetron model; the major difference between the coaxial model and the Rising Sun magnetron model is that the coaxial model does not contain any resonant cavities. The goal is to first study the physics of the electron population when it is not subjected to perturbation due to the resonant cavities; then the results can be compared to the 2D Rising Sun magnetron simulation results. This work is currently ongoing; the following section will discuss some preliminary results.

The coaxial model was first simulated with parameters and setups that are identical to the one used in the 2D Rising Sun magnetron simulation with no priming. Additionally, current injection was shut off at 40 ns. The reason for shutting down electron injection at 40 ns is to prevent the statistics of the electron population over time from being distorted by newly injected electrons. This simulation yielded the breadth ratios shown in Figure 0-1. The breadth ratio in radius stayed near 1:1, indicating that the electron population had no net movement toward the anode. This is expected since the geometry is coaxial, and the device is operating under the Hull cutoff. The breadth ratio in azimuth offered extremely interesting insights. As electron injection was shut off at 40 ns, after which point there was no new electron entering the interaction space, the breadth ratio in azimuth exploded to as high as 240:1 positive. This observation suggests that the portion of the electron population that had stayed in the interaction space for some time (i.e., electrons that are not newly injected) exhibited behaviors that are close to

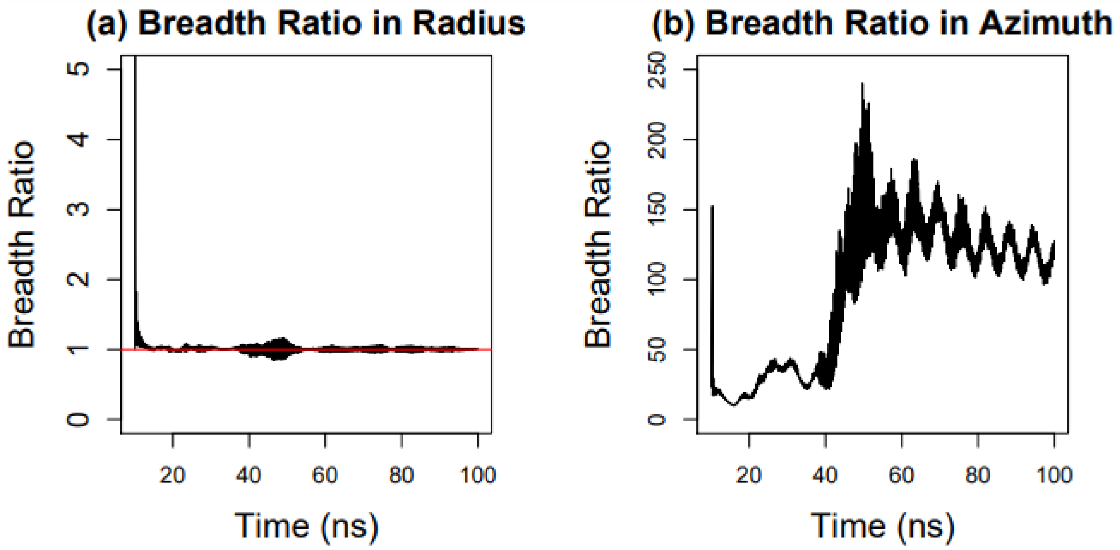

Figure X-1 Breadth ratios for the coaxial model with current injection being shut off at 40 ns.

Brillouin flow. Additionally, the breadth ratio in azimuth after 40 ns showed an oscillation pattern, suggesting the presence of some instability that is periodic in nature. The precise indications of these observations are subjects for future work.

Another analysis scheme currently in development aims to track the change of the electron trajectories' cycloidal radius over time. The current algorithm is only capable of tracking electrons one by one. The algorithm first organizes the electron's trajectory in temporally sequential order; then this sequence breaks down into temporal segments, each with the length of one RF period. Finally, the algorithm evaluates the difference between the smallest radial distance and the largest radial distance of the electron's trajectory within each RF period and plots the differences ("radial Δ") vs. time. Figure 0-2 shows the resulting plot from the radial Δ analysis for a single electron in the simulation of the coaxial model. The plot shows the radial Δ decreased over time, which suggests the electron was becoming less cycloidal as time progressed. If an electron is in ideal Brillion flow, the radial Δ is expected to be near-zero. No meaningful conclusion

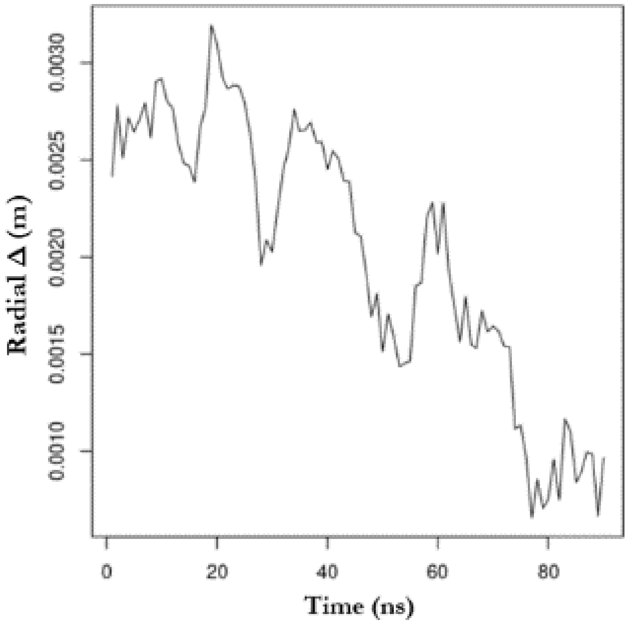

Figure X-2 Resulting plot from the radial Δ analysis for a single electron in the simulation of the coaxial model.

can be reached based on Figure 0-2 since it is the analysis result of only a single electron; however, as the scale of the analysis expands, the goal is to perform this analysis to every macroparticle within the simulation and construct a statical distribution of radial Δ vs. time.

Future work will focus on the development of scalable data analytic algorithms that are efficient to execute. It will also focus on the extension of existing and new data analytic schemes into the analysis of other MVEDs, including but not limited to cross-field amplifiers, traveling wave tubes, etc. to gain new insights into the fundamental physics behind these MVEDs.

REFERENCES

[1] J. M. Osepchuk, "Microwave Power Applications," *IEEE Transactions of Microwave Theory and Techniques,* vol. 50, no. 3, pp. 975-985, 2002.

[2] R. J. Barker, J. H. Booske, N. C. Luhmann and G. S. Nusinovich, Modern Microwave and Millimeter-Wave Power Electronics, Piscataway, NJ: John Wiley & Sons, Inc., 2005.

[3] D. M. Pozar, Microwave Engineering, 4th ed., John Wiley & Sons, 2012, pp. 705-707.

[4] T. G. vandeRoer, Microwave Technology Series, vol. 10, Boston, MA: Springer, 1994.

[5] R. P. Wadhwa, "Crossed-Field Microwave Devices," *IETE Journal of Research,* no. 24, pp. 418-437, 1978.

[6] G. B. Collins, Microwave Magnetrons, New York: McGraw-Hill, 1948.

[7] "Radio Progress During 1946," in *Preceedings of the IRE*, 1947.

[8] J. Goerth, "Early magnetron development especially in Germany," in *2010 International Conference on the Origins and Evolution of the Cavity Magnetron (CAVMAG 2010)*, Bournemouth, United Kingdom, 2010.

[9] W. E. Burcham, "The Magnetron," Bournemouth University, 26 July 2011. [Online]. Available: https://histru.bournemouth.ac.uk/Oral_History/Talking_About_Technology/radar_research/the_magnetron.html. [Accessed 9 December 2020].

[10] 'Percy Spencer Melts a Chocolate Bar, Invents the Microwave Oven," New England Historical Society, 2020. [Online]. Available:

https://www.newenglandhistoricalsociety.com/percy-spencer-melts-chocolate-bar-invents-microwave-oven/. [Accessed 9 December 2020].

[11] P. L. Spencer, "Method of treating foodstuffs". US Patent 2495429, 24 January 1950.

[12] E. Brookner, "From $10,000 magee to $7 magee and $10 transmitter and receiver (T/R) on a single chip," in *2010 International Conference on the Origins and Evolution of the Cavity Magnetron (CAVMAG 2010)*, Bournemouth, United Kingdom, 2010.

[13] C. Spindt, K. Shoulders and L. Heynick, "Field emission cathode structures and devices utilizing such structures". US Patent 3755704, 28 August 1973.

[14] J. M. Dawson, "Pariticle Simulation of Plasmas," *Reviews of Modern Physics,* vol. 2, no. 55, pp. 403-447, 1983.

[15] S. A. Fernandez-Gutierrez, J. Browning, M. Lin, D. N. Smith and J. Watrous, "Phase-Control of a Rising Sun Magnetron Using a Modulated, Addressable, Current Source," *Journal of Vacuum Science & Technology,* vol. 33, 2015.

[16] S. A. Fernandez-Gutierres and et al., "Simulation of a Rising Sun Magnetron Employing a Faceted Cathode with a Continuous Current Source," *Journal of Vacuum Science & Technology B,* vol. 32, no. 6, 2014.

[17] S. A. Fernandez-Gutierrez, J. Browning, D. Smithe, M.-C. Lin and J. Watrous, "Simulation of a Facted Magnetron Using Discrete Modulated Current Sources," in *2014 IEEE 41st International Conference on Plasma Sciences (ICOPS)*, Washington D.C., 2014.

[18] "CWM-75KW; 75 kW L-Band CW Magnetron," L3Harris Electron Devices, Walliamsport, PA, 2020.

[19] M. Worthington and J. Cipolla, *Experimental Data of the L3Harris CWM-75kW.*

[20] C. Wolff, "Radar Basics - Magnetron," [Online]. Available: http://www.radartutorial.eu/08.transmitters/Magnetron.en.html. [Accessed 17 April 2019].

[21] "Neets- Naval Electrical Engineering Training Series," Integrated Publishing, Inc., [Online]. Available: http://electriciantraining.tpub.com/14183/css/The-Magnetron-Continued-113.htm. [Accessed 17 April 2019].

[22] D. M. Kirkwood, S. J. Gross, T. J. Balk, M. J. Beck, J. Booske, D. Busbaher, R. Jacobs, M. E. Kordesch, B. Mitsdarfffer, D. Morgan, W. D. Palmer, B. Vancil and J. E. Yater, "Frontiers in Thermionic Cathode Research," *IEEE Transactions on Electron Devices,* vol. 65, no. 6, pp. 2061-2071, 2018.

[23] K. U. Laszczyk, "Field Emission Cathodes to Form an Electron Beam," *Micromachines,* vol. 11, p. 260, 2020.

[24] O. W. Richardson, "The Emission of Electrons From Tungsten at High

Temperatures: An Experimental Proof That The Electric Current In Metals Is Carried By Electrons," *Science,* vol. 38, no. 967, pp. 57-61, 1913.

[25] R. H. Fowler and L. W. Nordheim, "Electron Emission in Intense Electric Fields," *Preceedings of the Royal Society A,* vol. 119, no. 781, pp. 173-181, 1928.

[26] A. J. Brizard, "Beyong Linear Gyrocenter Polarization in Gyrokinetic Theory," *Physics of Plasmas,* vol. 20, no. 9, 2013.

[27] J. Creedon, "Magnetric Cutoff in High-Current Diodes," *Journal of Applied Physics,* vol. 48, no. 3, pp. 1070-1077, 1977.

[28] R. V. Lovelace and T. F. T. Young, "Relativistic Hartree Condition for Magnetrons: Theory and Comparison with Experiments," *The Physics of Fluids,* vol. 28, no. 8, pp. 2450-2452, 1985.

[29] W. Knauer, "Diocotron Instability in Plasmas and Gas Discharges," *Journal of Applied Physics,* vol. 37, no. 2, pp. 602-611, 1965.

[30] R. H. Levy, "Diocotron Instability in a Cylindrical Geometry," *Physics of Fluids,* vol. 8, no. 7, 1965.

[31] H. S. Uhm, H. C. Chen and H. E. Brandt, "Theory of the Diocotron Instability in High Power Magnetron," in *Proceedings Volume 1039, 13th Intl Conf on Infrared and Millimeter Waves*, Honolulu, HI, United States, 1989.

[32] V. M. Ayres, H. C. Chen, R. A. Stark and H. S. Uhm, "Diocotron Instability for Relativistic Non-neutral Electron Flow in a Planar Magnetron Geometry," *Physics of Fluids B: Plasma Physics,* vol. 4, no. 10, 1992.

[33] L. Brillouin, "A Theorem of Larmor and Its Importance for Electrons in Magnetric Fields," *Physical Review,* vol. 67, no. 7, pp. 260-266, 1945.

[34] P. J. Christenson, D. P. Chernin, A. L. Garner and Y. Y. Lau, "Resistive Destabilization of Cycloidal Electron Flow and Universality of (near-)Brillouin Flow in a Crossed-field Gap," *Physics of Plasmas ,* vol. 3, no. 12, pp. 4455-4462, 1996.

[35] D. H. Simon, Y. Y. Lau, G. Greening, P. Wong, B. W. Hoff and R. M. Gilgenbach, "Stability of Brillouin Flow in Planar, Conventional, and Inverted Magnetrons," *Physics of Plasmas,* vol. 22, p. 082104, 2015.

[36] D. H. Simon, Y. Y. Lau, G. Greening, P. Wong, B. Hoff and R. M. Gilgenbach, "Stability of Brillouin Flow in the Presence of Slow-wave Structure," *Physics of Plasmas,* vol. 23, p. 092101, 2016.

[37] R. M. Gilgenbach and et al., "Recirculating Planar Magnetrons for High-Power High-Frequency Radiation Generation," *IEEE Transactions on Plasma Science,* vol. 39, no. 4, pp. 980-987, 2011.

[38] G. B. Greening, S. C. Exelby, D. A. Packard, N. M. Jordan, Y. Y. Lau and R. M. Gilgenbach, "Harmonic Frequency Locking in the Multifrequency Recirculating Planar Magnetron," *IEEE Transactions on Electron Devices,* vol. 65, no. 6, pp. 2347-2353, 2018.

[39] M. C. Jones and et al., "Cathode Priming of a Relativisitic Magnetron," *Applied Physics Letters,* vol. 85, no. 26, pp. 6332-6334, 2004.

[40] M. Fuks and E. Schammiloglu, "Rapid Start of Oscillations in a Magnetron with a "Transparent" Cathode," *Physical Review Letters,* vol. 95, no. 20, 2005.

[41] R. W. Lemke, T. C. Genoni and T. A. Spencer, "Three-Dimensiional Particle-in-cell Simulation Study of a Relativistic Magnetron," *Physcis of Plasmas,* vol. 6, no. 2, pp. 603-613, 1999.

[42] S. Prasad and et al., "Experimental Verification of the Advantages of the Transparent Cathode in a Short-pulse Magnetron," in *2009 IEEE Pulsed Power Conference*, Washington D.C., 2009.

[43] M. I. Fuks and E. Schamiloglu, "70% efficient relativistic magnetron with axial extraction of radiation through a horn antenna," *IEEE Transactions on Plasma Science,* vol. 18, no. 2, p. 023103, 2010.

[44] C. Leach, S. Prasad, M. Fuks, J. Buchenauer, W. McConaha and E. Schamiloglu, "Experimental Demonstration of a High-Efficiency Relativistic Magnetron With Diffraction Output With Spherical Cathode Endcap," *IEEE Transactions on Plasma Science,* vol. 45, no. 2, pp. 282-288, 2017.

[45] A. D. Andreev and K. J. Hendricks, "Particle-in-Cell (PIC) Simulation of CW Industrial Heating Magnetron," *Journal of Microwave Power and Electromagnetic Energy,* vol. 44, no. 2, pp. 114-124, 2010.

[46] A. D. Andreev and K. J. Hendricks, "ICEPIC Simulation of a Strapped Nonrelativistic High-power CW UHF Magnetron with a Solid Cathode Operating in the Space-charge Limited Regime," *IEEE Transactions on plasma science ,* vol. 40, no. 6, pp. 1551-1562, 2012.

[47] C. Nieter and J. R. Cary, "VORPAL: a versatile plasma simulation code," *Journal of Computational Physics,* vol. 196, no. 2, pp. 448-473, 2004.

[48] M. C. Lin, C. Nieter, P. H. Stoltz and D. Smithe, "Accurately and Efficiently Studying the RF Structures Using a Conformal Finite-Difference Time-Domain Particle-in-Cell Method," *The Open Plasma Physics Journal,* vol. 3, pp. 48-52, 2010.

[49] L. Li, K. Aranganadin, H. Y. Hsu and M. C. Lin, "Design and Development fo Field Emission Based Magnetron for Industrial Applicaitons Using Conformal Finite-Difference Time-domain Particle-In-Cell Simulations," *Journal of Vacuum Science & Technology B,* vol. 38, no. 2, p. 023205, 2020.

[50] S. Maurya, V. V. P. Singh and P. K. Jain, "Study of Output Performance of Partially Dielectric Loaded A6 Relativistic Magnetron," *IEEE Transactions on Plasma Science,* vol. 40, no. 4, pp. 1070-1074, 2012.

[51] H. J. Kim, U. S. Jung and J. C. Jin, "Particle-in-cell code simulations on a rising-sun magnetron oscillator," *IEEE Transactions on Plasma Science,,* vol. 30, no. 3, pp. 956-961, 2002.

[52] X. Chen, M. Esterson and P. A. Lindsay, "Computer modeling of phase locking in magnetrons," *Proc. SPIE Intense Microwave Pulses IV,* vol. 2843, no. 47, pp. 47-56, 19996.

[53] S. Maurya, V. V. P. Singh and P. K. Jain, "Three-Dimensional Particle-in-Cell Simulation of Fast Oscillation Startup and Efficiency Improvement in a Relativistic Magnetron With Electric Priming," *IEEE Transactions on Plasma Science,* vol. 40, no. 10, pp. 2686-2692, 2012.

[54] B. W. Hoff, M. Franzi, R. M. Gilgenbach and Y. Y. Lau, "Three-Dimensional Simulations of Magnetic Priming of a Relativistic Magnetron," *IEEE Transactions on Plasma Science,* vol. 38, no. 6, pp. 1292-1301, 2010.

[55] J. Bronwing and J. Watrous, "Faceted Magnetron Concept Using Field Emission Cathodes," *Journal of Vacuum Science and Technology B,* vol. 29, no. 2, p. 02B109, 2011.

[56] A. D. Andreev and K. J. Hendricks, "ICEPIC Simulation of a Strapped Nonrelativistic High-Power CW UHF Magnetron With a Solid Cathode Operating in the Space-Charge Limited Regime," *IEEE Transactions on Plasma Science,* vol. 40, no. 6, pp. 1551-1562, 2012.

[57] T. A. Van der Straaten, N. F. Cramer, I. S. Falconer and B. W. James, "The Cylindrical DC Magnetron Discharge: I. Particle-in-cell Simulation," *Journal of Physics D: Applied Physics,* vol. 31, no. 2, pp. 177-190, 1998.

[58] S. A. Guerrera and A. I. Akinwande, "Silicon Field Emitter Arrays with Current Densities Exceeding 100 A/cm2 at Gate Voltages Below 75 V," *IEEE Electron Device Letters,* vol. 37, no. 1, pp. 96-99, 2016.

[59] D. Black, R. Harper, P. Ward, J. Davlin, O. Bentancourt, D. Plumlee and J. Browning, "A Cathode Support Structure for Use in a Magnetron Oscillator Experiment," *International Journal of Applied Ceramic Technology,* vol. 17, no. 5, pp. 2393-2406, 2020.

[60] F. H. Harlow, "A Machine Calculation Method for Hydrodynamic Problems," Los Alamos Scientific Laboratory, Los Alamos, NM, 1955.

[61] J. M. Dawson, "Particle Simulation of Plasmas," *Reviews of Modern Physics,* vol. 55, no. 2, pp. 403-447, 1983.

[62] K. S. Yee, "Numerical Solution of Initial Boundary Value Problems Involving Maxwell's Equations in Isotropic Media," *IEEE Transactions on Antennas and Propagation,* vol. 14, no. 3, pp. 302-307, 1966.

[63] S. Dey and R. Mittra, "A Locally Conformal Finite-Difference Time-Domain (FDTD) Algorithm for Modeling Three-Dimensional Perfectly Conducting

Objects," *IEEE Microwave and Guided Wave Letters,* vol. 7, no. 9, pp. 273-275, 1997.

[64] R. Schuhmann, T. Weiland and I. A. Zagorodnov, "A Uniformaly Stable Conformal FDTD-method in Cartesian Grids," *International Journal of Numerical Modeling,* vol. 16, p. 127, 2003.

[65] C. K. Birdsall and A. B. Langdon, Plasma Physics Via Computer Simulation, McGraw-Hill, 1985.

[66] J. P. Boris, "Relativistic Plasma Simulation-Optimization of a Hybrid Code," in *Proceedings of the 4th Conference on Numerical Simulation of Plasmas*, Washington, D.C., 1970.

[67] H. Qin, S. Zhang, J. Xiao and W. M. Tang, "Why is the Boris Algorithm So Good?," *Physics of Plasmas,* vol. 20, no. 5, p. 084503, 2013.

[68] C. Nieter, J. R. Cary, G. R. Werner, D. Smithe and P. H. Stoltz, "Application of Dey-Mittra Conformal Boundary Algorithm to 3D Electromagnetic Modeling," *Journal of Computational Physics,* vol. 228, no. 21, pp. 7902-7916, 2009.

[69] R. Courant, K. Friedrichs and H. Lewy, "On the Partial Difference Equations of Mathematical Physics," *IBM Journal,* 1967.

[70] A. C. Cangellaris and D. B. Wright, "Analysis of the Numerical Error Caused by the Stair-stepped Approximation of a Conducting Boundary in FDTD Simulations of Electromagnetic Phenomena," *IEEE Transactions on Antennas and Propagation,* vol. 39, pp. 1518-1525, 1991.

[71] X.-K. Wei, W. Shao, S.-B. Shi, Y. Zhang and B.-Z. Wang, "An efficient locally one-dimensional finite-difference time-domain method based on the conformal scheme," *Chinese Physics B,* vol. 24, no. 7, p. 070203, 2015.

[72] I. A. Zagorodnov, R. Schuhmann and T. Weiland, "A uniformaly stable conformal FDTD-method in Cartesian grids," *International Journal of Numerical Modeling,* vol. 16, p. 127, 2003.

[73] C. Nieter, J. R. Cary, D. Smithe and P. H. Stoltz, "SIMULATIONS OF ELECTRON

EFFECTS IN SUPERCONDUCTING," in *Proceedings of EPAC 2006*, Edinburgh, Scotland, 2006.

[74] "VSim Reference Manual," Tech-X Corporation, Boulder, CO, 2020.

[75] W. M. White, R. M. Gilgenbach, M. C. Jones, V. B. Neculaes, Y. Y. Lau, P. Pengvanich, N. M. C. Jordan, B. W. Hoff, R. Edgar, T. A. Spencer and D. Price, "Radio frequency priming of a long-pulse relativistic magnetron," *IEEE Transactions on Plasma Science,* vol. 34, no. 3, pp. 627-634, 2006.

[76] B. W. Hoff, R. M. Gilgenbach, N. M. Jordan, Y. Y. Lau, E. J. Cruz, D. M. French, M. R. Gomez, J. C. Zier, T. A. Spencer and D. Price, "Magnetic Priming at the Cathode of a Relativistic Magnetron," *IEEE Transactions on Plasma Science,* vol. 36, no. 3, pp. 710-717, 2008.

[77] W. Fu, Y. Yan and X. Li, "Investigation of magnetron injection locking and cascaded locking by solid-state microwave power source," *Journal of Microwave Power and Electromagnetic Energy,* vol. 53, no. 3, pp. 171-183, 2019.

[78] G. Kazakevich, R. Johnson, V. Lebedev, V. Yakovlev and V. Pavlov, "Phase and Power Control in the RF Magnetron Power Stations of Superconducting Accelerators," *Physical Review Accelerators and Beams,* vol. 21, p. 062001, 2018.

[79] A. C. Dexter, G. Burt, R. G. Carter, I. Tahir, H. Wang, K. Davis and R. Rimmer, "First demonstration and performance of an injection locked continuous

wave magnetron," *Physcial Review Accdelerators and Beams,* vol. 14, p. 032001, 2011.

[80] C. D. Kirkpatrick and J. R. Dahlquist, Technical Analysis, Upper Saddle River, NJ: FT Press, 2010.

[81] Figure made with help from Dr. Ranajoy Bhattacharya.

[82] S. Fernandez-Gutierrez, *Simulation of A Magnetron Using Discrete Modulated Current Sources,* Ph.D. dissertation, Department of Electrical and Compter Engineering, Boise State University. Boise, 2014.

APPENDIX A

Data Sheet for the L3harris Cwm-75kw

CWM-75KW
75 KW L-BAND CW MAGNETRON

The CWM 75 kW is a fixed tuned magnetically focused, air and liquid-cooled, ceramic-metal magnetron designed for industrial processing applications. It can continuously generate 75 kW of useful power at 915 MHz with efficiencies approaching 90%.

KEY FEATURES

- 896, 915, 922, 929 MHz
- CW output power 75 kW
- 85% efficiency
- Air and liquid cooled

SPECIFICATIONS

PERFORMANCE CHARACTERISTICS

Frequency Range	896, 915, 922, 929 MHz
Power Output	75 kW
Anode voltage	19 kV
Anode Current	6.0 A
Efficiency	85 %
Filament Voltage	12.6 VAC
Filament Current	115 A
Max Load VSWR	1.5:1
Max Inlet Water Pressure	100 psi
Max Outlet Water Temp	70° C
Max Anode Dissipation	25 kW

TYPICAL OPERATING CONDITIONS

Frequency	915 MHz
CW Output Power	75 kW
Anode Voltage	18 kV
Anode Current	4.75 A
Efficiency	88 %
Filament Voltage	12.6 VAC
Filament Current (standby)	115 A
Filament Current (operating)	80 A
Electromagnet Current	4.0 A
Load VSWR	1.2:1
Anode Water Flow	5 gpm
Anode Cooling Temp	15 C
Cathode Air Flow	5 cfm
Dome Air Flow	40 cfm

MECHANICAL DESCRIPTION

Mounting Position	Any
Dimensions	See outline drawing
Terminal Connection	See outline drawing
Max Length	18.55 in
Max Diameter	4.94 in
Weight	15 lbs, 6.9 Kg

All voltages are with respect to cathode.

Electron Devices

CWM-75KW
75 KW L-BAND CW MAGNETRON

SEE OUTLINE

(measurements in inches)

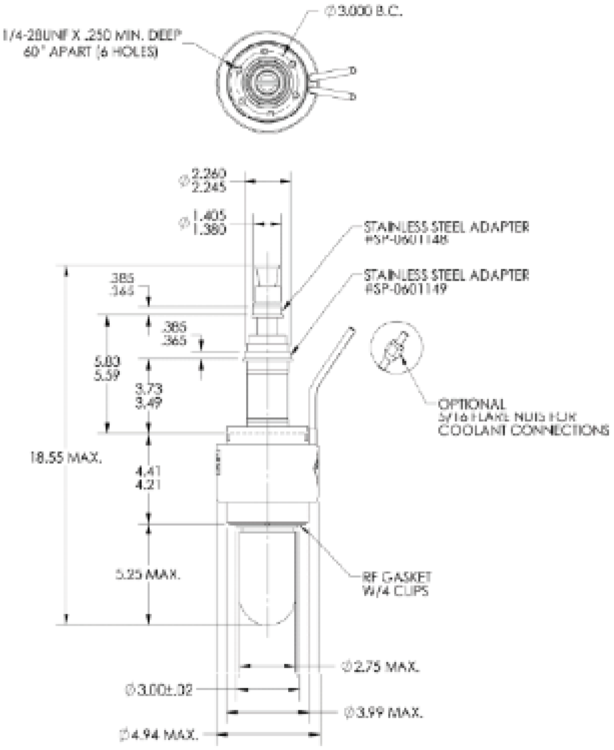

Please contact L3 Electron Devices for additional information, specific product requests, and/or requirements.

L3 Electron Devices
1035 Westminster Drive
Williamsport, PA 17701
570.326.3561
Toll free 888.861.1843
Fax: 570.326.2903
Email: EDD.Sales@L3T.com

Rev. Jan. 2017

APPENDIX B

Vsim Code Used for the 2d Rising Sun Magnetron Simulation

```
nsteps = 480000
dumpPeriodicity = 1000
dt = 1.0449320794148379e-12
dimension = 2
floattype = double
verbosity = 127
copyHistoryAtEachDump = 0
useGridBndryRestore = True
constructUniverse = False

<Grid globalGrid>
  verbosity = 127
  numCells = [102 102 12]
  lengths = [0.204 0.204 1.0]
  startPositions = [-0.102 -0.102 0.0]
</Grid>

<Decomp decomp>
  periodicDirs = []
</Decomp>

<GridBoundary theAnode>
  kind = rgnGridBndry
  dmFrac = 0.5
  calculateVolume = true

  <STRgn region>
    kind = stFuncRgn

    <STFunc function>
      kind = expression
      expression = (max(max((H(0.02242^2-((x))^2-((y))^2)-
0.4),(H(0.5*0.17453292519943295-
abs((mod(atan2((((y))),(((x))))+6.283185307179586+0.5*1.2566370614359172,1.25663
70614359172)-0.5*1.2566370614359172)))*H(((x))^2+((y))^2-0.02242^2)*H(0.1^2-
((x))^2-((y))^2)-0.4)),(H(0.5*0.17453292519943295-
abs((mod(atan2((((y))),(((x))))+6.283185307179586+1.0*1.2566370614359172,1.25663
70614359172)-0.5*1.2566370614359172)))*H(((x))^2+((y))^2-0.02242^2)*H(0.06^2-
((x))^2-((y))^2)-0.4)))
    </STFunc>

  </STRgn>

</GridBoundary>

<GridBoundary theCathode>
```

```
    kind = rgnGridBndry
    dmFrac = 0.5
    calculateVolume = true

    <STRgn region>
      kind = stFuncRgn

      <STFunc function>
        kind = expression
        expression = (1.0-(H(min(min(min(min(min(min(min(min(min(((((x))-(-
4.286263797015736e-18))*((-0.008090169943749477)-(-0.01))-(((y))-(-
0.01))*((0.005877852522924728)-(-4.286263797015736e-18)))*(((-
0.005877852522924723)-(-4.286263797015736e-18))*((-0.008090169943749477)-(-
0.01))-((-0.00809016994374948)-(-0.01))*((0.005877852522924728)-(-
4.286263797015736e-18))),((((x))-(0.005877852522924728))*((-
0.003090169943749479)-(-0.008090169943749477))-(((y))-(-
0.008090169943749477))*((0.009510565162951535)-(0.005877852522924728)))*(((-
4.286263797015736e-18)-(0.005877852522924728))*((-0.003090169943749479)-(-
0.008090169943749477))-((-0.01)-(-
0.008090169943749477))*((0.009510565162951535)-
(0.005877852522924728)))),((((x))-
(0.009510565162951535))*((0.0030901699437494694)-(-0.003090169943749479))-
(((y))-(-0.003090169943749479))*((0.009510565162951538)-
(0.009510565162951535)))*(((0.005877852522924728)-
(0.009510565162951535))*((0.0030901699437494694)-(-0.003090169943749479))-((-
0.008090169943749477)-(-0.003090169943749479))*((0.009510565162951538)-
(0.009510565162951535)))),((((x))-
(0.009510565162951538))*((0.008090169943749472)-(0.0030901699437494694))-
(((y))-(0.0030901699437494694))*((0.005877852522924736)-
(0.009510565162951538)))*(((0.009510565162951535)-
(0.009510565162951538))*((0.008090169943749472)-(0.0030901699437494694))-((-
0.003090169943749479)-(0.0030901699437494694))*((0.005877852522924736)-
(0.009510565162951538)))),((((x))-(0.005877852522924736))*((0.01)-
(0.008090169943749472))-(((y))-(0.008090169943749472))*((5.5109105961630896e-
18)-(0.005877852522924736)))*(((0.009510565162951538)-
(0.005877852522924736))*((0.01)-(0.008090169943749472))-
((0.0030901699437494694)-(0.008090169943749472))*((5.5109105961630896e-18)-
(0.005877852522924736)))),((((x))-(5.5109105961630896e-
18))*((0.008090169943749477)-(0.01))-(((y))-(0.01))*((-0.005877852522924727)-
(5.5109105961630896e-18)))*(((0.005877852522924736)-(5.5109105961630896e-
18))*((0.008090169943749477)-(0.01))-((0.008090169943749472)-(0.01))*((-
0.005877852522924727)-(5.5109105961630896e-18)))),((((x))-(-
0.005877852522924727))*((0.0030901699437494803)-(0.008090169943749477))-
(((y))-(0.008090169943749477))*((-0.009510565162951535)-(-
0.005877852522924727)))*(((5.5109105961630896e-18)-(-
0.005877852522924727))*((0.0030901699437494803)-(0.008090169943749477))-
```

```
((0.01)-(0.008090169943749477))*((-0.009510565162951535)-(-
0.005877852522924727)))),((((x))-(-0.009510565162951535))*((-
0.0030901699437494512)-(0.0030901699437494803))-(((y))-
(0.0030901699437494803))*((-0.009510565162951543)-(-
0.009510565162951535)))*(((-0.005877852522924727)-(-0.009510565162951535))*((-
0.0030901699437494512)-(0.0030901699437494803))-((0.008090169943749477)-
(0.0030901699437494803))*((-0.009510565162951543)-(-
0.009510565162951535)))),((((x))-(-0.009510565162951543))*((-
0.008090169943749 48)-(-0.0030901699437494512))-(((y))-(-
0.0030901699437494512))*((-0.005877852522924723)-(-
0.009510565162951543)))*(((-0.009510565162951535)-(-0.009510565162951543))*((-
0.00809016994374948)-(-0.0030901699437494512))-((0.0030901699437494803)-(-
0.0030901699437494512))*((-0.005877852522924723)-(-
0.009510565162951543)))),((((x))-(-0.005877852522924723))*((-0.01)-(-
0.00809016994374948))-(((y))-(-0.00809016994374948))*((-4.286263797015736e-18)-
(-0.005877852522924723)))*(((-0.009510565162951543)-(-
0.005877852522924723))*((-0.01)-(-0.00809016994374948))-((-
0.0030901699437494512)-(-0.00809016994374948))*((-4.286263797015736e-18)-(-
0.005877852522924723)))))))-0.4)
              </STFunc>

            </STRgn>
          </GridBoundary>

          <GridBoundary theMagnetron>
            kind = funcGridBndry
            dmFrac = 0.5
            calculateVolume = true

            <STFunc function>
              kind = expression
              expression = (min((1.0-(H(min(min(min(min(min(min(min(min(min((((((x)))-
(-4.286263797015736e-18))*((-0.008090169943749477)-(-0.01))-((((y)))-(-
0.01))*((0.005877852522924728)-(-4.286263797015736e-18)))*(((-
0.005877852522924723)-(-4.286263797015736e-18))*((-0.008090169943749477)-(-
0.01))-((-0.00809016994374948)-(-0.01))*((0.005877852522924728)-(-
4.286263797015736e-18))),(((((x)))-(0.005877852522924728))*((-
0.003090169943749479)-(-0.008090169943749477))-((((y)))-(-
0.008090169943749477))*((0.009510565162951535)-(0.005877852522924728)))*(((-
4.286263797015736e-18)-(0.005877852522924728))*((-0.003090169943749479)-(-
0.008090169943749477))-((-0.01)-(-
0.008090169943749477))*((0.009510565162951535)-
(0.005877852522924728)))),(((((x)))-
(0.009510565162951535))*((0.0030901699437494694)-(-0.003090169943749479))-
((((y)))-(-0.003090169943749479))*((0.009510565162951538)-
(0.009510565162951535)))*(((0.005877852522924728)-
```

```
(0.00951056516295153 5))*((0.0030901699437494694)-(-0.003090169943749479))-((-
0.008090169943749477)-(-0.003090169943749479))*((0.009510565162951538)-
(0.009510565162951535)))),(((((x)))-
(0.009510565162951538))*((0.008090169943749472)-(0.0030901699437494694))-
((((y)))-(0.0030901699437494694))*((0.005877852522924736)-
(0.009510565162951538)))*(((0.009510565162951535)-
(0.009510565162951538))*((0.008090169943749472)-(0.0030901699437494694))-((-
0.003090169943749479)-(0.0030901699437494694))*((0.005877852522924736)-
(0.009510565162951538)))),(((((x)))-(0.005877852522924736))*((0.01)-
(0.008090169943749472))-((((y)))-(0.008090169943749472))*((5.5109105961630896e-
18)-(0.005877852522924736)))*(((0.009510565162951538)-
(0.005877852522924736))*((0.01)-(0.008090169943749472))-
((0.0030901699437494694)-(0.008090169943749472))*((5.5109105961630896e-18)-
(0.005877852522924736)))),(((((x)))-(5.5109105961630896e-
18))*((0.008090169943749477)-(0.01))-((((y)))-(0.01))*((-0.005877852522924727)-
(5.5109105961630896e-18)))*(((0.005877852522924736)-(5.5109105961630896e-
18))*((0.008090169943749477)-(0.01))-((0.008090169943749472)-(0.01))*((-
0.005877852522924727)-(5.5109105961630896e-18)))),(((((x)))-(-
0.005877852522924727))*((0.0030901699437494803)-(0.008090169943749477))-
((((y)))-(0.008090169943749477))*((-0.009510565162951535)-(-
0.005877852522924727)))*(((5.5109105961630896e-18)-(-
0.005877852522924727))*((0.0030901699437494803)-(0.008090169943749477))-
((0.01)-(0.008090169943749477))*((-0.009510565162951535)-(-
0.005877852522924727)))),(((((x)))-(-0.009510565162951535))*((-
0.0030901699437494512)-(0.0030901699437494803))-((((y)))-
(0.0030901699437494803))*((-0.009510565162951543)-(-
0.009510565162951535)))*(((-0.005877852522924727)-(-0.009510565162951535))*((-
0.0030901699437494512)-(0.0030901699437494803))-((0.008090169943749477)-
(0.0030901699437494803))*((-0.009510565162951543)-(-
0.009510565162951535)))),(((((x)))-(-0.009510565162951543))*((-
0.00809016994374948)-(-0.0030901699437494512))-((((y)))-(-
0.0030901699437494512))*((-0.005877852522924723)-(-
0.009510565162951543)))*(((-0.009510565162951535)-(-0.009510565162951543))*((-
0.00809016994374948)-(-0.0030901699437494512))-((0.0030901699437494803)-(-
0.0030901699437494512))*((-0.005877852522924723)-(-
0.009510565162951543)))),(((((x)))-(-0.005877852522924723))*((-0.01)-(-
0.00809016994374948))-((((y)))-(-0.00809016994374948))*((-4.286263797015736e-
18)-(-0.005877852522924723)))*(((-0.009510565162951543)-(-
0.005877852522924723))*((-0.01)-(-0.00809016994374948))-((-
0.0030901699437494512)-(-0.00809016994374948))*((-4.286263797015736e-18)-(-
0.005877852522924723))))))-0.4),(max(max((H(0.02242^2-(((x)))^2-(((y)))^2)-
0.4),(H(0.5*0.17453292519943295-
abs((mod(atan2(((((y)))),((((x)))))+6.283185307179586+0.5*1.2566370614359172,1.256
6370614359172)-0.5*1.2566370614359172)))*H((((x)))^2+(((y)))^2-
0.02242^2)*H(0.1^2-(((x)))^2-(((y)))^2)-0.4)),(H(0.5*0.17453292519943295-
abs((mod(atan2(((((y)))),((((x)))))+6.283185307179586+1.0*1.2566370614359172,1.256
```

```
6370614359172)-0.5*1.2566370614359172)))*H((((x)))^2+(((y)))^2-
0.02242^2)*H(0.06^2-(((x)))^2-(((y)))^2)-0.4)))))
          </STFunc>

        </GridBoundary>

        <GridBoundary loadGeomSolid>
          kind = gridRgnBndry
          calculateVolume = 1
          dmFrac = 0.5
          polyfilename = loadGeom__loadGeomSolid.stl
          flipInterior = True
          scale = [1.0 1.0 1.0]
          printGridData = False
          mappedPolysfile = loadGeom__loadGeomSolid_mapped.stl
        </GridBoundary>

        <MultiField multiField>

          <Scalar historyfeedbackCurrentSourceComp1Scalar>
            kind = regular
            initialValue = 1.0
          </Scalar>

          <Scalar historyfeedbackCurrentSourceComp2Scalar>
            kind = regular
            initialValue = 1.0
          </Scalar>

          <Field myExternalBField>
            numComponents = 3
            overlap = [1 1]
            offset = none
            labels = [myExternalBField_x myExternalBField_y myExternalBField_z]

            <InitialCondition initmyExternalBField>
              kind = varset
              lowerBounds = [0 0]
              upperBounds = [103 103]
              components = [0 1 2]

              <STFunc component0>
                kind = expression
                expression = 0.0
              </STFunc>
```

```
    <STFunc component1>
      kind = expression
      expression = 0.0
    </STFunc>

    <STFunc component2>
      kind = expression
      expression = 0.12
    </STFunc>

  </InitialCondition>

  dumpSteps = [0]
</Field>

<Field J>
  numComponents = 3
  offset = edge
  kind = depField
  overlap = [1 2]
  labels = [J_x J_y J_z]
</Field>

<Field E>
  numComponents = 3
  offset = edge
  kind = regular
  overlap = [1 1]
  labels = [E_x E_y E_z]
</Field>

<Field B>
  numComponents = 3
  offset = face
  kind = regular
  overlap = [1 1]
  labels = [B_x B_y B_z]
</Field>

<Field nodalE>
  numComponents = 3
  offset = none
  kind = regular
  overlap = [1 2]
  labels = [nodalE_x nodalE_y nodalE_z]
</Field>
```

```
<Field nodalB>
 numComponents = 3
 offset = none
 kind = regular
 overlap = [1 2]
 labels = [nodalB_x nodalB_y nodalB_z]
</Field>

<Field D>
 numComponents = 3
 offset = edge
 kind = regular
 overlap = [1 1]
 labels = [D_x D_y D_z]
</Field>

<Field invEps>
 numComponents = 3
 offset = edge
 kind = regular
 overlap = [1 1]
 labels = [invEps_x invEps_y invEps_z]
 dumpSteps = [0]
</Field>

<Field lossFactor>
 numComponents = 3
 offset = edge
 kind = regular
 overlap = [1 1]
 labels = [lossFactor_x lossFactor_y lossFactor_z]
 dumpSteps = [0]
</Field>

<Updater historyfeedbackCurrentSourceComp1Scalarupdater>
 kind = unaryScalarOpUpdater
 operation = set
 writeScalars = [historyfeedbackCurrentSourceComp1Scalar]
 dtCoefficients = [1.0 0.0]

 <STFunc convert>
  kind = historyAsSTFunc
  history = cathodeAnodeVoltage
  expression = 1.0
 </STFunc>
```

```
</Updater>

<Updater historyfeedbackCurrentSourceComp2Scalarupdater>
  kind = unaryScalarOpUpdater
  operation = set
  writeScalars = [historyfeedbackCurrentSourceComp2Scalar]
  dtCoefficients = [1.0 0.0]

  <STFunc convert>
    kind = historyAsSTFunc
    history = cathodeAnodeVoltage
    expression = 1.0
  </STFunc>

</Updater>

<FieldUpdater myExternalBFieldaddingUpdater>
  kind = fieldBinOpUpdater
  binOp = add
  lowerBounds = [0 0 0]
  upperBounds = [103 103 13]
  aCoeff = 1.0
  bCoeff = 1.0
  readFields = [myExternalBField nodalB]
  writeFields = [nodalB]
</FieldUpdater>

<FieldUpdater constantVoltageDrain0>
  kind = STFuncUpdater
  operation = add
  lowerBounds = [0 0 0]
  upperBounds = [102 102 0]
  component = 0
  writeFields = [J]
  writeComponents = 0

  <STFunc stFunc>
    kind = expression
    expression = (-1.0*(1.0-exp(-1.0*max(0.0,(t))/1e-
09))*(1791.555388913859/6.283185307179586)*((atan2((x),(y)-0.5*(0.002))-
atan2((x),(y)+0.5*(0.002)))/(0.002)))
  </STFunc>

</FieldUpdater>
```

```
        <FieldUpdater constantVoltageDrain1>
          kind = STFuncUpdater
          operation = add
          lowerBounds = [0 0 0]
          upperBounds = [102 102 0]
          component = 1
          writeFields = [J]
          writeComponents = 1

          <STFunc stFunc>
            kind = expression
            expression = (-1.0*(1.0-exp(-1.0*max(0.0,(t))/1e-
09))*(1791.555388913859/6.283185307179586)*((atan2((y),(x)-0.5*(0.002))-
atan2((y),(x)+0.5*(0.002)))/(0.002)))
          </STFunc>

        </FieldUpdater>

        <FieldUpdater feedbackVoltageSource0>
          kind = STFuncUpdater
          operation = add
          lowerBounds = [0 0 0]
          upperBounds = [102 102 0]
          component = 0
          writeFields = [J]
          writeComponents = 0

          <STFunc stFunc>
            kind = feedbackSTFunc
            expression = (1791.555388913859/6.283185307179586)*((atan2((x),(y)-
0.5*(0.002))-atan2((x),(y)+0.5*(0.002)))/(0.002))
            feedback = feedbackCurrentSourceComp1cathodeAnodeVoltageFeedback
          </STFunc>

        </FieldUpdater>

        <FieldUpdater feedbackVoltageSource1>
          kind = STFuncUpdater
          operation = add
          lowerBounds = [0 0 0]
          upperBounds = [102 102 0]
          component = 1
          writeFields = [J]
          writeComponents = 1

          <STFunc stFunc>
```

```
          kind = feedbackSTFunc
          expression = (1791.555388913859/6.283185307179586)*((atan2((y),(x)-
0.5*(0.002))-atan2((y),(x)+0.5*(0.002)))/(0.002))
          feedback = feedbackCurrentSourceComp2cathodeAnodeVoltageFeedback
        </STFunc>

      </FieldUpdater>

      <FieldUpdater setInvEps>
        kind = multiDielectricUpdater
        lowerBounds = [0 0 0]
        upperBounds = [103 103 13]
        permittivityField = invEps

        <DielectricShape loadGeomSolidShape>
          boundary = loadGeomSolid
          permittivity = 1.0
        </DielectricShape>

        backgroundPermittivity = 1.0
      </FieldUpdater>

      <FieldUpdater DtoE>
        kind = fieldBinOpUpdater
        binOp = multiply
        lowerBounds = [0 0 0]
        upperBounds = [103 103 13]
        aCoeff = 0.0
        bCoeff = 0.0
        readFields = [D invEps]
        writeFields = [E]
      </FieldUpdater>

      <FieldUpdater setLossFactor>
        kind = multiDielectricUpdater
        lowerBounds = [0 0 0]
        upperBounds = [103 103 13]
        permittivityField = lossFactor

        <DielectricShape loadGeomSolidShape>
          boundary = loadGeomSolid
          permittivity = 1.0002310387975053
        </DielectricShape>

        backgroundPermittivity = 1.0
      </FieldUpdater>
```

```
<FieldUpdater beforeAmpereLossA>
  kind = fieldBinOpUpdater
  binOp = divide
  lowerBounds = [0 0 0]
  upperBounds = [103 103 13]
  aCoeff = 0.0
  bCoeff = 0.0
  readFields = [D lossFactor]
  writeFields = [E]
</FieldUpdater>

<FieldUpdater beforeAmpereLossB>
  kind = fieldBinOpUpdater
  binOp = subtract
  lowerBounds = [0 0 0]
  upperBounds = [103 103 13]
  aCoeff = 2.0
  bCoeff = 1.0
  readFields = [D E]
  writeFields = [D]
</FieldUpdater>

<FieldUpdater afterAmpereLoss>
  kind = fieldBinOpUpdater
  binOp = multiply
  lowerBounds = [0 0 0]
  upperBounds = [103 103 13]
  aCoeff = 0.0
  bCoeff = 0.0
  readFields = [D lossFactor]
  writeFields = [D]
</FieldUpdater>

<FieldMultiUpdater yeeAmpere>
  kind = yeeAmpereUpdater
  readFieldCompShifts = [0 0]
  components = [0 1 2]
  contractFromBottomInNonComponentDir = True
  gridBoundary = theMagnetron
  interiorness = deymittra
  readFields = [B J]
  writeFields = [D]
  lowerBounds = [0 0 0]
  upperBounds = [102 102 12]
</FieldMultiUpdater>
```

```
<FieldMultiUpdater yeeFaraday>
  kind = yeeFaradayUpdater
  gridBoundary = theMagnetron
  interiorness = deymittra
  components = [0 1 2]
  expandToTopInComponentDir = 1
  lowerBounds = [0 0 0]
  upperBounds = [102 102 12]
  readFields = [E]
  writeFields = [B]
</FieldMultiUpdater>

<FieldUpdater yeeDeyMittra>
  gridBoundary = theMagnetron
  interiorness = deymittra
  kind = deyMittraUpdater
  lowerBounds = [0 0 0]
  upperBounds = [102 102 12]
  readFields = [E]
  writeFields = [B]
</FieldUpdater>

<FieldUpdater edgeToNode>
  kind = edgeToNodeVec
  lowerBounds = [0 0 0]
  upperBounds = [103 103 13]
  readFields = [E]
  writeFields = [nodalE]
</FieldUpdater>

<FieldUpdater copyPerimlowerX>
  kind = unaryFieldOpUpdater
  minDim = 1
  lowerBounds = [0 0 0]
  upperBounds = [1 103 13]
  operation = set
  bumpReadIter = [0 0 0]
  readFields = [E]
  component = 0
  writeFields = [nodalE]

  <STFunc copyFunc>
    kind = constantFunc
    amplitude = 1.
  </STFunc>
```

```
</FieldUpdater>

<FieldUpdater copyPerimupperX>
  kind = unaryFieldOpUpdater
  minDim = 1
  lowerBounds = [102 0 0]
  upperBounds = [103 103 13]
  operation = set
  bumpReadIter = [-1 0 0]
  readFields = [E]
  component = 0
  writeFields = [nodalE]

  <STFunc copyFunc>
    kind = constantFunc
    amplitude = 1.
  </STFunc>

</FieldUpdater>

<FieldUpdater copyPerimlowerY>
  kind = unaryFieldOpUpdater
  minDim = 2
  lowerBounds = [0 0 0]
  upperBounds = [103 1 13]
  operation = set
  bumpReadIter = [0 0 0]
  readFields = [E]
  component = 1
  writeFields = [nodalE]

  <STFunc copyFunc>
    kind = constantFunc
    amplitude = 1.
  </STFunc>

</FieldUpdater>

<FieldUpdater copyPerimupperY>
  kind = unaryFieldOpUpdater
  minDim = 2
  lowerBounds = [0 102 0]
  upperBounds = [103 103 13]
  operation = set
  bumpReadIter = [0 -1 0]
```

```
   readFields = [E]
   component = 1
   writeFields = [nodalE]

   <STFunc copyFunc>
     kind = constantFunc
     amplitude = 1.
   </STFunc>

 </FieldUpdater>

 <FieldUpdater faceToNode>
   kind = faceToNodeVec
   lowerBounds = [0 0 0]
   upperBounds = [103 103 13]
   readFields = [B]
   writeFields = [nodalB]
 </FieldUpdater>

 <InitialUpdateStep myExternalBFieldaddingUpdaterInitStep>
   alsoAfterRestore = False
   updaters = [myExternalBFieldaddingUpdater]
   messageFields = [nodalB]
 </InitialUpdateStep>

 <InitialUpdateStep setInvEpsInitStep>
   alsoAfterRestore = True
   updaters = [setInvEps]
   messageFields = [invEps]
 </InitialUpdateStep>

 <InitialUpdateStep setDampFactInitStep>
   alsoAfterRestore = True
   updaters = [setLossFactor]
   messageFields = [lossFactor]
 </InitialUpdateStep>

 <UpdateStep historyfeedbackCurrentSourceComp1ScalarupdaterStep>
   toDtFrac = 1.0
   updaters = [historyfeedbackCurrentSourceComp1Scalarupdater]
   messageScalars = [historyfeedbackCurrentSourceComp1Scalar]
 </UpdateStep>

 <UpdateStep historyfeedbackCurrentSourceComp2ScalarupdaterStep>
   toDtFrac = 1.0
   updaters = [historyfeedbackCurrentSourceComp2Scalarupdater]
```

```
  messageScalars = [historyfeedbackCurrentSourceComp2Scalar]
</UpdateStep>

<UpdateStep myExternalBFieldaddingUpdaterStep>
  toDtFrac = 1.0
  updaters = [myExternalBFieldaddingUpdater]
  messageFields = [nodalB]
</UpdateStep>

<UpdateStep constantVoltageDrain0driveJStep>
  toDtFrac = 1.0
  updaters = [constantVoltageDrain0]
  messageFields = []
</UpdateStep>

<UpdateStep constantVoltageDrain1driveJStep>
  toDtFrac = 1.0
  updaters = [constantVoltageDrain1]
  messageFields = []
</UpdateStep>

<UpdateStep feedbackVoltageSource0driveJStep>
  toDtFrac = 1.0
  updaters = [feedbackVoltageSource0]
  messageFields = []
</UpdateStep>

<UpdateStep feedbackVoltageSource1driveJStep>
  toDtFrac = 1.0
  updaters = [feedbackVoltageSource1]
  messageFields = []
</UpdateStep>

<UpdateStep DtoEStep>
  toDtFrac = 1.0
  updaters = [DtoE]
  messageFields = [E]
</UpdateStep>

<UpdateStep beforeAmpereLossAStep>
  toDtFrac = 1.0
  updaters = [beforeAmpereLossA]
  messageFields = [E]
</UpdateStep>

<UpdateStep beforeAmpereLossBStep>
```

```
  toDtFrac = 1.0
  updaters = [beforeAmpereLossB]
  messageFields = [D]
</UpdateStep>

<UpdateStep afterAmpereLossStep>
  toDtFrac = 1.0
  updaters = [afterAmpereLoss]
  messageFields = [D]
</UpdateStep>

<UpdateStep ampereStep>
  toDtFrac = 1.0
  updaters = [yeeAmpere]
  messageFields = [D]
</UpdateStep>

<UpdateStep firstFaradayStep>
  toDtFrac = 0.5
  updaters = [yeeFaraday yeeDeyMittra]
  messageFields = [B]
</UpdateStep>

<UpdateStep secondFaradayStep>
  toDtFrac = 1.0
  updaters = [yeeFaraday yeeDeyMittra]
  messageFields = [B]
</UpdateStep>

<UpdateStep edgeToNodeStep>
  toDtFrac = 1.0
  updaters = [edgeToNode]
  messageFields = [nodalE]
</UpdateStep>

<UpdateStep copyPerimlowerXStep>
  toDtFrac = 1.0
  updaters = [copyPerimlowerX]
  messageFields = [nodalE]
</UpdateStep>

<UpdateStep copyPerimupperXStep>
  toDtFrac = 1.0
  updaters = [copyPerimupperX]
  messageFields = [nodalE]
</UpdateStep>
```

```
       <UpdateStep copyPerimlowerYStep>
        toDtFrac = 1.0
        updaters = [copyPerimlowerY]
        messageFields = [nodalE]
       </UpdateStep>

       <UpdateStep copyPerimupperYStep>
        toDtFrac = 1.0
        updaters = [copyPerimupperY]
        messageFields = [nodalE]
       </UpdateStep>

       <UpdateStep faceToNodeStep>
        toDtFrac = 1.0
        updaters = [faceToNode]
        messageFields = [nodalB]
       </UpdateStep>

       updateStepOrder = [firstFaradayStep constantVoltageDrain0driveJStep
constantVoltageDrain1driveJStep feedbackVoltageSource0driveJStep
feedbackVoltageSource1driveJStep beforeAmpereLossAStep beforeAmpereLossBStep
ampereStep afterAmpereLossStep DtoEStep secondFaradayStep
historyfeedbackCurrentSourceComp1ScalarupdaterStep
historyfeedbackCurrentSourceComp2ScalarupdaterStep edgeToNodeStep
copyPerimlowerXStep copyPerimupperXStep copyPerimlowerYStep
copyPerimupperYStep faceToNodeStep myExternalBFieldaddingUpdaterStep]
      </MultiField>

      <VectorDepositor JDep>
       kind = areaWeighting
       depField = multiField.J
      </VectorDepositor>

      <Species electron>
       kind = relBorisVW
       charge = -1.6021766208e-19
       mass = 9.10938215e-31
       nominalDensity = 149708931.98808953
       nomPtclsPerCell = 500.0
       numPtclsInMacro = 1.0e5
       fields = [multiField.nodalE multiField.nodalB]
       currDeps = [JDep]

       <ParticleSource cutCellEmitter>
        kind = xvLoaderEmitter
```

```
      applyTimes = [1e-09 1.0]
      load = False
      loadAfterInit = False
      loadOnShift = False
      emit = True
      emitBasedOnLocalForce = 1
      useCornerMove = 1

      <VelocityGenerator emitVelGen>
        kind = funcVelGen
        velocityIsLocal = True

        <STFunc component0>
          kind = expression
          expression = 150000.0
        </STFunc>

      </VelocityGenerator>

      <STFunc currentDensityFunc>
        kind = expression
        expression = 63661.97723675813
      </STFunc>

      <STFunc relMacroFluxFunc>
        kind = expression
        expression =
((max(ceil(max(0.8535533905932737,(0.5*(sin((5)*atan2((y),(x))+2*3.14159265358979
3*957000000.0*(t)+(3.141592653589793/2))+1)))-0.8535533905932737),0)))
      </STFunc>

      <PositionGenerator posGen>
        kind = cutCellPosGen
        emitterBoundary = theCathode
        emissionOffset = 0.1
        nomMacroPtclsPerStep = 500.0
      </PositionGenerator>

    </ParticleSource>

    <ParticleSink lower0Absorber>
      kind = absorber
      minDim = 1
      lowerBounds = [-1 -1 -1]
      upperBounds = [0 103 13]
    </ParticleSink>
```

```
  <ParticleSink upper0Absorber>
    kind = absorber
    minDim = 1
    lowerBounds = [102 -1 -1]
    upperBounds = [103 103 13]
  </ParticleSink>

  <ParticleSink lower1Absorber>
    kind = absorber
    minDim = 2
    lowerBounds = [0 -1 -1]
    upperBounds = [102 0 13]
  </ParticleSink>

  <ParticleSink upper1Absorber>
    kind = absorber
    minDim = 2
    lowerBounds = [0 102 -1]
    upperBounds = [102 103 13]
  </ParticleSink>

  <ParticleSink cathodeElectronSink>
    kind = absSavTriCutCell
    minDim = 1
    gridBoundary = theCathode
    lowerBounds = [-1 -1 -1]
    upperBounds = [103 103 13]
  </ParticleSink>

  <ParticleSink anodeElectronSink>
    kind = absSavTriCutCell
    minDim = 1
    gridBoundary = theAnode
    lowerBounds = [-1 -1 -1]
    upperBounds = [103 103 13]
  </ParticleSink>

</Species>

<History feedbackCurrentSourceComp1cathodeAnodeVoltageFeedback>
  kind = feedbackDesired
  scalar = multiField.historyfeedbackCurrentSourceComp1Scalar
  useMeasuredOnly = 0
  timeConstant = 1e-09
```

```
  <STFunc desiredHistory>
    kind = expression
    expression = 26000.0*(1.0-exp(-1.0*max(0.0,(t))/1e-09))
  </STFunc>

</History>

<History feedbackCurrentSourceComp2cathodeAnodeVoltageFeedback>
  kind = feedbackDesired
  scalar = multiField.historyfeedbackCurrentSourceComp2Scalar
  useMeasuredOnly = 0
  timeConstant = 1e-09

  <STFunc desiredHistory>
    kind = expression
    expression = 26000.0*(1.0-exp(-1.0*max(0.0,(t))/1e-09))
  </STFunc>

</History>

<History fieldEnergy_Joules>
  kind = EMfieldEnergy
  fields = [multiField.E multiField.B]
</History>

<History Anode_Current>
  kind = speciesCurrAbs
  species = [electron]
  ptclAbsorbers = [anodeElectronSink]
</History>

<History Cathode_Current>
  kind = speciesCurrAbs
  species = [electron]
  ptclAbsorbers = [cathodeElectronSink]
</History>

<History anodeElectronHeat_Watts_timesDT>
  kind = speciesEngyAbs
  species = [electron]
  ptclAbsorbers = [anodeElectronSink]
</History>

<History cathodeElectronHeat_Watts_timesDT>
  kind = speciesEngyAbs
  species = [electron]
```

```
  ptclAbsorbers = [cathodeElectronSink]
</History>

<History numMacroParticles>
  kind = speciesNumberOf
  species = [electron]
</History>

<History Cavity_Voltage>
  kind = pseudoPotential
  field = multiField.E
  referencePoint = [64 49 0]
  measurePoint = [64 53 0]
</History>

<History cathodeAnodeVoltage>
  kind = pseudoPotential
  field = multiField.E
  referencePoint = [51 51 0]
  measurePoint = [102 51 0]
</History>

<History Power_Out>
  kind = fieldPoyn
  lowerBounds = [81 45 0]
  upperBounds = [81 58 0]
  fields = [multiField.E multiField.B]
</History>

<History cavity1BField_Tesla>
  kind = fieldAtCoords
  field = multiField.B
  position = [0.1 0.0 0.0]
</History>

<History Emitted_Current>
  kind = speciesCurrEmit
  species = [electron]
  ptclSource = electron.cutCellEmitter
  sourceType = 0
</History>

<History Physical_Particle_Count>
  kind = speciesNumPhysical
  species = [electron]
</History>
```

APPENDIX C

Vsim Code Used for The L3harris Cwm-75kw Magnetron Simulation

```
nsteps = 454000
dumpPeriodicity = 2000
dt = 5.50660793e-13
dimension = 3
floattype = double
verbosity = 127
copyHistoryAtEachDump = 0
useGridBndryRestore = False
constructUniverse = False

<Grid globalGrid>
  verbosity = 127
  numCells = [220  220  127]
  lengths = [0.11 0.11 0.127]
  startPositions = [-0.055 -0.055 -0.055]
</Grid>

<Decomp decomp>
  periodicDirs = []
</Decomp>

<EmMaterial PEC>
  kind = conductor
  resistance = 0.0
</EmMaterial>

<GridBoundary vsimPecShapes>
  kind = gridRgnBndry
  calculateVolume = 1
  dmFrac = 0.5
  polyfilename = vsimPecShapes.stl
  flipInterior = True
  scale = [1.0  1.0  1.0]
  printGridData = False
  mappedPolysfile = vsimPecShapes_mapped.stl
</GridBoundary>

<GridBoundary anodeGeomSolid>
  kind = gridRgnBndry
  calculateVolume = 1
  dmFrac = 0.5
  polyfilename = anodeGeom__anodeGeomSolid.stl
  flipInterior = True
  scale = [1.0  1.0  1.0]
  printGridData = False
  mappedPolysfile = anodeGeom__anodeGeomSolid_mapped.stl
```

```
</GridBoundary>

<GridBoundary CathodeGeomSolid>
  kind = gridRgnBndry
  calculateVolume = 1
  dmFrac = 0.5
  polyfilename = CathodeGeom__CathodeGeomSolid.stl
  flipInterior = True
  scale = [1.0  1.0  1.0]
  printGridData = False
  mappedPolysfile = CathodeGeom__CathodeGeomSolid_mapped.stl
</GridBoundary>

<GridBoundary Cathde_largeGeomSolid>
  kind = gridRgnBndry
  calculateVolume = 1
  dmFrac = 0.5
  polyfilename = Cathde_largeGeom__Cathde_largeGeomSolid.stl
  flipInterior = True
  scale = [1.0  1.0  1.0]
  printGridData = False
  mappedPolysfile = Cathde_largeGeom__Cathde_largeGeomSolid_mapped.stl
</GridBoundary>

<MultiField multiField>

  <Scalar historydc_source_0Scalar>
    kind = regular
    initialValue = 1.0
  </Scalar>

  <Scalar historydc_source_1Scalar>
    kind = regular
    initialValue = 1.0
  </Scalar>

  <Field Applied_B>
    numComponents = 3
    overlap = [1 1]
    offset = none
    labels = [Applied_B_x   Applied_B_y   Applied_B_z]

    <InitialCondition initApplied_B>
      kind = varset
      lowerBounds = [0  0  0]
      upperBounds = [221  221  128]
```

```
    components = [0 1 2]

    <STFunc component0>
      kind = expression
      expression = 0.0
    </STFunc>

    <STFunc component1>
      kind = expression
      expression = 0.0
    </STFunc>

    <STFunc component2>
      kind = expression
      expression = -0.17
    </STFunc>

  </InitialCondition>

  dumpSteps = [0]
</Field>

<Field E>
  numComponents = 3
  offset = edge
  kind = regular
  overlap = [1 1]
  labels = [E_x   E_y   E_z]
</Field>

<Field B>
  numComponents = 3
  offset = face
  kind = regular
  overlap = [1 1]
  labels = [B_x   B_y   B_z]
</Field>

<Field J>
  numComponents = 3
  offset = edge
  kind = depField
  overlap = [1 2]
  labels = [J_x   J_y   J_z]
</Field>
```

```
<Field nodalE>
  numComponents = 3
  offset = none
  kind = regular
  overlap = [1 2]
  labels = [nodalE_x   nodalE_y   nodalE_z]
  dumpSteps = [0]
</Field>

<Field nodalB>
  numComponents = 3
  offset = none
  kind = regular
  overlap = [1 2]
  labels = [nodalB_x   nodalB_y   nodalB_z]
  dumpSteps = [0]
</Field>

<Updater historydc_source_0Scalarupdater>
  kind = unaryScalarOpUpdater
  operation = set
  writeScalars = [historydc_source_0Scalar]
  dtCoefficients = [1.0 0.0]

  <STFunc convert>
    kind=historyAsSTFunc
    history=Cathode_Anode_Voltage_Bottom
    expression=1.0
  </STFunc>

</Updater>

<Updater historydc_source_1Scalarupdater>
  kind = unaryScalarOpUpdater
  operation = set
  writeScalars = [historydc_source_1Scalar]
  dtCoefficients = [1.0 0.0]

  <STFunc convert>
    kind=historyAsSTFunc
    history=Cathode_Anode_Voltage_Bottom
    expression=1.0
  </STFunc>

</Updater>
```

```
<FieldUpdater Applied_BaddingUpdater>
 kind = fieldBinOpUpdater
 binOp = add
 lowerBounds = [0  0  0]
 upperBounds = [221  221  128]
 aCoeff = 1.0
 bCoeff = 1.0
 readFields = [Applied_B nodalB]
 writeFields = [nodalB]
</FieldUpdater>

<FieldUpdater portBeforeAmpereLower20>
 kind = userFuncUpdater
 minDim =  3
 lowerBounds = [0  0  0]
 upperBounds = [220  221  1]
 readFields = [E   E]
 readComponents = [0   0]
 readItersShiftInX = [0  0]
 readItersShiftInY = [0  0]
 readItersShiftInZ = [0  1]
 readFieldVarNames = [ESURFACE   EINSIDE]
 writeFields = [E]
 writeComponents = [0]

 <Expression updateFunction>
   expression = 0.7166144941210074*ESURFACE+EINSIDE
 </Expression>

</FieldUpdater>

<FieldUpdater portBeforeAmpereLower21>
 kind = userFuncUpdater
 minDim =  3
 lowerBounds = [0  0  0]
 upperBounds = [221  220  1]
 readFields = [E   E]
 readComponents = [1   1]
 readItersShiftInX = [0  0]
 readItersShiftInY = [0  0]
 readItersShiftInZ = [0  1]
 readFieldVarNames = [ESURFACE   EINSIDE]
 writeFields = [E]
 writeComponents = [1]

 <Expression updateFunction>
```

```
            expression = 0.7166144941210074*ESURFACE+EINSIDE
          </Expression>

        </FieldUpdater>

        <FieldUpdater portIncidentLower20>
          kind = STFuncUpdater
          minDim =  3
          operation = add
          lowerBounds = [0  0  0]
          upperBounds = [220  221  1]
          readFields = [E]
          component = 0
          writeFields = [E]
          writeComponents = [0]

          <STFunc function>
            kind = feedbackSTFunc
            feedback=dc_source_0Cathode_Anode_Voltage_BottomFeedback
            expression = 3.4332289882420146*(((0.625*-
2431980.5441556475*(H(0.012687**2+(((x)))**2+(((y)))**2)*H(0.019266**2-
(((x)))**2-(((y)))**2))*(sin(1.5707963267948966*max(0.0,min(1.0,(((t+5.50660793e-
13-1.6678204759907604e-12)))/(1e-08))))**2)*(1-(--
2431980.5441556475*(H(0.012687**2+((((x))))**2+((((y))))**2)*H(0.019266**2-
((((x))))**2-((((y))))**2))/1e-08/60.0*(((t+5.50660793e-13-1.6678204759907604e-
12))))/-2431980.5441556475))*((atan2(((x)),((y))-0.5*(0.0005))-
atan2(((x)),((y))+0.5*(0.0005)))/(0.0005)))-((0.625*-
2431980.5441556475*(H(0.012687**2+(((x)))**2+(((y)))**2)*H(0.019266**2-
(((x)))**2-(((y)))**2))*(sin(1.5707963267948966*max(0.0,min(1.0,(((t-
1.6678204759907604e-12)))/(1e-08))))**2)*(1-(--
2431980.5441556475*(H(0.012687**2+((((x))))**2+((((y))))**2)*H(0.019266**2-
((((x))))**2-((((y))))**2))/1e-08/60.0*(((t-1.6678204759907604e-12))))/-
2431980.5441556475))*((atan2(((x)),((y))-0.5*(0.0005))-
atan2(((x)),((y))+0.5*(0.0005)))/(0.0005))))
          </STFunc>

        </FieldUpdater>

        <FieldUpdater portIncidentLower21>
          kind = STFuncUpdater
          minDim =  3
          operation = add
          lowerBounds = [0  0  0]
          upperBounds = [221  220  1]
          readFields = [E]
          component = 1
```

```
          writeFields = [E]
          writeComponents = [1]

          <STFunc function>
            kind = feedbackSTFunc
            feedback=dc_source_0Cathode_Anode_Voltage_BottomFeedback
            expression = 3.4332289882420146*(((0.625*-
2431980.5441556475*(H(0.012687**2+(((x)))**2+(((y)))**2)*H(0.019266**2-
(((x)))**2-(((y)))**2))*(sin(1.5707963267948966*max(0.0,min(1.0,(((t+5.50660793e-
13-1.6678204759907604e-12)))/(1e-08))))**2)*(1-(--
2431980.5441556475*(H(0.012687**2+((((x))))**2+((((y))))**2)*H(0.019266**2-
((((x))))**2-((((y))))**2))/1e-08/60.0*(((t+5.50660793e-13-1.6678204759907604e-
12))))/-2431980.5441556475))*((atan2(((y)),((x))-0.5*(0.0005))-
atan2(((y)),((x))+0.5*(0.0005)))/(0.0005)))-((0.625*-
2431980.5441556475*(H(0.012687**2+(((x)))**2+(((y)))**2)*H(0.019266**2-
(((x)))**2-(((y)))**2))*(sin(1.5707963267948966*max(0.0,min(1.0,(((t-
1.6678204759907604e-12)))/(1e-08))))**2)*(1-(--
2431980.5441556475*(H(0.012687**2+((((x))))**2+((((y))))**2)*H(0.019266**2-
((((x))))**2-((((y))))**2))/1e-08/60.0*(((t-1.6678204759907604e-12))))/-
2431980.5441556475))*((atan2(((y)),((x))-0.5*(0.0005))-
atan2(((y)),((x))+0.5*(0.0005)))/(0.0005))))
          </STFunc>

        </FieldUpdater>

        <FieldUpdater portAfterAmpereLower21>
          kind = userFuncUpdater
          minDim =  3
          lowerBounds = [0  0  0]
          upperBounds = [221  220  1]
          readFields = [E   E]
          readComponents = [1   1]
          readItersShiftInX = [0  0]
          readItersShiftInY = [0  0]
          readItersShiftInZ = [0  1]
          readFieldVarNames = [ESURFACE   EINSIDE]
          writeFields = [E]
          writeComponents = [1]

          <Expression updateFunction>
            expression = ESURFACE-0.7166144941210074*EINSIDE
          </Expression>

        </FieldUpdater>

        <FieldUpdater portAfterAmpereLower20>
```

```
  kind = userFuncUpdater
  minDim =  3
  lowerBounds = [0  0  0]
  upperBounds = [220  221  1]
  readFields = [E   E]
  readComponents = [0   0]
  readItersShiftInX = [0  0]
  readItersShiftInY = [0  0]
  readItersShiftInZ = [0  1]
  readFieldVarNames = [ESURFACE   EINSIDE]
  writeFields = [E]
  writeComponents = [0]

  <Expression updateFunction>
    expression = ESURFACE-0.7166144941210074*EINSIDE
  </Expression>

</FieldUpdater>

<FieldUpdater malDDenomupperZ>
  kind = malUpdater
  lowerBounds = [0  0  125]
  upperBounds = [220  220  127]
  upperOrLower = upper
  numOrDenom = denom
  writeField = E
  dir = 2
  frac = 0.5
  power = 3.0
</FieldUpdater>

<FieldUpdater malBDenomupperZ>
  kind = malUpdater
  lowerBounds = [0  0  125]
  upperBounds = [220  220  127]
  upperOrLower = upper
  numOrDenom = denom
  writeField = B
  dir = 2
  frac = 0.5
  power = 3.0
</FieldUpdater>

<FieldMultiUpdater yeeAmpere>
  kind = yeeAmpereUpdater
  readFieldCompShifts = [0 0]
```

```
  components = [0   1   2]
  contractFromBottomInNonComponentDir = True
  gridBoundary = vsimPecShapes
  interiorness = deymittra
  readFields = [B J]
  writeFields = [E]
  lowerBounds = [0  0  0]
  upperBounds = [220  220  127]
</FieldMultiUpdater>

<FieldMultiUpdater yeeFaraday>
  kind = yeeFaradayUpdater
  gridBoundary = vsimPecShapes
  interiorness = deymittra
  components = [0   1   2]
  expandToTopInComponentDir = 1
  lowerBounds = [0  0  0]
  upperBounds = [220  220  127]
  readFields = [E]
  writeFields = [B]
</FieldMultiUpdater>

<FieldUpdater yeeDeyMittra>
  gridBoundary = vsimPecShapes
  interiorness = deymittra
  kind = deyMittraUpdater
  lowerBounds = [0   0   0]
  upperBounds = [220   220   127]
  readFields = [E]
  writeFields = [B]
</FieldUpdater>

<FieldUpdater edgeToNode>
  kind = edgeToNodeVec
  lowerBounds = [0  0  0]
  upperBounds = [221  221  128]
  readFields = [E]
  writeFields = [nodalE]
</FieldUpdater>

<FieldUpdater copyPerimlowerX>
  kind = unaryFieldOpUpdater
  minDim = 1
  lowerBounds = [0  0  0]
  upperBounds = [1  221  128]
  operation = set
```

```
  bumpReadIter = [0  0  0]
  readFields = [E]
  component = 0
  writeFields = [nodalE]

  <STFunc copyFunc>
    kind = constantFunc
    amplitude = 1.
  </STFunc>

</FieldUpdater>

<FieldUpdater copyPerimupperX>
  kind = unaryFieldOpUpdater
  minDim = 1
  lowerBounds = [220  0  0]
  upperBounds = [221  221  128]
  operation = set
  bumpReadIter = [-1  0  0]
  readFields = [E]
  component = 0
  writeFields = [nodalE]

  <STFunc copyFunc>
    kind = constantFunc
    amplitude = 1.
  </STFunc>

</FieldUpdater>

<FieldUpdater copyPerimlowerY>
  kind = unaryFieldOpUpdater
  minDim = 2
  lowerBounds = [0  0  0]
  upperBounds = [221  1  128]
  operation = set
  bumpReadIter = [0  0  0]
  readFields = [E]
  component = 1
  writeFields = [nodalE]

  <STFunc copyFunc>
    kind = constantFunc
    amplitude = 1.
  </STFunc>
```

```
</FieldUpdater>

<FieldUpdater copyPerimupperY>
  kind = unaryFieldOpUpdater
  minDim = 2
  lowerBounds = [0  220  0]
  upperBounds = [221  221  128]
  operation = set
  bumpReadIter = [0  -1  0]
  readFields = [E]
  component = 1
  writeFields = [nodalE]

  <STFunc copyFunc>
    kind = constantFunc
    amplitude = 1.
  </STFunc>

</FieldUpdater>

<FieldUpdater copyPerimlowerZ>
  kind = unaryFieldOpUpdater
  minDim = 3
  lowerBounds = [0  0  0]
  upperBounds = [221  221  1]
  operation = set
  bumpReadIter = [0  0  0]
  readFields = [E]
  component = 2
  writeFields = [nodalE]

  <STFunc copyFunc>
    kind = constantFunc
    amplitude = 1.
  </STFunc>

</FieldUpdater>

<FieldUpdater copyPerimupperZ>
  kind = unaryFieldOpUpdater
  minDim = 3
  lowerBounds = [0  0  127]
  upperBounds = [221  221  128]
  operation = set
  bumpReadIter = [0  0  -1]
  readFields = [E]
```

```
  component = 2
  writeFields = [nodalE]

  <STFunc copyFunc>
    kind = constantFunc
    amplitude = 1.
  </STFunc>

</FieldUpdater>

<FieldUpdater faceToNode>
  kind = faceToNodeVec
  lowerBounds = [0  0  0]
  upperBounds = [221  221  128]
  readFields = [B]
  writeFields = [nodalB]
</FieldUpdater>

<InitialUpdateStep Applied_BaddingUpdaterInitStep>
  alsoAfterRestore = False
  updaters = [Applied_BaddingUpdater]
  messageFields = [nodalB]
</InitialUpdateStep>

<UpdateStep historydc_source_0ScalarupdaterStep>
  toDtFrac = 1.0
  updaters = [historydc_source_0Scalarupdater]
  messageScalars = [historydc_source_0Scalar]
</UpdateStep>

<UpdateStep historydc_source_1ScalarupdaterStep>
  toDtFrac = 1.0
  updaters = [historydc_source_1Scalarupdater]
  messageScalars = [historydc_source_1Scalar]
</UpdateStep>

<UpdateStep Applied_BaddingUpdaterStep>
  toDtFrac = 1.0
  updaters = [Applied_BaddingUpdater]
  messageFields = [nodalB]
</UpdateStep>

<UpdateStep portBeforeAmpereLower2Step>
  toDtFrac = 1.0
  updaters = [portBeforeAmpereLower20 portBeforeAmpereLower21]
  messageFields = [E]
```

```
</UpdateStep>

<UpdateStep portIncidentLower20Step>
  toDtFrac = 1.0
  updaters = [portIncidentLower20]
  messageFields = [E]
</UpdateStep>

<UpdateStep portIncidentLower21Step>
  toDtFrac = 1.0
  updaters = [portIncidentLower21]
  messageFields = [E]
</UpdateStep>

<UpdateStep portAfterAmpereLower2Step>
  toDtFrac = 1.0
  updaters = [portAfterAmpereLower20 portAfterAmpereLower21]
  messageFields = [E]
</UpdateStep>

<UpdateStep ampereStep>
  toDtFrac = 1.0
  updaters = [yeeAmpere malDDenomupperZ]
  messageFields = [E]
</UpdateStep>

<UpdateStep firstFaradayStep>
  toDtFrac = 0.5
  updaters = [yeeFaraday yeeDeyMittra malBDenomupperZ]
  messageFields = [B]
</UpdateStep>

<UpdateStep secondFaradayStep>
  toDtFrac = 1.0
  updaters = [yeeFaraday yeeDeyMittra]
  messageFields = [B]
</UpdateStep>

<UpdateStep edgeToNodeStep>
  toDtFrac = 1.0
  updaters = [edgeToNode]
  messageFields = [nodalE]
</UpdateStep>

<UpdateStep copyPerimlowerXStep>
  toDtFrac = 1.0
```

```
          updaters = [copyPerimlowerX]
          messageFields = [nodalE]
        </UpdateStep>

        <UpdateStep copyPerimupperXStep>
          toDtFrac = 1.0
          updaters = [copyPerimupperX]
          messageFields = [nodalE]
        </UpdateStep>

        <UpdateStep copyPerimlowerYStep>
          toDtFrac = 1.0
          updaters = [copyPerimlowerY]
          messageFields = [nodalE]
        </UpdateStep>

        <UpdateStep copyPerimupperYStep>
          toDtFrac = 1.0
          updaters = [copyPerimupperY]
          messageFields = [nodalE]
        </UpdateStep>

        <UpdateStep copyPerimlowerZStep>
          toDtFrac = 1.0
          updaters = [copyPerimlowerZ]
          messageFields = [nodalE]
        </UpdateStep>

        <UpdateStep copyPerimupperZStep>
          toDtFrac = 1.0
          updaters = [copyPerimupperZ]
          messageFields = [nodalE]
        </UpdateStep>

        <UpdateStep faceToNodeStep>
          toDtFrac = 1.0
          updaters = [faceToNode]
          messageFields = [nodalB]
        </UpdateStep>

        updateStepOrder = [firstFaradayStep portBeforeAmpereLower2Step ampereStep
portAfterAmpereLower2Step portIncidentLower21Step portIncidentLower20Step
secondFaradayStep historydc_source_0ScalarupdaterStep
historydc_source_1ScalarupdaterStep edgeToNodeStep copyPerimlowerXStep
copyPerimupperXStep copyPerimlowerYStep copyPerimupperYStep
```

```
copyPerimlowerZStep copyPerimupperZStep faceToNodeStep
Applied_BaddingUpdaterStep]
      </MultiField>

      <VectorDepositor JDep>
        kind = areaWeighting
        depField = multiField.J
      </VectorDepositor>

      <Species electron>
        kind = relBorisVW
        charge = -1.6021766208e-19
        mass = 9.10938215e-31
        nominalDensity = 1e+18
        nomPtclsPerCell = 200.0
        fields = [multiField.nodalE multiField.nodalB]
        currDeps = [JDep]

        <ParticleSource Cathode_Emitter_1>
          kind = xvLoaderEmitter
          applyTimes = [5e-09 1.0]
          load = False
          loadAfterInit = False
          loadOnShift = False
          emit = True
          emitBasedOnLocalForce = 0
          useCornerMove = 1

          <VelocityGenerator velGen>
            kind = fieldEmitterVelGen
            velocityIsLocal = 1
            work_function = 4.5
            temperature = 2000.0
            alpha = 5.0
            field_enhancement = 1.0
            multiplier = 600.0
            emitterType = Richardson-Dushman
          </VelocityGenerator>

          <STFunc relMacroFluxFunc>
            kind = expression
            expression =
(((max(ceil(max(0.8535533905932737,(0.5*(sin((5)*atan2((y),(x))+2*3.1415926535897
93*915.0e6*(t)+(3.141592653589793/2))+1)))-0.8535533905932737),0))))
          </STFunc>
```

```
  <PositionGenerator posGen>
    kind = cutCellPosGen
    emitterBoundary = Cathde_largeGeomSolid
    emissionOffset = 0.25
    nomMacroPtclsPerStep = 200.0
  </PositionGenerator>

</ParticleSource>

<ParticleSink lower0Absorber>
  kind = absorber
  minDim = 1
  lowerBounds = [-1   -1   -1]
  upperBounds = [0   221   128]
</ParticleSink>

<ParticleSink upper0Absorber>
  kind = absorber
  minDim = 1
  lowerBounds = [220   -1   -1]
  upperBounds = [221   221   128]
</ParticleSink>

<ParticleSink lower1Absorber>
  kind = absorber
  minDim = 2
  lowerBounds = [0   -1   -1]
  upperBounds = [220   0   128]
</ParticleSink>

<ParticleSink upper1Absorber>
  kind = absorber
  minDim = 2
  lowerBounds = [0   220   -1]
  upperBounds = [220   221   128]
</ParticleSink>

<ParticleSink lower2Absorber>
  kind = absorber
  minDim = 3
  lowerBounds = [0   0   -1]
  upperBounds = [220   220 0]
</ParticleSink>

<ParticleSink upper2Absorber>
  kind = absorber
```

```
    minDim = 3
    lowerBounds = [0   0   127]
    upperBounds = [220   220   128]
  </ParticleSink>

  <ParticleSink Anode_Sink>
    kind = absSavTriCutCell
    minDim = 1
    gridBoundary = anodeGeomSolid
    lowerBounds = [-1  -1  -1]
    upperBounds = [221  221  128]
  </ParticleSink>

  <ParticleSink Cathode_sink>
    kind = absSavTriCutCell
    minDim = 1
    gridBoundary = CathodeGeomSolid
    lowerBounds = [-1  -1  -1]
    upperBounds = [221  221  128]
  </ParticleSink>

</Species>

<History dc_source_0Cathode_Anode_Voltage_BottomFeedback>
  kind = feedbackDesired
  scalar = multiField.historydc_source_0Scalar
  useMeasuredOnly = 0
  timeConstant = 1e-09

  <STFunc desiredHistory>
    kind = expression
    expression = 1.0
  </STFunc>

</History>

<History dc_source_1Cathode_Anode_Voltage_BottomFeedback>
  kind = feedbackDesired
  scalar = multiField.historydc_source_1Scalar
  useMeasuredOnly = 0
  timeConstant = 1e-09

  <STFunc desiredHistory>
    kind = expression
    expression = 1.0
  </STFunc>
```

```
</History>

<History Cavity_Voltage>
  kind = pseudoPotential
  field = multiField.E
  referencePoint = [146  112  55]
  measurePoint = [146  108  55]
</History>

<History Power_Out>
  kind = fieldPoyn
  lowerBounds = [26  26  123]
  upperBounds = [194  194  123]
  fields = [multiField.E multiField.B]
</History>

<History Cathode_Anode_Voltage_Center>
  kind = pseudoPotential
  field = multiField.E
  referencePoint = [110  123  55]
  measurePoint = [110  139  55]
</History>

<History Cathode_Anode_Voltage_Bottom>
  kind = pseudoPotential
  field = multiField.E
  referencePoint = [110  135  2]
  measurePoint = [110  149  2]
</History>

<History Emitted_Current>
  kind = speciesCurrEmit
  species = [electron]
  ptclSource = electron.Cathode_Emitter_1
  sourceType = 0
</History>

<History Anode_Current>
  kind = speciesCurrAbs
  species = [electron]
  ptclAbsorbers = [Anode_Sink]
</History>

<History Macro_Particle_Count>
  kind = speciesNumberOf
```

```
  species = [electron]
</History>

<History Physical_Particle_Count>
  kind = speciesNumPhysical
  species = [electron]
</History>

<History Electron_Energy>
  kind = speciesEnergy
  species = [electron]
</History>

<History Cathode_Current>
  kind = speciesCurrAbs
  species = [electron]
  ptclAbsorbers = [Cathode_sink]
</History>

<History Power_Antenna>
  kind = fieldPoyn
  lowerBounds = [26  26  95]
  upperBounds = [194  194  95]
  fields = [multiField.E multiField.B]
</History>
```